CORA Cork Open Research Archive
Cartlann Taighde Oscailte Chorcaí

Title	Predicting photovoltaic module degradation using current-voltage
Authors	Al Mahdi, Hussain
Publication date	2022-02-01
Original Citation	Al Mahdi, H. 2022. Predicting photovoltaic module degradation using current-voltage. PhD Thesis, University College Cork.
Type of publication	Doctoral thesis
Rights	© 2022, Hussain Al Mahdi. - https://creativecommons.org/licenses/by-nc-nd/4.0/
Download date	2026-11-04 02:18:55
Item downloaded from	https://hdl.handle.net/10468/13282



UCC
University College Cork, Ireland
Coláiste na hOllscoile Corcaigh

Ollscoil na hÉireann, Corcaigh

National University of Ireland, Cork



Predicting Photovoltaic Module Degradation Using Current-Voltage Measurements

Thesis presented by

Hussain Al Mahdi

[0000-0003-1931-7350]

for the degree of

Doctor of Philosophy

University College Cork

School of Engineering

Head of School: Prof. Jorge Oliveira

Supervisor(s): Dr. Alan P Morrison and Dr. Paul Leahy

February 2022

Declaration

This is to certify that the work I am submitting is my own and has not been submitted for another degree, either at University College Cork or elsewhere. All external references and sources are acknowledged and identified within the contents. I have read and understood the regulations of University College Cork concerning plagiarism and intellectual property.

Hussain Al Mahdi

Acknowledgments

First of all, I would like to express my thanks and gratitude to my country, Saudi Arabia, for funding my Ph.D. study and giving me this opportunity to improve my skills and critical thinking.

I'm deeply grateful for many individuals for whom my Ph.D. work was not achievable without their help and support. I want to thank Dr Mostafa Elsharqawi my supervisor at University of Guelph, Canada. I want to express my sincere thanks and gratitude to my supervisors, Dr. Alan Morrison, and Dr. Paul Leahy. They lighted the dark path toward Ph.D.; after almost each Ph.D. meeting with them, I felt energetic, enthusiastic, motivated, and optimistic. I wish to extend my special thanks to postgraduate students and researchers, especially George O'Mahoney, Brian Murphy, Alison O'Shea, Nikolina Molnar, and Oksana Semenova. I would like to thank Prof. Mohammed Abido, Dr. Chokri Belhaj, and Mr. Khaled Alodah for instructing me during the scientific placement at King Fahad University of Petroleum and Minerals.

My sincere appreciation to the staff of the School of Engineering and Architecture: Michel O'Shea, Timothy Power, Dr. Bill Wright, Dr. Dominic O'Sullivan, Mary O'Leary, Claudia Cashman, Gerard Hooton, and James Griffiths. I'm grateful to the people I met in Canada and Ireland and became best friends: Dr. Ahmed Ashoor, Dr. Muath Alomair, Dr. Khaleel Alkhalaf, Dr. Moahmmed Alsaygh, Ali Abdi, Jamal Alfarag, Bandar Althobaiti, Dr. Husam Alzayer, Dr. Sultan Mohammed, and Dr. Noah Ismaeel.

I want to dedicate this dissertation to my family; my grandfather Ali Almuslim who encouraged me to continue studying and acquiring knowledge and sadly passed away before pursuing my Ph.D. study. To my parents, Ali Al Mahdi, and Zainab Almuslim, who never stopped thinking about me and whom I wish to make them happy as long as my heart is beaten. To my uncle Hassan Almuslim, my older brother Muayed Al Mahdi, my siblings. To my wife Fatema Alsanan, my son Ali, and my daughters Zainab and Layal, who accompany me in this Ph.D. journey and make my life enjoyable, less stressful, healthier, and easier.

List of Publications

H. A. A. Mahdi, P. G. Leahy, and A. P. Morrison, "Predicting Early EVA Degradation in Photovoltaic Modules from Short Circuit Current Measurements," in *IEEE Journal of Photovoltaics*, vol. 11, no. 5, pp. 1188-1196, Sept. 2021, doi: 10.1109/JPHOTOV.2021.3086455.

Submitted Paper

Early Prediction of Shunt Resistance Degradation in Photovoltaic Modules, submitted to *IEEE Journal of Photovoltaics. March-2022.*

Conferences Attended

17-19 November 2021, 3rd International Conference on Advances in Signal Processing and Artificial Intelligence (ASPAI' 2021), Porto, Portugal.

13-15 December 2021: The 31st International PV Science and Engineering Conference (PVSEC-31), Sydney, Australia.

Table of Contents

Chapter 1| Introduction 1

1.1 Introduction 1

1.2 PV Degradation Rate and Failures 4

1.3 Thesis Objectives 6

1.4 Thesis Approach 7

1.5 Thesis Structure 8

Chapter 2 | A review of PV Failures and Degradation Mechanisms 11

2.1 Introduction 11

2.2 Definition of PV Failure 11

2.3 Failures of the PV Module Components 12

2.3.1 Protective Glass 13

2.3.2 Encapsulant 15

2.3.3 Solar Cells 18

2.3.4 Backsheet 20

2.3.5 Junction Box and Bypass Diodes 22

2.4 Classification of Crystalline Photovoltaic Module Failures 23

2.5 Environmental Stress Factors that Trigger PV Degradation 25

2.5.1 PV Failures Triggered by Harsh Weather 25

2.5.2 Temperature and Humidity 26

2.5.3 Dust and Dust Storms 26

2.6 Detection of PV Failures 28

2.6.1 Visual Inspection 30

2.6.2 Infrared Imaging 30

2.6.3 Electroluminescence Imaging 31

2.6.4 Ultrasonic Inspection 32

2.6.5 Electrical Characterization 32

2.6.6 Detection Degradations and Failures Using Shunt Resistance . 36

2.7 Conclusion 39

Chapter 3| Early prediction of EVA Degradation in PV Modules from Short Circuit Current Measurements 41

3.1 Introduction 41

3.2 Overview of the SPICE Model 43

3.2.1 Standard Solar Spectrum (AM1.5G) 44

3.2.2 Short Current Density, J_{SC} 45

3.2.3 Current-Voltage (I-V) characteristic of a Solar Cell 47

3.3 Simulation of EVA Degradation 48

3.3.1 Transmittance Extraction from Experimental Data 50

3.3.2 Simulation of Solar Spectrum for the Five Encapsulant 51

3.3.3 Simulation of the Short-Circuit Current Densities 52

3.3.4 Simulation of the I-V Curves for the Five Degraded Encapsulant Scenarios 53

3.4 Results and Discussion 55

3.4.1 Correlations Between EVA Transmittance and Electrical Parameters 55

3.4.2 Simulation Verification Using the PC1D PV Modelling Software 57

3.4.3 Modelling the onset of EVA degradation 58

3.5 Conclusion 63

Chapter 4 | Early Prediction of Shunt Resistance Degradation in PV Modules 65

4.1 Introduction 65

4.2 Experimental Procedure 66

4.2.1 Adding External Resistance in Parallel to the Shunt Resistance 70

4.2.2 Extracting the Internal Shunt Resistance 72

4.3 Effect of Irradiance and Temperature Fluctuation 73

4.3.1 Effect of Irradiance Fluctuation on I-V Measurements 73

4.3.2 Effect of Temperature Rise on I-V Measurements 74

4.4 Results and Discussion 76

4.4.1 Effect of Low Shunt Resistance on Open-Circuit Voltage, Maximum Output Power and Fill Factor 77
4.4.2 Verification of the Measurements 80
4.4.3 Reducing the Surface Area of Solar Cell 81
4.4.4 Determining the Critical Degradation Point for Solar Cell 82
4.4.5 Modelling the Onset of Shunt Resistance Degradation 83
4.5 Conclusion 86

Chapter 5 | Early Prediction of Failed Cells in a PV Module Using Open-Circuit Voltage 88
5.1 Introduction 88
5.2 SPICE Model for Solar Cell 90
5.2.1 Equivalent Circuit Model of Solar Cell Used in SPICE 91
5.3 Simulation of the I-V Curves at Degradation Modes 93
5.3.1 Simulation of PV Module's I-V Curve at Degradation Modes 99
5.4 Results and Discussion 101
5.4.1 Correlation between Fill Factor and Shunt Resistance 103
5.4.2 Correlation between Maximum Power Output and Shunt Resistance 103
5.4.3 Correlation between Open-Circuit Voltage and Shunt Resistance 104
5.4.4 Model to Detect Cells with Degraded Shunt Resistance in a PV Module 108
5.5 Conclusion 109

Chapter 6| Failed PV Modules at KFUPM: Corrective Actions and the Potential of Machine Learning Applications 112
6.1 Introduction 112
6.2 Experimental Procedure and Results 113
6.2.1 Effect of Dust Accumulation on PV Module Surface 115
6.2.2 PV Module Diagnosed with Hotspot Failure 117
6.3 Corrective Actions and Potential of Machine Learning Models 118
6.4 Conclusion 123

Chapter 7| Cost Analysis for Substituting a Degraded PV Module as A Corrective Action 125

7.1 Introduction 125

7.2 Cost Analysis for Substituting a Degraded PV Module 126

7.3 Simulation of PV Array and String to Extract Parameters 127

7.3.1 Extracting Parameters from Simulated PV Module 129

7.4 Estimated Energy from PV Systems in Ireland 130

7.5 Energy Loss from PV Systems with a Degraded Module 132

7.5.1 PV String with a Module Showing Yellow-Brown EVA 135

7.5.2 PV Array with a Module Showing Yellow-Brown EVA 136

7.5.3 PV Systems with a Module Showing Shunt Resistance Degradation 136

7.6 Optimal Time for Replacement of Degraded Module 137

7.6.1 Cost of 3- kW and 5-kW PV Systems in Ireland 138

7.6.2 Cost Comparisons for Replacement of Degraded PV Module 140

7.7 Conclusion 143

Chapter 8| Conclusions, Summary and Outlook 145

8.1 Contributions 145

8.2 Thesis Summary 148

8.3 Future Works 152

REFERENCE LIST 155

List of Abbreviations

A_0	Investment or installation cost of the photovoltaic system
A_i	Maintenance cost of the photovoltaic system
AM1.5G	Standard Solar Spectrum
C_a	The annual cost of a photovoltaic system
c_E	The cost of the system in kilo-Watthour
C_{tot}	The total cost of a photovoltaic system
DTC	Decision Tree Classifier
E_a	Generated energy per year of a photovoltaic system
EF	Modelling efficiency formula
EVA	Ethylene Vinyl Acetate
FF	Fill Factor of the solar cell
G	Solar Irradiance
G-device	Voltage-Controlled Current Source
I_{01}	First Saturation Current of the solar cell
I_{02}	Second Saturation Current of the solar cell
I_m	Maximum Current Output at the solar cell's current-voltage curve
I_{SC}	Short-Circuit Current of the solar cell
IR	Infrared Imaging
ir	Interest rate, also known as discounted rate; a rate applied to investment amount given by a financial lending institute

$\boldsymbol{I-V}$	Current-Voltage Curve of the solar cell
J-box	Junction Box, a component of photovoltaic module
$\boldsymbol{J_{01}}$	First Saturation Current Density of the solar cell
$\boldsymbol{J_{02}}$	Second Saturation Current Density of the solar cell
$\boldsymbol{J_{darkB}}$	Dark Current Density of the semiconductor's base
$\boldsymbol{J_{\mathrm{darkE}}}$	Dark Current Density of the semiconductor's emitter
$\boldsymbol{J_L}$	Photo-Current Density of the solar cell
$\boldsymbol{J_{sc\lambda}}$	Spectral Short-Circuit Current Density of the solar cell
$\boldsymbol{J_{SC}}$	Short Circuit Current Density of the solar cell
$\mathbf{kW}_{\boldsymbol{p}}$	The Peak Power, Maximum-Power Output in Kilowatts
LID	Light Induced Degradation
MAE	Mean Absolute Error
MV	Mean Value
η	Ideality Factor
PDMS	Polydimethylsiloxane, type of polymer used as an encapsulant in photovoltaic modules
PET	Polyethylene terephthalate, plastic material used as a backsheet in a photovoltaic module.
PID	Potential Induced Degradation
$\boldsymbol{P_{max}}$	Maximum Power Output, the maximal power produced by the solar cell
PV	Photovoltaic
PWL	Piecewise Linear Source in SPICE Modelling Program

RPN	Risk Priority Number used for rating guideline
$\boldsymbol{R_{sho}}$	The resistance estimated from the slope near the short-circuit current of the solar cell's current-voltage curve
$\boldsymbol{R_{sh}}$	Shunt or Parallel Resistance of the photovoltaic solar cell
$\boldsymbol{R_{so}}$	The resistance estimated from the slope near the open-circuit voltage of the solar cell's current-voltage curve
$\boldsymbol{R_s}$	Series Resistance of the solar cell
RMSE	Root Mean Square Error
S	The Annual Solar Radiation
SD	Standard Deviation
SPICE	Simulation Program with Integrated Circuit Emphasis
STC	Standard Test Condition
TPU	Thermoplastic Polyurethane
TTI	Thurlby Thandar Instruments
UV	Ultra-Violet
$\boldsymbol{V_{OC}}$	Open-Circuit Voltage of the solar cell
$\boldsymbol{V_m}$	Maximum Voltage Output at the solar cell's current-voltage curve

List of Figures and Tables

Figures

Figure 1.1 Average annual renewable capacity addition of renewable energy sources between 2019 and 2021[4]. 1
Figure 1.2 Equivalent circuit of a single diode model of the solar cell. 2
Figure 1.3 Worldwide installed capacity of PV in 2020 [13]. 3
Figure 1.4 Fire incident in PV array initiated by hotspot failure [36]..... 6
Figure 2.1 PV module components designed by Fusion 360 modelling program. 12
Figure 2.2 (A) Example of PV module with a shattered protective glass [54]. (B) Broken glass due to manufacturing fault by too tight bolt [33]..... 14
Figure 2.3 (A) Brown discolouration of PV cell [79]. (B) PV module affected by delamination [57]. (C) PV module affected by delamination that led to corrosion [80]. 17
Figure 2.4 (A) PV module affected by snail track failure [94]. (B) PID failure detected by electroluminescence image [100]. (C) Hotspot burned the cell solder bonding and exhibited burn marks in the back sheet [101]..... 20
Figure 2.5 (A) Backsheet bubbles [97]. (B) Backsheet delamination [97]. (C) Burn marks were caused by a hotspot in the backsheet [101]. 21
Figure 2.6 (A) Failed bypass diodes led to hotspots [101]. (B) Poor bonding of j-box [100]..... 22
Figure 2.7 Infrared imaging to discover high-temperature cells in a PV module [127]. 31
Figure 2.8 (A) EL imaging of a healthy monocrystalline solar cell. (B) El imaging of a cracked monocrystalline solar cell [130]. 31
Figure 2.9 Ultrasonic inspection for several cell wafers showing cell No.11 has an abnormal reduction in frequency, indicating a crack failure [133]..... 32
Figure 2.10 Current-Voltage and Power-Voltage curves display the major parameters of a solar cell; I_{sc}, the current at zero V, V_{OC}, the voltage at zero current, and P_{max}, the maximum point at the voltage and current. 34

Figure 3.1 Simulation of the standard solar spectrum AM1.5G on earth, and standard solar spectrum with a 10% reduction. 45
Figure 3.2 Standard solar spectrum with an obstructive wavelength from 0.523 µm to 0.530 µm.....49
Figure 3.3 Standard solar spectrum with an obstructive wavelength from 0.533µm to 0.546 µm.....50
Figure 3.4 Transmittance for the five different encapsulants adapted from [83], with extracted transmittance data-points using Engauge Digitizer. Note: extraction below 300 nm was not carried out as these wavelengths are not absorbed by the silicon solar cell. 50
Figure 3.5: Six simulated solar spectra demonstrating the degradation of EVA encapsulant expected from Pern et al. [83]. 52
Figure 3.6: Simulation of the spectral short-circuit current density for the unexposed and four degraded encapsulant scenarios.....53
Figure 3.7: Simulation of the I-V curves for the five encapsulant scenarios..54
Figure 3.8: Relationships between received solar irradiance via encapsulant degradation scenarios and electrical parameters of the solar cell. The short-circuit current, maximum power output, and open-circuit voltage were normalized relative to their value in the unexposed EVA degradation scenarios and electrical parameters of the solar cell. 56
Figure 3.9: I-V curves generated from a solar cell with five encapsulant scenarios simulated in the PC1D modelling program.....57
Figure 3.10 Linear fit models between the solar irradiance and the generated short-circuit current for EVA degradation Vs normal change of solar irradiance started from the same irradiance EVA received when it was clear. When the P_{max} falls below 50% of the original power the cell is considered to have failed. 62
Figure 4.1 Solar cell housing designed using Autodesk Fusion 360 67
Figure 4.2 Newport Sol1A, solar simulator along with Keithley Source Meter used to take measurements of the electrical parameters of the solar cell samples and some resistors that were added in parallel to the shunt resistance. 68

Figure 4.3 The equivalent circuit of the solar cell's single-diode model, modified by adding a resistance R_{sh2} in parallel with the cell's internal shunt resistance R_{sh1}.....71
Figure 4.4 I-V curves obtained at different shunt resistance levels with 1-2% limited variations of solar irradiance.....73
Figure 4.5 10 Measurements taken for every 30 seconds of electrical parameters of Sample 2 with a parallel resistor of 2.2 Ω.....75
Figure 4.6 The mean I-V curves from 10 measurements of the second sample for different externally added resistors; ± standard deviation error bars were calculated and presented in the figure.....76
Figure 4.7 V_{OC}, P_{max}, and fill factor versus shunt resistance for Samples 2 and 5, the points represent the mean value of ten measurements. ± Standard deviation error bars were negligibly small and omitted from the figures.....78
Figure 4.8 Electrical parameters of the 1st and 2nd Measurements (MEAS) of Sample 5. Error bars refer to the difference in two experiments conditions due to irradiance and temperature fluctuations…….....80
Figure 4.9 Electrical parameters of Sample 3 with a reduced surface area of 42.5 cm^2…….....81
Figure 4.10 The derivative of fill factor with respect to shunt resistance vs shunt resistance values for the second cell……..……82
Figure 4.11 Linear models correlate Isc vs V_{OC} and P_{max}, for solar cells in healthy and degraded (reduced shunt resistance) states. Employing I_{SC} instead of irradiance is cost-effective for a residential PV system as there will be no requirement for irradiance measurement tools …….....85
Figure 5.1 Equivalent circuit of two diodes model adopted in SPICE [5]…..92
Figure 5.2 Simulation of I-V curves at different shunt resistance levels using SPICE.....96
Figure 5.3 Simulation of I-V curves at different shunt resistance levels using SPICE.....97
Figure 5.4 I-V curve of simulated PV module, consists of 36 solar cells connected in series using SPICE.....100

Figure 5.5 I-V curves for a PV module simulated using SPICE showing the effect of lowering shunt resistance in a different number of solar cells. Where (A) is one cell with low R_{sh} and (B) six cells with low $R_{sh.}$ 102
Figure 5.6 Correlation with PV module's shunt resistances and (A) fill factor, (B) Maximum-power output (C) Open-circuit voltage. 106
Figure 5.7 Correlation between the number of defective cells in PV module with the (A) fill factor, (B) Maximum-power output (C) Open-circuit voltage. 107
Figure 5.8 Linear fit models correlate I_{sc} and V_{oc} to compare between healthy and faulty states of a PV module, the model can be used to detect the onset of PV cells degradation or failure in PV module caused by shunt resistance reduction. 108
Figure 6.1 (A) Typical experiment for DC measurement at KFUPM lab [207]. (B) Experiment set up for the dust accumulation and hotspot measurements. 114
Figure 6.2: (A) Cleaned PV module v. (B) dusty PV module. 115
Figure 6.3 I-V curve of dusty module versus the I-V curve of the cleaned PV module surface. Y-axis is the current normalized to 1A. 116
Figure 6.4 (A) I-V curve of PV module with one cell damaged by hotspot. (B) snapshot of hotspot damage 118
Figure 6.5 Decision tree model classifies between EVA and R_{sh} degradation mechanisms. 119
Figure 6.6 Decision tree ML model for small-scale data used to predict, detect and classify shunt resistance and EVA degradations of PV module. X [1] is the slope used to detect shunt resistance degradation, and X [0] is the slope used to detect EVA degradation. 122
Figure 7.1 I-V and P-V curve of PV 100 W PV module 129
Figure 7.2 Diagram demonstrates the V_m, $I_{m,}$ and P_{max} parameters of a PV-string consisting of 6 PV modules connected in series, one of which shows the parameters of a degraded module by yellow-brown EVA or by low shunt resistance at 113.1 Ω cm^2. 132

Figure 7.3 Diagram demonstrates the V_m, I_m, and P_{max} of a 6×5 array, one of which shows the parameters of a degraded module by EVA or by shunt resistance at 113.1 Ω cm^2.....134
Figure 7.4 Estimated cost for a PV string consisting of 10 modules at four different times of degradation. Where: (A) Estimated cost when replacing an irreversibly degraded module in the system,(B) Estimated cost of the PV system when one module degraded by yellow-brown EVA, (C) Estimated cost of the PV system when one module degraded by low R_{sh} at 113.1 Ω cm^2...141
Figure 7.5 Estimated cost for a PV 6×5 array system at four different times of degradations. Where: (A) Estimated cost when replacing an irreversibly degraded module in the system,(B) Estimated cost of the PV system when one module degraded by yellow-brown EVA, (C) Estimated cost of the PV system when one module degraded by brown EVA, (D) Estimated cost of the PV system when one module degraded by low R_{sh} at 113.1 Ω cm^2. 142

Tables

Table 2-1 Photovoltaic failures list classified by three different reviews. 24
Table 2-2 Comparison between the chapter's classification methodology and some scientific articles' classification methodology in the PV area. 40
Table 3-1 Values of the short-circuit current density for the five encapsulant scenarios. 53
Table 3-2 Value of Isc, Voc, and P_{max} for the five encapsulant degradation scenarios along with a further 5%, and 10% reduction in the dark encapsulant transmittance, and their ratio relative to the unexposed EVA values. 55
Table 3-3 Comparison between the generated Isc from PC1D and SPICE for the five EVA degradation scenarios. 58
Table 3-4 Short-circuit current relative to the unexposed encapsulant. 61
Table 3-5 The approach used by widely-cited EVA discolouration articles and the approach followed in this chapter. 64
Table 4-1 The resistors' mean values (MV) that were added to the solar cell's samples, with the resulting total shunt resistance. 72

Table 4-2 The approach used by widely-cited shunt resistance articles and the one followed in this chapter. 87
Table 5-1 Root Mean Square Error and Modelling Efficiency for the Simulated I-V 98
Table 5-2 The simulation approach used by widely-cited shunt resistance articles and the one followed in this chapter. 110
Table 6-1 Comparison between decision tree ML model used by widely-cited article and the one followed in this chapter. 124
Table 7-1 Estimated yearly energy production in Ireland for a PV string with five peak power ratings facing south tilted at 60º angle, at three different scenarios, (1)Without extreme degradation, (2) One module with EVA yellow-brown degradation, and (3) One module with shunt resistance degradation at 113.1 Ω cm^2 130
Table 7-2 Estimated yearly energy production in Ireland for PV array with five peak power rating facing south tilted at 60º angle at three different scenarios, (1) Without extreme degradation, (2) One module with EVA yellow-brown degradation, and (3) One module with shunt resistance degradation at 113.1 Ω cm^2 132
Table 7-3 Calculated costs for 3 kW PV string and 6 kW PV array 139
Table 7-4 Comparison between the cost analysis used in Orkizis [251] and the one followed in this chapter. 144

Abstract

With the global increase of photovoltaic (PV) modules deployment in recent years, monitoring techniques to ensure a safe and healthy operation have become crucial. Despite PV modules being considered reliable devices, failures and extreme degradations often occur. They have been frequently classified into two categories: optical and electrical.

Of optical failures, degradation of the ethylene-vinyl acetate (EVA) encapsulant due to prolonged ultra-violet (UV) exposure and other environmental stress factors, such as temperature and humidity, is the most common failure.

Conversely, electrical failures are linked to low shunt resistance (R_{sh}). Unidentified degradation mechanisms in these categories lead to catastrophic failure. The objective of this dissertation is to find comprehensive techniques to predict and detect these degradations at the initial stages. This can be achieved by continuously monitoring the current-voltage (I-V) curve parameters of the solar cell, from healthy-state (no degradation) to failure-state (critical degradation). The EVA degradation research was accomplished using an electrical circuit simulator (SPICE) to simulate an experimental result. In addition to simulations, experiments were performed to artificially lower the solar cell shunt resistance.

The effect of EVA and shunt resistance degradations on solar cells' major parameters; maximum power output (P_{max}), short-circuit current (I_{SC}), open-circuit voltage (V_{OC}), and fill factor were analysed. As a result, novel linear models were developed and proposed as strong predictors and observers, and also are suitable for implementation in online monitoring systems for operational PV modules. Training a machine learning model to classify degradation mechanisms was also shown effective. Corrections should be made if critical degradation is detected. Aside from the potential risks to the PV system, the thesis showed that replacing a degraded PV module is cost-effective before the critical degradation state.

1. Chapter 1| Introduction

1.1 Introduction

Among different renewable energy sources available on earth, solar energy is the most prevalent renewable source in most regions of the world due to its cost-effective applications and installation simplicity [1]. The cost of photovoltaic (PV) systems has declined rapidly over time [2]. For example, Germany's PV investment for a 10 kW system dropped by nearly 92.6% from €14000 to €1036 per kW between 1990 and 2020 [3]. In the U.S, the wholesale price for multi-crystalline modules remarkably dropped by 95% between 2008 and 2018. Figure 1.1 shows the average annual addition of solar energy over other renewable energy sources for the past three years.

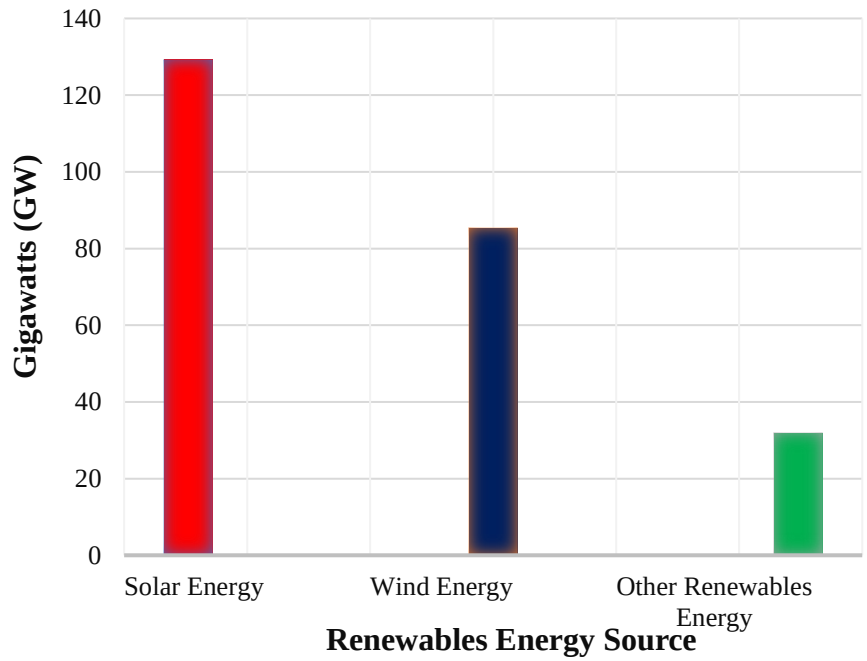


Figure 1.1 Average annual renewable capacity addition of renewable energy sources between 2019 and 2021[4].

Radiation from the sun, which peaks at noon, produces photons absorbed by a $p-n$ junction semiconductor and converted into charges to produce electrical energy. Figure 1.2 shows the equivalent circuit of the solar cell's single diode model, demonstrating the solar cell's working principle. (I_{ph}) and (D_1) are the generated currents by the solar spectrum and the first saturation current, respectively, calculated in ampere. (R_s) is the series resistance that existed due to (a) semiconductor material resistivity, (b) metal contact interface with semiconductor resistance, and the contact resistance [5]. On the other hand, (R_{sh}) symbolises the shunt resistance due to the photo-current losses. The higher the shunt resistance, the fewer photo-currents being lost [6], both R_s and R_{sh} are calculated in Ω multiplied by the surface area of the cell in cm ^{2}. V is the voltage of the solar cell calculated in volts [7].

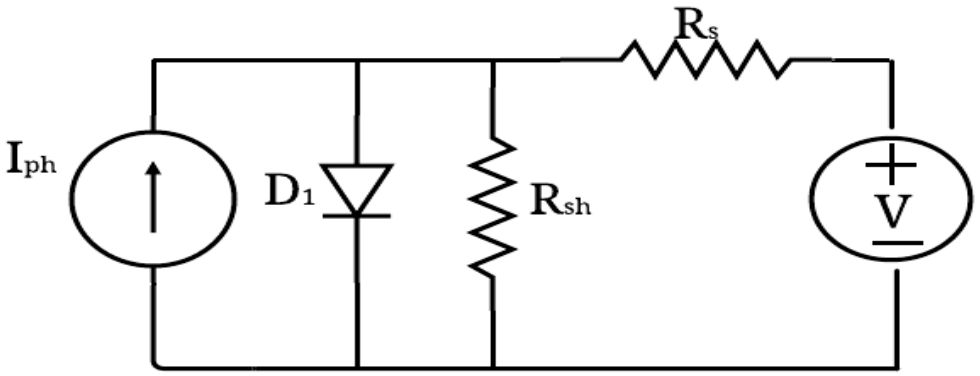


Figure 1.2 Equivalent circuit of a single diode model of the solar cell.

The solar spectrum consists of light having wavelengths of varying intensity. The solar spectrum is typically divided into three wavelength regions: ultra-violet (UV) with a wavelength range from 300 nm to 400 nm, visible with a wavelength range from 400 nm to 700 nm, and from 700 nm to 1150 nm of a wavelength range is infrared. Some of which can be absorbed by PV cell, which is designed to convert the solar spectrum wavelength into electrical energy. It was enhanced in 1954 at Bell laboratory by Chapin *et al*. [8, 9]. Absorbed light that is not converted

into captured charges is dissipated as heat, leading to an increase in the operating temperature of the PV cell.

The conversion efficiency of the solar cell has progressed rapidly [10]; nowadays, it converts nearly 26% of the solar spectrum within the wavelength range from 350 nm to 1140 nm into electrical energy [11]. Due to this rapid advancement in solar efficiency, there was 760 GW of new installed photovoltaic PV capacity worldwide at the end of 2020 [12]. Figure 1.3 shows the installed capacity of PV in the year 2020.

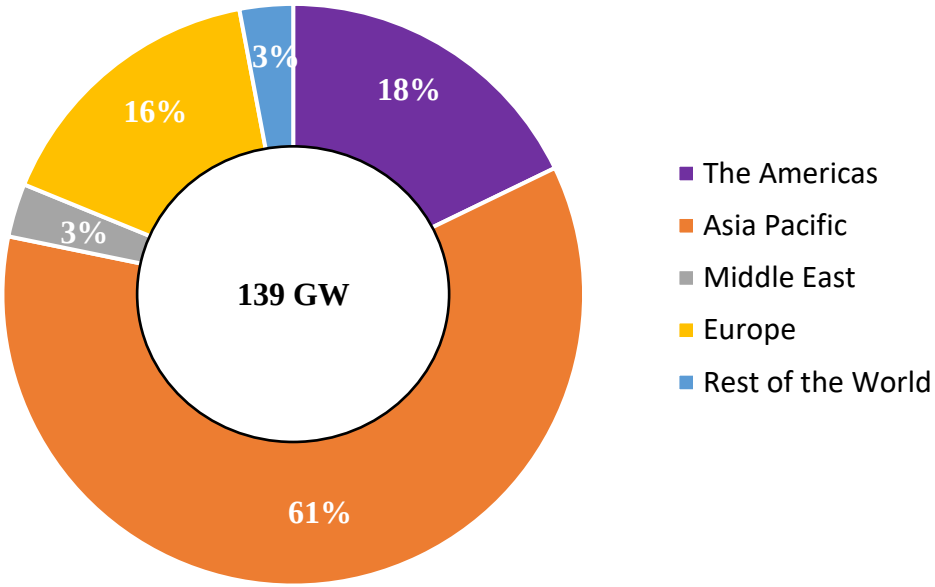


Figure 1.3 Worldwide installed capacity of PV in 2020 [13].

Solar cells are typically connected in series to maximise the voltage output. After being serially connected, they are packaged into modules covered by tempered glass. A polymer layer, called the encapsulant, is also used between the solar cells and the tempered glass to increase light absorption and reduce light reflection [14, 15].

Several different materials have been used as encapsulants for photovoltaic modules, including thermoplastic polyurethane (TPU) and polydimethylsiloxane

(PDMS) [15-18]. The latter is superior to other encapsulants when it comes to immunity against environmental stress and UV radiation. For this reason, it was used in the early development of PV encapsulation [19]. Modern alternative encapsulants include Ionomers (DuPont) that are claimed to have up to 25 times the effectiveness of ethylene-vinyl acetate (EVA) in preventing potential induced degradation and polyolefins (Dow Chemicals) that offer claims of superior electrical resistance and moisture rejection than either EVA or ionomers [20, 21]. However, a trade-off between cost and immunity from environmental stress has favoured EVA, which is why EVA is currently used in almost 80% of all PV modules [22, 23]. Vinyl acetate represents up to 33% of the encapsulant composition, while the remaining percentage is a mixture of ethylene, antioxidants, and curing materials such as peroxide [24, 25].

The PV module after being encapsulated and ready to function is guaranteed by manufacturers to have a 25-years lifetime with an expected power degradation rate of 0.8% per annum [26-28]. The National Renewable Energy Laboratory (NREL) developed accelerated stress tests to keep degradation rates within this range, ensuring superior quality and long-term reliability of PV modules [29]. Failures found in previously deployed PV modules, such as encapsulant discolouration and cracked solar cells, prompted the development of these tests.

1.2 PV Degradation Rate and Failures

Jordan *et al.* [30] examined PV modules operated for 20 years and found that the degradation rate was 0.8% drop in the rated power per annum. However, researchers, e.g., [31-34], agreed that the degradation rate might vary depending on many factors like materials' properties, environmental stress, and type of connections, whether the PV system is connected to the electrical grid or standalone. Another study by Jordan *et al*. [35] examined many degradation rates from 40 countries; the findings agreed with [31-34] that these factors significantly

affect the degradation rate. It was reported by Jordan and Kurtz [32] that the median degradation rate of grid-connected PV systems was higher than stand-alone PV systems deployed in the years before 2000. But the median degradation rate of grid-connected PV systems after the year 2000 became lower. In addition, these factors were described by Köntges *et al.* [36], including damage during transportation to degrade the PV module at a faster pace.

A recent study of deployed PV modules in India found that degradation rates of c. 1.47% per annum have been reported across the industry [37]. Quansha *et al.* [38] monitored PV modules that operated for 16 years in northern Ghana, particularly off-grid-connected, mono-crystalline type. The average temperature of north Ghana could reach 30°C and be combined with an intermediate humidity level of 43%. It was found that the annual degradation rate was 1.54%. This represents a double loss in potential power generation than projected.

Furthermore, some PV failures, such as cell cracks, distribute rapidly [33, 34]; if undetected, they will cause a significant cost loss that may reach up to 10 fold of the equipment cost [39]. This is because some undetected failures may lead to fire and cause catastrophic damage to the whole system [40]. For instance, critical degradation in some PV modules in an array system leads to mismatch, increasing the PV module's thermal temperature and subsequently leading to fire [41, 42]. Critical degradations of PV modules were also listed to initiate fire in a research project based in Germany [40]. Fire can also be caused by hotspot failure, primarily driven by other failure mechanisms that increase the temperature, and eventually catch fire [43, 44].

There have been 80 fire incidents that involved PV in the United Kingdom alone [45]. The fire caused by PV failures is not only resulting in power reduction and cost losses, but it may sadly lead to fatalities. Twenty-two casualties related to fire incidents stemming from PV failures were reported in the UK by BRE National

Solar Centre [45]. Besides, hydrogen decomposes during PV fires into toxic and life-threatening gases, namely, hydrogen fluoride and hydrogen chloride [46]. Figure 1.4 shows a fire incident triggered by a hotspot failure on a module in China.



Figure 1.4 Fire incident in PV array initiated by hotspot failure [46].

According to Sepanski *et al.* [40], PV modules do not catch fire abruptly; fires are often sparked by critical degradation mechanisms that possibly can be detected in advance. Hence, early prediction and determination of PV failures and critical degradation ensure a safe and reliable operation of the PV system, as well as reduce the risk of lost revenue and resultant increased costs for PV operators.

1.3 Thesis Objectives

The prior section gives an overview of the hazard from failures and extreme degradations of PV modules and highlights the importance of monitoring PV systems for the safety and reliability of power production. Therefore, the objectives of the thesis are:

- Review the scientific literature to find the common degradation mechanisms of PV modules.
- Conduct experiments and simulations to find the onset of PV critical degradation and failures from the current-voltage (*I-V*) measurements.
- Develop models to early detect and predict the onset of critical degradation, allowing corrective actions to be taken to avoid catastrophic failures.
- Explore the economic aspect of substituting an irreversibly degraded PV module in PV array or string systems at the early stages of degradations.

1.4 Thesis Approach

Simulation and experimental approaches have been followed in order to meet the thesis objectives. These approaches are implemented to simulate the most common PV degradation mechanisms, generating an adequate amount of data to be collected and explored. The simulation approach tends to generate more realistic data taken from well-published experimental data as well as make use of the thesis' experimental results to generate more data and investigate more PV degradation scenarios. The experimental approach was designed to conduct experimentations with extensive repetitions to produce a sufficient amount of data that brings a robust conclusion. Both the experimental and simulation approaches aimed to closely investigate the output *I-V* curve of the solar cell at progressive deterioration stages. The analysis of the generated data led to developing mathematical models that can predict early failures in PV systems and meet the thesis objectives.

The work of the thesis is expected to positively impact the area of solar energy, particularly with methodological contributions to the PV degradation monitoring field. The contributions can be summarised as follows:

- Extensive surveying of PV degradation and failure mechanisms, identifying the key failure modes.

- Designing a method to test and investigate EVA degradation effect on PV module performance.
- Characterising PV degradation through reduced shunt resistance and developing models for early prediction of shunt resistance degradation.
- Decreasing the cost of PV failures' detection techniques through developing detection techniques that detect degradation and predict them in residential and industrial PV systems, considering the criteria given by Pillai and Rajasekar [47]. That is, detection techniques should be simple, applicable in most PV systems, cost-effective, non-interfering to power and have the ability to localise and classify failures.
- Increasing the safety and reliability of the PV system by avoiding and preventing catastrophic accidents related to PV failures.
- Lay the foundations for future simulation studies about PV failure scenarios.
- Development of machine learning models to detect PV failures through generating mega-data of PV failure scenarios.

1.5 Thesis Structure

The thesis investigates several challenging tasks aiming to find novel and comprehensive methodologies that can be applied to predict, detect, and classify the two most common degradation mechanisms linked to optical and electrical failures in PV systems.

This dissertation starts in Chapter 2 by reporting PV failures and degradation mechanisms on different PV module components from the literature. Then, detection techniques outlined in the literature are briefly explained with more focus on electrical characterization techniques that analyse the output parameters from the *I-V* curve.

The dominant optical failure in the PV module is when there is a loss in the solar transmittance caused by poor PV encapsulation, primarily EVA discolouration. EVA discolouration is primarily considered the onset of PV optical degradation. Thus, a simulation analysis is performed using experimental data from a widely cited article to explore the effect of these degradation scenarios on PV output characteristics in Chapter 3.

Besides the EVA degradation mechanism, most PV degradation and failure mechanisms classified in the electrical category were associated with low shunt resistance. Chapter 4 investigates the effect of low shunt resistance in PV cells. Lowering the shunt resistance is realised artificially in a novel way in five samples of poly-crystalline solar cells. Different shunt resistances values are recorded with their output parameters.

Chapter 5 presents performed simulations of the experimental cells' output parameters obtained at low shunt resistance. It investigates the observed effects on the output parameters when the PV module had low shunt resistance. Four different scenarios are explored; each one has a different number of faulty solar cells. This would be a great potential technique for detecting PV failures that start with few cells and progress rapidly, leading to significant power loss.

Chapter 6 discusses the corrective action to be taken when detecting PV failure. It presents conducted experiments that demonstrate an example of the recommended corrective action when dealing with reversible or irreversible PV failures. Experiments are conducted at King Fahd University of Petroleum and Minerals (KFUPM) and are established to investigate one of the harshest environmental factors on PV; dust accumulation when mixed with high relative humidity and extremely hot weather. Measurements of a PV module diagnosed with a damaged cell caused by a hotspot are also taken. The potential of building

machine learning models to classify between PV failures or degradation mechanisms like EVA and low shunt resistance is discussed and tested.

In Chapter 7, economic analysis carried out when replacing a PV module with irreversible degradation in a PV array or string system is promoted as a corrective action. The cost analysis focuses on the two common degradation mechanisms, EVA discolouration and low shunt resistance, finding the optimal time concerning the cost for replacement.

Chapter 8 summarises and concludes the thesis with a brief discussion highlighting the thesis' main contributions to the PV field and suggests possible future directions.

2 Chapter 2 | A review of PV Failures and Degradation Mechanisms

2.1 Introduction

This chapter reviews the literature and discusses failure and degradation mechanisms of the PV modules with more focus on the encapsulant degradation process. Furthermore, it outlines the hazardous consequences beyond PV module failures, describing what harm they can bring to the PV system. Finally, the chapter briefly explains PV failure detection techniques, with an emphasis on electrical characterization techniques. Most significantly, this chapter prepares the stage for this dissertation to identify the most prevalent degradation processes so that modelling and experimental studies may be conducted to forecast and detect them at the early onset.

2.2 Definition of PV Failure

Photovoltaic failure is not defined uniformly in the literature. Some definitions indicate that a drop of 80% in maximum output power is considered a PV failure [48]. Others claim a 20% drop in maximal power is a PV failure [49]. Durand & Bowling [50] defined failure as a drop of more than 50% in maximum power output. However, The International Electrotechnical Commission (IEC) stated that to ascertain failure in the PV module [51], the 50% drop in maximum-power output must be accompanied by safety hazards. This discrepancy in defining the term explains the reason for Jordan *et al*. [52] to use the word "degradation mode" instead of "failure" when reviewing the literature. The author of this thesis, even with discrepancies in defining the "failure" term, uses both terms: failure and degradation. The term "failure" is universally described in the literature as any unusual changes in PV modules' appearance, function and reliability [46][53].

Whereas the term degradation describes the degradation mechanism of the PV module during its lifetime-cycle. In most cases, the degradation mechanisms if within expected range, 0.8% drop of rated power per annum, do not harm the PV system unless become critical with a higher degradation rate than expected [38],[54].

2.3 Failures of the PV Module Components

A PV module consists of solar cells, solders, encapsulant, and protective glass. The raw material of the solar cell comes from element fourteen of the periodic table: silicon. Although silicon is not the ideal element for power conversion efficiency, its semiconductor properties were extensively studied in the market before the development of the solar cell [10, 55].

Silicon is highly purified and shaped into crystalline perfection and then sliced into a narrow profile ranging between 0.2 to 0.5 mm recognised as a wafer. Residuals of crystalline during the slicing process vary based on the slicing technology. They are regularly used as crystalline ribbons to reduce manufacturing costs [10]. Once the wafer is connected to the ribbon, the solar cell is ready for testing.

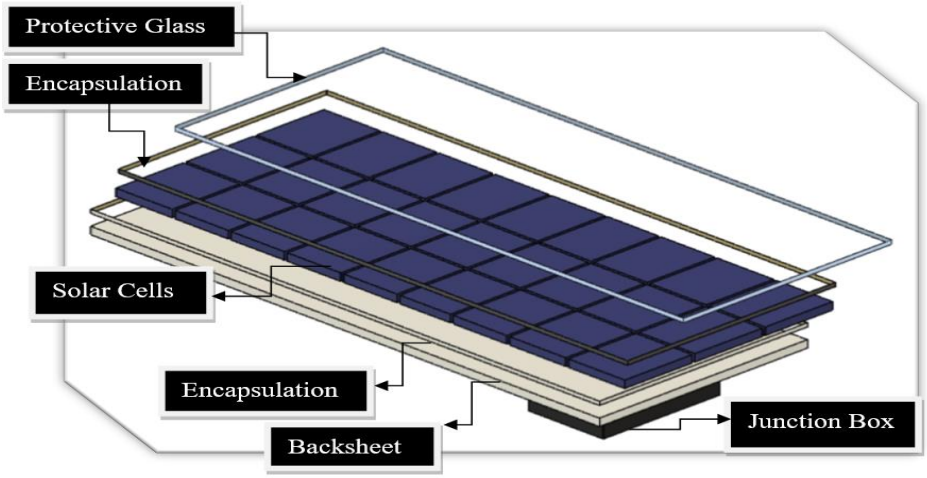


Figure 2.1 PV module components designed by Fusion 360 modelling program.

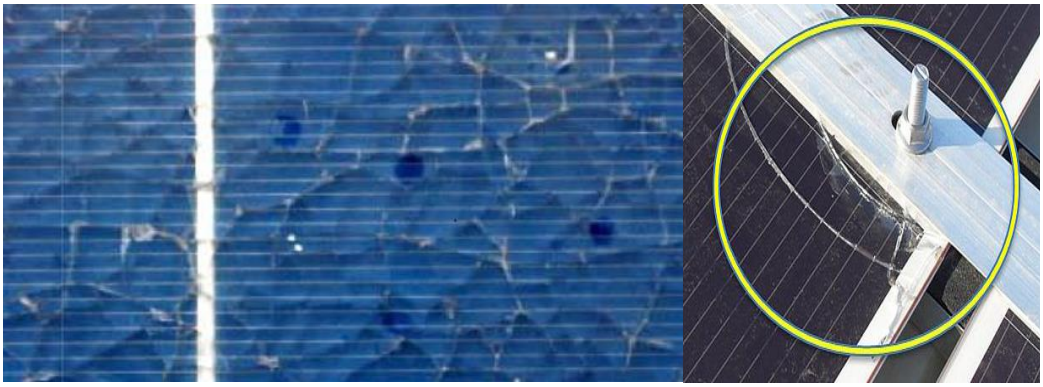
2.3.1 Protective Glass

The protective glass in the PV module is made from tempered glass that consists of a small proportion of iron oxide, not exceeding 0.05%, to allow transmission of sun rays [56]. It is manufactured and designed to resist environmental stress factors such as a drastic shift in temperature. Gürtürk *et al.* [57] validated glass resistivity by measuring its optical transmittance and energy efficiency. They investigated two types of PV glass, one rated to have a 1% higher solar transmittance. One in each type was used as a control glass and tested at a constant temperature. The others were tested with a drastic shift in their temperature reached 120°C. Their results showed no significant impact on energy efficiency, only a slight variation that reached 2.06% at most.

Optical reduction of light transmittance is typically the failure that occurs in PV glasses, and it may be caused by UV wavelengths or by glass breaking or shattering [58, 59]. Some PV glasses are doped with cerium as an additive to protect the PV module from harmful UV wavelengths [60]. However, in a lab study conducted by King *et al.* [61], the use of cerium additive was found to cause a 2% reduction of the optical transmission in the long run.

Moreover, Kempe *et al.* [62] investigated the effect of cerium removal from the protective glass and found that excluding cerium results in a gain of up to 1.8% in optical transmittance [18]. This motivates some manufacturers to persevere without adding cerium. In contrast, its exclusion is considered a risk factor that leads to a threefold increase in the rate of encapsulant delamination [62]. Therefore, it was concluded by Kempe *et al.* [62] that the exclusion of cerium has no benefit on electrical performance and if omitted, an anti-reflective coating must be added to the glass to block the harmful UV wavelengths, particularly the spectrum below 350 nm.

Glass shattering can be the result of poor PV module transportation or incorrect manufacturing processes involving excessive clamping force [32, 64-66]. Shattering or breakage of the module's glass allows water vapour to ingress the solar cells, creating short circuits and safety hazards by causing electrical shock [32]. In addition, the thermal temperature at the breaking point increases, which may cause hotspot failure [36]. In an investigation study by Chandel *et al.* [67], a PV module found with glass breakage had developed hotspot failure with significant power loss. However, Ndiaye *et al*. [32] investigated a PV module with a broken glass operated for five years and found no significant power loss. This may indicate that the breaking glass is not the cause of the failure, but the consequences that come afterwards due to weak protection.



(A) (B)

Figure 2.2 (A) Example of PV module with a shattered protective glass [63]. (B) Broken glass due to installation fault by too tight bolt [36].

Typically, hotspot forms in a PV module when some cells receive less illumination than others, converting them from energy producers to energy dissipaters, i.e., the energy produced by the fully illuminated solar cells is dissipated by the lesser illuminated ones, increasing the latter cells' thermal temperature, making them operated in reverse bias [5]. Hotspot failures are not only driven by broken glass failures but also driven by shading and mismatch

failures [68]. When they occur, they cause permanent damage to the solar cells or other module parts; metal connection, EVA encapsulation, or protective glass [69, 70]. Jordan *et al.* [52] rated PV failures based on their severity, where one is low, and ten is considerably most severe; they listed hotspots to have the highest severity rate among all PV failures.

2.3.2 Encapsulant

From the historical PV research carried out in 1981 by Lathrop *et al*. [71] at Clemson University until recent literature reviews, e.g., [72, 73], EVA encapsulant is the primary cause of PV degradation mechanism. Degradation of the encapsulant leads to poor optical performance in the PV module, leading to poor energy efficiency due to reduced light absorption and increased reflection [74]. Discolouration failure causes a loss in the rate to short-circuit current (I_{SC}). The loss may reach 40% in severe cases, albeit it is not considered a failure as it may not cause a safety hazard [51]. However, discolouration leads to more severe failures like delamination and corrosion. Corrosion of contacts is typically due to the creation of acetic acid [75], commonly occurring long after the effects of discolouration.

Delamination will significantly reduce absorbed light, thereby resulting in a dramatic reduction in I_{SC}. Bubble formation is one of the primary triggers of encapsulant delamination; it is formed initially during the lamination process of encapsulation due to a higher ratio of released volatile organic compounds [76, 77]. The area affected by bubbles in the PV module operates at hotter thermal temperatures and probably leads to burn marks [78]. A study by Rajput *et al.* [79] analysed the degradation mechanism of 90 mono-crystalline PV modules operated for 22 years in India; it was found that the PV modules affected by more bubbles had more power loss.

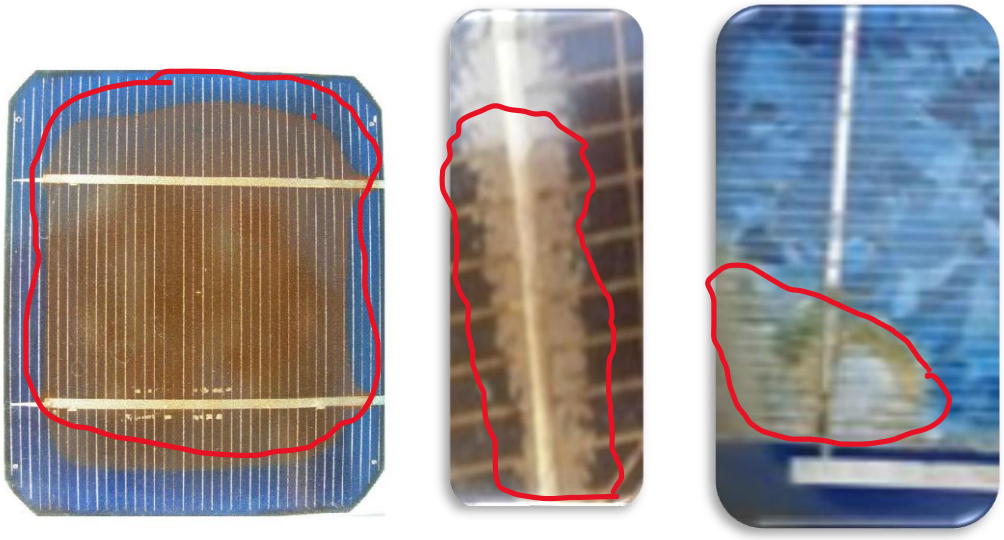
One of the significant causes of encapsulant degradation is ultraviolet radiation, even though it represents less than 3.5% of the solar spectrum [80, 81]. Given its shorter wavelength, UV light has increased energy that degrades the encapsulant over time, typically by breaking down the polymeric bonds [82].

The ultraviolet spectrum is categorized into three regions: UV-A, UV-B, and UV-C. As PV modules are never naturally exposed to UV-C, it is UV-B that is considered the most harmful in triggering the degradation process in EVA encapsulation[83] [84, 85]. The UV irradiance is combined with temperature or other stress factors, which leads to the deterioration of the EVA encapsulant [86] even with the use of UV-blocking glass [51]. As a result, a chemical reaction is triggered that produces acetic acid and aldehyde, altering the EVA colour progressively from clear to light yellow, then yellow, yellow-brown, brown, and ultimately dark brown in critical cases [86, 87].

An experiment conducted by Miller *et al.* [17] demonstrates the effect of UV exposure along with two other stress factors: humidity and temperature, on five different types of encapsulants. Results showed that the rate of degradation increases when encapsulants experience a combination of lower humidity and higher temperature. This leads to a greater discolouration of the encapsulant. A similar study by Arularasu [88] also investigated the effect of these two stress factors along with UV radiation on encapsulant degradation, with similar conclusions.

A term is known as the "yellowness index" was introduced to quantify the discolouration effect. According to the International Standards Organization (ISO) [89], the yellowness index is defined as a shift in polymer colour toward yellow. However, in Oliveira *et al.* [90] it was found that even if the PV encapsulant colour has not yet shifted to yellowness, i.e., did not affect the yellowing index, it cannot be determined with certainty that degradation is not present. This uncertainty has

motivated researchers, for instance [60, 91, 92], to investigate the starting point of the encapsulant degradation process.



(A) (B) (C)

Figure 2.3 (A) Brown discolouration of PV cell [93]. (B) PV Module affected by delamination [67]. (C) PV module affected by delamination that led to corrosion [94].

While it was claimed by Ferrara and Philipp [95], that there is no clear relationship between the change in the encapsulant's colour and electrical performance of the solar cell, it was experimentally proven by Rosillo and Alonso-Garcia [96], that the maximum power output (P_{max}) is reduced when the yellowness index increases. This is in agreement with Pern *et al.* [97] who conducted an experiment in 1991, calculating the electrical performance of solar cells for five different colours of EVA and found that maximum power output was dramatically decreased when the EVA colour altered to a darker brown.

Furthermore, Dechthummarong *et al.* [98] compared PV modules before and after 15 years of operation to investigate if the insulation resistance still complied with the IEC 61215 standard [99]. They classified encapsulant discolouration

based on four colours: light yellow, yellow, brown, and dark brown. It was found that the modules with light yellow and yellow colours had a better electrical performance. Meanwhile, modules with brown discolouration were more likely to develop corrosion, delamination, and bubbles failures than modules with yellow discolouration, although insulation resistance, when measured in all PV modules, was compliant with the IEC 61215 standard. Corrosion and more hazardous failures were also found in modules with brown discolouration in a Brazilian study by Diniz *et al.* [100].

Therefore, detecting the early onset of EVA degradation avoids possible hazards through preventative maintenance, such as direct replacement of modules exhibiting signs of early degradation, even if the PV modules are compliant with the IEC standard, while also ensuring the PV modules continue to produce maximal power.

2.3.3 Solar Cells

Solar cells are connected in series and then encapsulated, typically with EVA, to provide adhesion between the solar cells and the protective glass. Failure of the solar cell mainly occurs due to the very narrow profile of the pure silicon slice. These thin wafers are very brittle and are prone to cracking easily during manufacturing or transportation.

Generally, the microcracks of the cell cannot be detected by the naked eye. Due to that, they may spread and distribute to other cells in the module [36]. When the cracks block more than 8% of the cell from functioning, it may lead to a hotspot [36, 101]. The active area of the cracked cell may be forced to operate in reverse bias, eventually causing a hotspot failure. Moreover, cracks are subject to expansion and emerging more cracks, especially under environmental and mechanical stress factors from hot, cold, and windy climates [102-105].

Consequently, it accelerates the ageing process and causes a faster degradation rate [36]. Buerhop *et al*. [106] reported that PV modules with cracked cells had a greater than 10% power loss after six years of operation only.

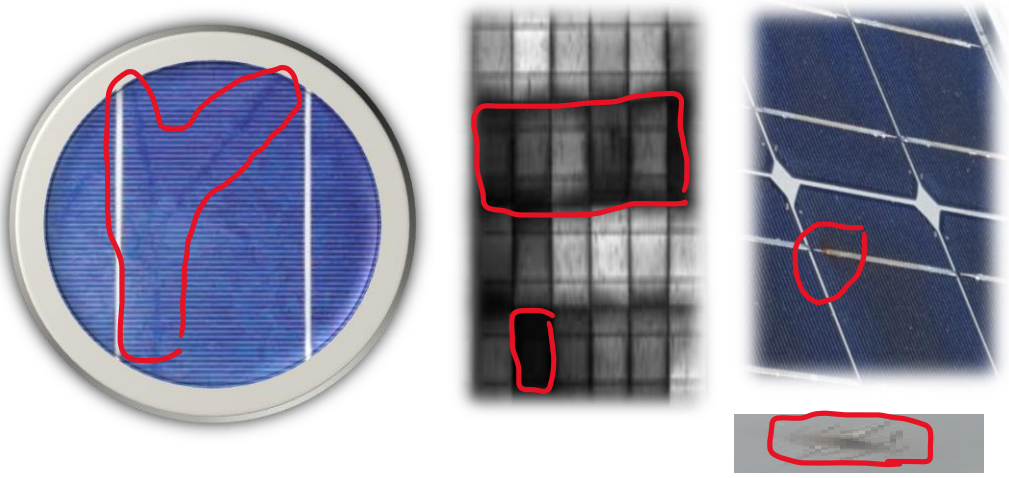
Conversely, snail track failure can be detected by the naked eye; this failure is so-named because it is shaped like a snail. Alberto *et al.* [107] indicated that most of the snail track failures are linked to the existence of cracked cells. They also compared four PV modules with a snail track against a healthy one. In their findings, the maximum power output dropped in all PV modules with a snail track, one of which had a power loss of 40% than rated. This reduction in maximum power was caused primarily by a significant reduction in the I_{SC}, despite a slight increment in open-circuit voltage (V_{OC}). Duerr *et al*. [108] found that four degradation mechanisms trigger snail track failures, depending on the combination of the encapsulant materials, and, on that basis, snail tracks should be described and categorised under PV failures rather than a single degradation mechanism.

Potential induced degradation (PID) is another PV failure observed firstly in Germany in 2005 [109]. It degrades PV wafers and leads to the development of hotspots [110, 111]. If undetected, it may lead to 100% power loss within a few years [58]. A report based in Germany stated that PID failure is progressing rapidly with the release of acetic acid due to EVA discolouration [112]. Moreover, in a lab experiment by Pingel *et al.* [113], the PV module was found unlikely to recover from PID when operated at higher temperatures.

Another failure that solar cells might experience is a disconnection of the solar cell wires known as busbars or ribbons. This type of failure occurs because of a manufacturing defect, it is also driven by excessive heat due to long partial shading. Such failure is detected by an infra-red camera (IR) or by monitoring the output *I-V* curve. When this occurs, the power is dropped by 35%. With progression, it will decrease the power by 46% [33]. Consequently, solder bound will become

extremely hot, leading to burning marks and discolouration of the EVA encapsulant [114]. In the worst scenario, the protective glass will be broken with visible burn marks on the PV module's back sheet, blocking the current path and initiating an electrical arc and fire, causing irreversible damage [36].

Thus, as with most PV failures, detecting them earlier is essential to assure a reliable and safe operation of the PV system.



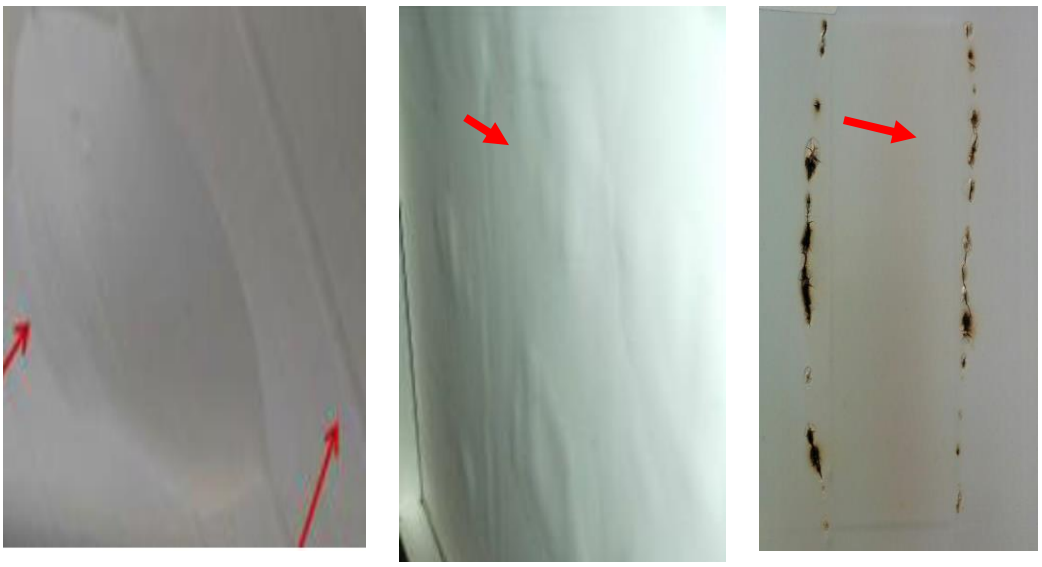
(A) (B) (C)

Figure 2.4 (A) PV module affected by snail track failure [108]. (B) PID failure detected by electroluminescence image [115]. (C) Hotspot burned the cell solder bonding and exhibited burn marks in the back sheet [116].

2.3.4 Backsheet

The backsheet is the last layer of the PV module that provides construction support and protects the modules' electrical parts from short circuit failure, ensuring perfect electrical insulation from various environmental stress factors such as water ingress from high relative humidity [117]. Failures and degradation

in the backsheet can appear as discolouration, delamination, bubbles, and burn marks [112].



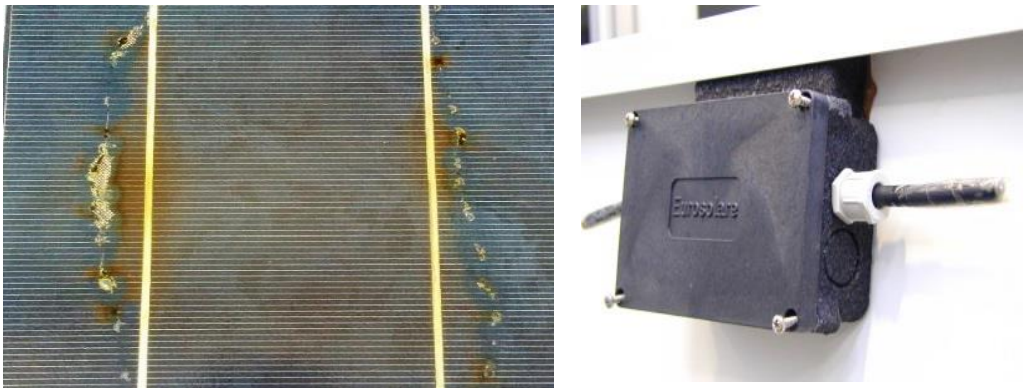
(A) (B) (C)

Figure 2.5 (A) Backsheet bubbles [112]. (B) Backsheet delamination [112]. (C) Burn marks were caused by a hotspot in the backsheet [116].

The major cause of burn marks failure is hotspots, and this may lead the PV module to catch fire. For this purpose, a study conducted by Cancelliere and Liciotti [95] investigated fire reaction with four common types of backsheet materials: 3-layers (PET/PET/Primer), 4-layers (PET/Aluminium/PET/Primer), 3-layers (Fluoro-Coating/PET/EVA) and PET layer with an outside and inside coating. The two backsheets, PET monolayer with an inside and outside coating, and the 4-layers (PET/Aluminium/PET/Primer), reacted slower to fire flame and had fewer damaged areas with no or less harm to EVA encapsulant. However, the monolayer with an inside and outside coating backsheet is favoured over the other as aluminium is electrically conductive and may result in less power production of the PV module.

2.3.5 Junction Box and Bypass Diodes

A junction box (j-box) is attached to the PV module through adhesive material to regulate and provide a safe flow of the PV module current [118]. To guarantee the proper flow of the current, bypass diodes are also installed inside the j-box in different configurations; overlap and non-overlap [119]. Failures in the j-box are mainly caused by bad wiring quality, blown bypass diodes, and poor bonding to the PV module (delamination) caused by high humidity [72]. Those failures allow water vapour to ingress, causing serious safety issues initiating an electrical arc or causing hotspots [36]. Han *et al*. [31] investigated the condition of 177 mono-crystalline PV modules that operated for 22 years in a humid climate with an average temperature of 27.5°C. Most of the junction boxes of the modules had been seriously damaged and needed replacement.



(A) (B)

Figure 2.6 (A) Failed bypass diodes led to hotspots [116].(B) Poor bonding of j-box [115].

Several PV failures were found to form hotspots making it necessary to protect the PV module. One means of protection is to use a bypass diode, although it has been criticised for being neither safe nor effective [69, 120, 121]. The existence of a bypass diode enables the current to flow over the defective solar cells, thereby

protecting the PV module from thermal increases and hotspots. This is one of the main reasons why some PV manufacturers, such as AE-Solar, a German PV Manufacturer, attach a bypass diode to each PV cell [122]. One of the frequent reasons for blown bypass diodes is the increase in their temperature due to long-term shading [123, 124]. Also, it was indicated by Bansal *et al*. [72] that bypass diodes exposed to over irradiance, in particular over 1400 Wm^{-2} are expected to be blown due to high flowing currents and high operating temperature.

Failure to detect poor bypass diodes may lead to serious safety issues [124, 125]. Since bypass diodes are used to avoid PV failures that lead to hot-spotting, whenever they fail, the module loses its means of protection and becomes vulnerable to hot-spotting and burn marks and, in the worst scenario, fire [42, 126].

2.4 Classification of Crystalline Photovoltaic Module Failures

Failures can be classified into different criteria based on the severity, location of the failure, and occurring time, whether at the early installation or the last years of warranty. Kuitche *et al.* [127] classify the failure types based on severity level, the severity of failure was mathematically estimated using Eq. (2.1) [127].

$$RPN = S \times O \times D \qquad (2.1)$$

Where RPN is defined as the Risk Priority Number used as a rating guideline,

S: is the severity rating and it is rated from 1 to 10. Where one refers to no apparent defect and 10 indicates no operation.

O: failure occurrence, and it is rated from 1 to 5. One indicates failure is less likely to occur, and 5 indicates a frequent occurrence at least once per month.

D: detection of the failure and rated from 1 to 10. One indicates the failure will be easily detected, and ten less likely to be spotted.

Table 2-1 Photovoltaic failures list classified by three different reviews.

Photovoltaic Failure	**Classified by Jordan *et al.* [52]** **Classification Categories:** **Severity 1 to 10**.	**Classified by Tsanakas *et al.* [58]** **Classification Categories:** ***a) Optical*** ***b) Electrical*** ***c) Not Classified***	**Classified by Köntges *et al.* [36]** **Classification Categories:** **a) Infant-Life** **b) Midlife-** **c) Wear Out**
Hotspot	10	Electrical	Not Classified
Delamination	Minor Delamination:1 Major Delamination: 5	Optical	Mid-Life
Encapsulant Discolouration	3	Optical	Mid-Life
Solder Bonding	8	Electrical	Wear Out
Glass Breakage	5	Optical	Early Life
Cracked Solar Cell	5	Electrical	Mid-Life
Bypass-Diode	5	Non-Classified	Mid-Life
Junction-Box Failure	5	Electrical	Infant-Life

Similarly, Jordan *et al.* [52] adopted Eq. (2.1) to extract a classification method based on the severity. They rated the severity measurement from 1 to 10, where one indicates there is no effect on the performance of the PV module and 10 points a severe impact on the performance accompanied by a safety hazard. Within

their classification, hotspot failure ranked 10, and a minor delamination failure rated 1. Tsanakas *et al.* [58] classified the PV failure differently based on optical and electrical shortages, as seen in Table 2-1.

Kontges *et al.* [36] classified PV failures into three categories: infant-life, mid-life, and wear-out failures based on the expected time of occurrence. Infant-life failures are the ones that appeared in the early life of PV operation. Mid-life failures arise after eight years of operation, whereas wear-out failures are failures that emerge just before the end of the module lifetime.

2.5 Environmental Stress Factors that Trigger PV Degradation

Harsh weather in some geographical locations in the world reduces the PV module's efficiency and triggers degradation. High temperature, high relative humidity, dust storms, snowstorms, and high UV index, all of which are aspects of environmental stress factors. For instance, the PV power production reduces when operated above 25 ºC [128, 129].

2.5.1 PV Failures Triggered by Harsh Weather

Potential induced degradation, encapsulant discolouration, and delamination failures were listed to be triggered by high ambient temperature [36]. Humidity triggers the adhesion of the module's back sheet and raises a safety concern in the system when water vapours penetrate the module's parts [36]. J-box failures are also triggered by high ambient temperature and humidity [31]. Dust particles and snowing were found in the literature to cause shading failures and reduce power output significantly [3]. Both extreme cold and hot climates were found to increase the degradation rate of PV modules with cracked cells [115, 130, 131].

2.5.2 Temperature and Humidity

Humid weather contributed more to failing the j-box as it deteriorates the bond force of cohesive material [132]. After Han *et al*. [31] found that most j-boxes needed replacement due to humid weather, they selected 144 modules and installed them in harsher weather. As a result, the degradation rate doubled, jumping from 0.18% to 0.43% per year. PID failure is also more likely to occur in humid weather [133].

Santhakumari and Sagar [132] reviewed the literature focusing on failures related to the weather condition and their contribution to the degradation of the photovoltaic system components, including batteries, cables, and inverters. Their review concluded that high ambient temperature, relative humidity, dust, sandstorm, and hailstorm highly trigger PV failures, causing optical and electrical losses. These environmental stress factors are found to trigger encapsulant degradation, corrosion, and glass breakage. The review [132] also addressed some of the experiments that have been conducted to tackle harsh environmental stress factors. For instance, sprinkling water on the PV panels was an efficient technique to reduce the thermal temperature.

A study was conducted by Chandel *et al*. [67] investigated the degradation rate and failures for mono-crystalline modules operated for 28 years in India. The kinds of failure classified by Santhakumari and Sagar [132] due to humid climates were found with an average degradation rate of 1.4%.

2.5.3 Dust and Dust Storms

Dust accumulation is another environmental stress factor that decreases the power output by causing shading on the PV surface, it occurs in locations where dust storm is common like the Middle East and Africa. The dust particles are either

scattering in the atmosphere or accumulating on the PV module surface [134]. When dust scatters radiation in the atmosphere, it minimises the irradiation reaching the earth's surface and converts it to diffuse irradiance, reducing the overall power. In contrast, dust accumulation on the PV surface directly impacts the power output and thus brings more attention to be studied and investigated more extensively. It motivates researchers who live in a harsh weather environment to conduct more studies during dust storms [135], while others have set up lab experiments to investigate different dust particles properties on PV modules [136, 137].

Saidan *et al.* [135] compared the electrical parameters between PV modules at different periods of dust accumulation. They found that reducing short-circuit current and the power output became greater for a longer time of dust accumulation. I_{SC} was decreased by fourfold in dust accumulation for one month when compared to one day. Said and Walwil [138] reached the same results in a previous study for PV modules deployed in Dharan, Saudi Arabia; the I_{SC} reduced greater in a more extended time of dust accumulation.

Many factors need to be considered to address PV dust accumulation; tilt angle is one of them. Sayigh *et al.* [139] experimented with PV modules operated in the field for 38 days at different tilt angles ranging between 0^o to 60^o. They found that dust accumulation increased dramatically when the tilt angle decreased, causing a reduction in the PV transmittance. This was also experimented and confirmed by Said and Walwil [138]. Both Elminir *et al.* [140], and Said and Walwil [138] showed that the dust accumulation increased fivefold at a tilt angle of 0^o compared to a tilt angle of 90^o.

Properties of dust particles, weather conditions, and dust adhesion force also play a vital role in tackling the dust accumulation problem. For example, the

adhesion force for the larger dust particles was higher than the smaller ones [137, 138].

A lab experiment conducted by Mehmood *et al.* [136] identified the material components of the dust particle found in Dhahran, Saudi Arabia and their mud character when they react with humidity on two PV surfaces: glass and polycarbonate. The dust particles collected from the PV modules surface, mixed with different concentrations of deionized water, applied to the glass and polycarbonate, and then dried for two days. Their results showed that glass's transmittance reduced more by 9% when compared to the polycarbonate. Therefore, it is essential to monitor the PV module surface to ensure no dust accumulation or dirt. This was reported to cause a decrease in the power efficiency by 18% after only a month of accumulation [135].

2.6 Detection of PV Failures

Depending on the connection types of the PV system, whether it is grid-connected or a standalone, failures occurred on two different sides DC and AC. They happen on the DC side when the system is standalone, whereas they also exist on the AC side when connected to the grid. Distinguishing them can be achieved by monitoring the system's power output; it reduces whenever there is a DC failure but causes a total blackout when a failure occurs on the AC side [141].

Madeti and Singh [141] reviewed the literature and classified all failures detection techniques into two groups; fault detection based on the ground by employing monitoring sensors and fault detection based on a space monitoring system. The latter group is cost-effective because it does not require sensors, but weather situations can reduce its accuracy significantly. The sensors employed in ground-based techniques are set to observe the major electrical parameters such are current, voltage, and power. These parameters vary based on the PV system's

connection type; for example, grid impedance needed to be monitored in a grid-connected system, but not in a standalone system [141].

Each type of PV failure requires a different strategy to be detected. For example, detection strategies employed in optical failures are different from those employed in electrical failures. Optical failures may be seen by the naked eye, whereas electrical losses require instruments to monitor, store data, and analyse. Furthermore, detection techniques for failures on the AC side, e.g., PV converter, power blackout of the grid, are utterly different from those on the DC side [141]. On the grounds that failures found in the PV module are listed under the DC side, details about detection techniques of losses that occur on the AC side will not be covered as they are beyond the scope of this thesis.

To the best of the author's knowledge, there are nine comprehensive reviews of PV failures in the literature: Madeti and Singh [141], Bansal *et al.* [72], Santhakumari and Sagar [132], Triki-Lahiani *et al.* [6], Flicker *et al.* [142], Mellit *et al.* [143], Pillai and Rajasekar [144], Rahman *et al.* [145], and Pillai and Rajasekar [47]. In this regard, the review of PV failures detection techniques of the DC side uses these sources.

According to Pillai and Rajasekar [47], for the detection technique to be effective, it should meet the following criteria: (1) Able to detect failures without interfering power or causing blackout (2), Able to pinpoint the failure, (3) Cost-effective and flexible (4), Simple and not complicated in structure and (5), Can be applied to different variety of PV systems.

Madeti and Singh [141] classified failure detection techniques of the DC side into six categories; electrical characterization, infrared imaging, visual inspection, ultrasonic inspection, electroluminescent imaging, and lock-in thermography. Nearly the same classification was presented by Santhakumari and Sagar [132], but in fewer details, the electrical characterization was also referred to as indoor

testing using the solar simulator. Twelve detection techniques were under electrical characterization listed in the Madeti and Singh [141], five of them reviewed in more detail by Mellit *et al.* [143]. Those five techniques were signal and processing, *I-V* characteristic analysis, power loss analysis, voltage and current monitoring, and machine learning detection techniques.

2.6.1 Visual Inspection

The first step to detect PV failure is to view the PV modules from different angles. Visualizing techniques have been demonstrated and reviewed by the international standard IEC 61215 [146]. The standard considered broken, cracked, and misaligned module surface as well as bubbles of the encapsulant as significant defects. Failures such are delamination, mild discolouring, corrosion, j-boxes, and shading could be visualised by naked eyes without employing other detection techniques [72, 143]. Moreover, some researchers proposed using drones with installed cameras to visualize PV plants more effectively, e.g., [147].

2.6.2 Infrared Imaging

Infrared imaging is a detection technique based on the solar cell's reversed biased circulating current in a PV module. In case of failure, the solar cell dissipates heat which an infrared camera can detect. Hotspot, as well as microcracks failures, sometimes cannot be seen by the natural human eye. Still, they are caught by infrared imaging. Predicting failure before taking place is a major advantage of this technique. On the other hand, drawbacks will be staffing and expensive costs [47].

The working principle is usually started by storing images of a healthy PV module to compare them to a faulty module when needed. This technique

can detect hotspots, breakage of solar cells, disconnection, and PID failures [72].

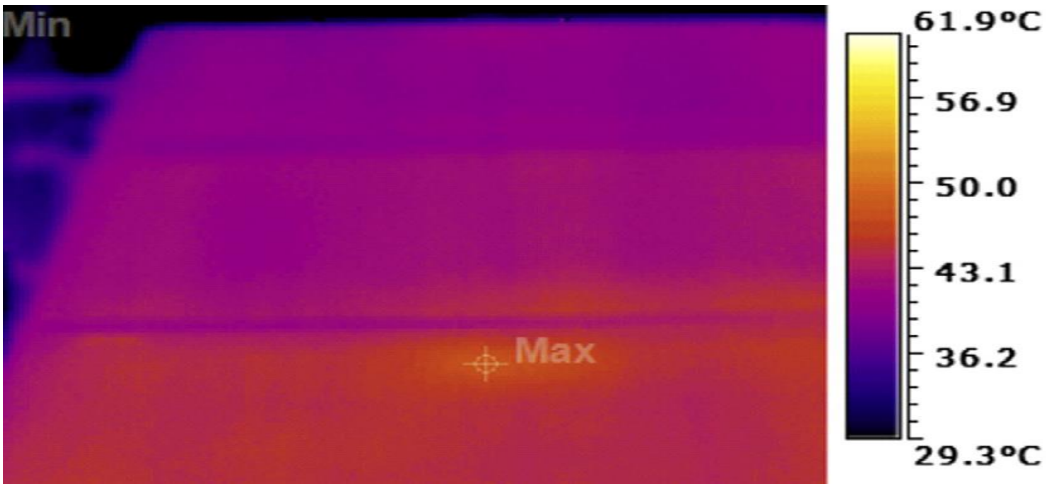
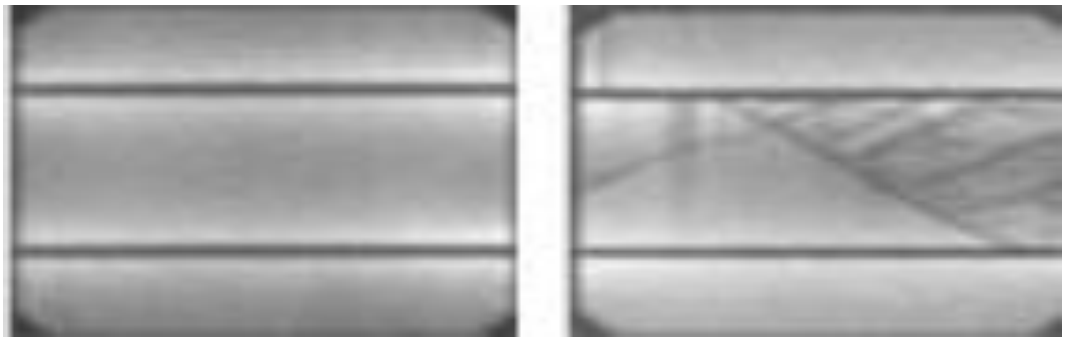


Figure 2.7 Infrared imaging to discover high-temperature cells in a PV module [47].

2.6.3 Electroluminescence Imaging

This technique is used to detect a potential cracked cell by pinpointing the low contact area of a PV module. The working principle of this technique is to look into the recombination losses (shunt defects) created by an injected current to the solar cell metallic contact [148-150]. In addition to detecting cracked cells, snail tracks, and PID failures can be seen using EL imaging [72].



(A) (B)

Figure 2.8 (A) EL imaging of a healthy monocrystalline solar cell. (B) El imaging of a cracked monocrystalline solar cell [151].

The lock-in thermography detection technique has nearly the same working principle as EL but was found superior and more sensitive in detecting failures [122].

2.6.4 Ultrasonic Inspection

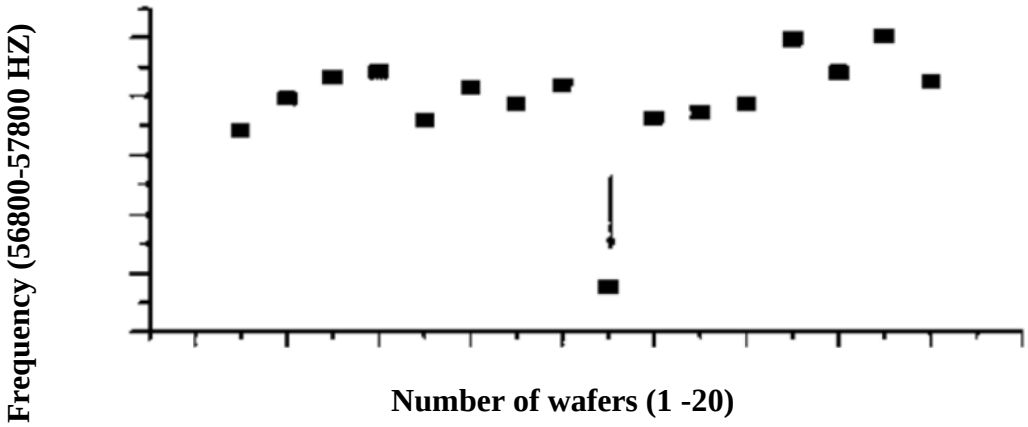


Figure 2.9 Ultrasonic inspection for several cell wafers showing cell No.11 has an abnormal reduction in frequency, indicating a crack failure [152].

The detection technique of ultrasonic inspection compares the frequency signals of a healthy and a faulty cell obtained by an ultrasonic transducer [152-154]. The resonance frequency intends to decrease when detecting a defective cell [153, 155]. The ultrasonic technique is mainly used to detect cracked cells in the PV module. An advantage of the method is that it determines the level of the crack based on the increased range of the frequency's bandwidth [153].

2.6.5 Electrical Characterization

Electrical characterization has been claimed to be the most common detection technique of PV failures [144]. This detection technique focused on monitoring the PV system's electrical parameters and was referred to as a signal processing approach by Mellit *et al.* [143]. Mellit *et al.* [143] also reviewed protection devices

used for electrical characterization, such as over-current protection devices. Pillai and Rajasekar critically reviewed detection devices [47], explaining the limitations and drawbacks of detecting a failure at the time of occurrence, particularly under low irradiance, which may lead to serious safety issues and catastrophic failure. For instance, over-current protection devices might respond slowly to PV failure, leading to an electric arc or fire [143].

I-V curve, power losses, and PV module's temperature, all of which can be used to detect PV failures. For instance, the temperature of the PV module increases at hotspot failure, fuses calculate the residual system's current. Insulation monitoring devices evaluate the resistance between the current-carrying conductor and the ground to detect ground failure.

2.6.5.1 Effect of Noise in Detecting Photovoltaic Failures

One obstacle preventing accurate detection of PV failures was obtaining noisy data from measurements. Harrou *et al.* [156] focused on detecting four types of PV failures on the DC side; open circuit, short circuit, partial shading, and degradation failures. They used a wavelet-based multiscale tool to separate the noise measurements data to detect those failures accurately. Elyes *et al.* [157], also concluded that using wavelet-based multiscale, anti-noise techniques better detects PV failures. Noisy data seems to be an obstacle in Ali *et al.* [158] ending up suggesting to separate them using noise separation devices or working out efficient ways for noise separation.

2.6.5.2 Detection of PV Failure Using Current and Voltage Residuals

This method used the values of maximum voltage (V_m), maximum current (I_m), and power obtained from the healthy PV module simulation to compare them with actual data. Residuals or the difference between the simulation and the

experimental values indicate the existence of PV failure. Depending on residual values, the type of failure can be predicted [156, 157].

Harrou *et al.* [156] used the measurement of the MPP residuals of voltage, current, and power as indicators of abnormal changes in the PV system. However, it was concluded that the monitored parameters were insufficient to detect degradation and partial shading failures. Thus, it will be more effective to include other parameters as an indicator. Elyes *et al.* [157] used the residual technique and reached the same result as Harrou *et al.* [156], particularly for shading failures, other *I-V* parameters such as short-circuit current and fill factor should be included to improve the detection technique.

2.6.5.3 Detection Techniques Using I-V Curve Parameters

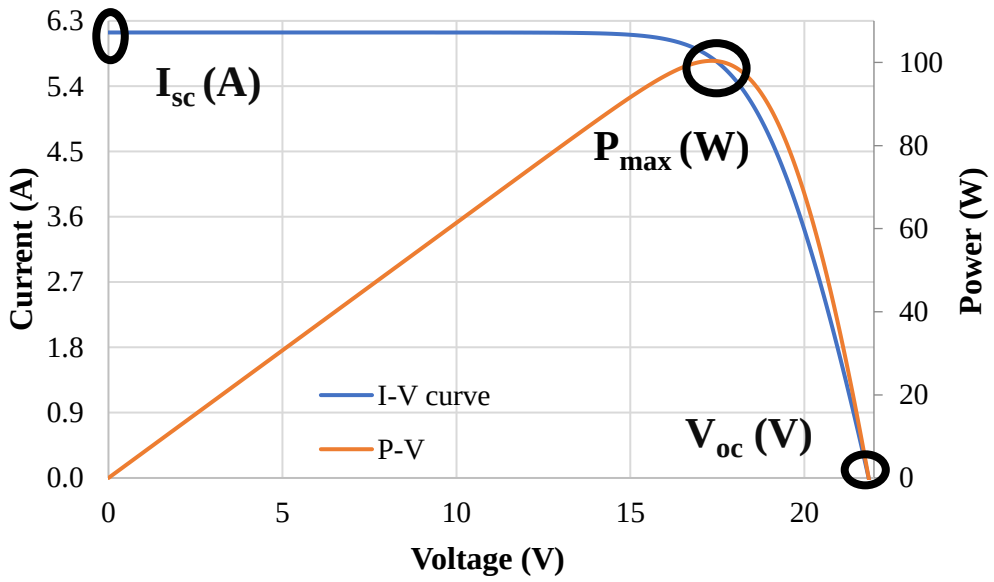


Figure 2.10 Current-Voltage and Power-Voltage curves display the major parameters of a solar cell; I_{sc}, the current at zero V, V_{OC}, the voltage at zero current, and P_{max}, the maximum point at the voltage and current.

The *I-V* curve shows the output combinations between voltages and currents, delivering the values of major parameters; short-circuit current, open-circuit

voltage, maximum power output, and fill factor. Modelling of healthy or expected *I-V* curves and power output via engineering modelling programs are also classified under electrical characterization and was referred to as "model-based difference measurements" by Pillai and Rajasekar [47].

One of the reasons for the *I-V* curve to be simulated, instead of obtaining them experimentally, is the risk associated with performing faulty operation scenarios in a real PV system which may get out of control [159].

Chen *et al.* [160] investigated four failure modes and records their impacts on the *I-V* curve. Short circuit failure was found to decrease both P_{max} and V_{OC}. Degradation failure can be observed when a reduction in the *I-V* slope accompanies a gradual decrease in P_{max}.

I_{SC} was decreased in open-circuit failure. In case of partial shading failures, the *I-V* curve will be distorted, forming multiple P_{max} points; one before shading and one after shading. Ali *et al.* [158] fabricated three shading scenarios on a PV string that contains three polycrystalline modules; firstly, where one-third of two modules were shaded, secondly, three cells in each module were shaded and lastly, half cells in each module were shaded. As a result, *I-V* curves were distorted, and V_{OC} decreased in all three scenarios, at most in the third scenario with a 68% reduction.

Köntges *et al.* [36] agreed with Ali *et al.* [158] that shading failure distorts the *I-V* curve, creating multiple P_{max} points. They also listed the effect of various PV failures on the *I-V* curve; I_{SC} is affected mainly by optical failures and losses of transparency, EVA discolouration, glass breakage and shattering, and EVA delamination. It is also affected by disconnected soldering of the cells, PID, and cracked cells in the PV module. Whereas V_{OC} is affected by defective bypass diode, PID, and disconnected soldering of the cells. The fill factor is affected by

delamination, corrosion, and cracked cells. All PV failures were found to reduce P_{max} except for the bypass defect.

2.6.5.4 Using I-V Characteristics to train machine learning (ML)

The awareness of the electrical characterization's boundaries assists in training supervised machine learning algorithms to detect PV failure and degradation. Chine *et al.* [161] implemented artificial neural networks (ANN) to detect eight types of faults: shading caused by snow and soiling. A probabilistic neural network (PNN) algorithm was implemented and compared to ANN to predict and classify three failure mechanisms by Garoudja *et al.* [159]. It was found that PNN is superior to, and more efficient than ANN even in the presence of noise.

2.6.6 Detection Degradations and Failures Using Shunt Resistance

Formulation of the *I-V* curve's major parameters with mathematical equations helps to extract the values of other hidden parameters [162, 163], namely series resistance (R_s) and shunt resistance (R_{sh}). Measurement of these parameters is vital for detecting some PV failure and degradation modes [164]. However, accurate extraction of R_s and R_{sh} values is challenging [162, 163]. For this purpose, many studies have attempted to refine and optimise an extraction approach to estimate these values, e.g., [165-169]. Though an exact identification might be unobtainable, approximating their range of values is still important.

The shunt resistance is a parallel resistance across the $p-n$ junction; a higher shunt resistance indicates fewer photogenerated currents flow through alternate paths [170, 171]. A reduction in R_{sh} means that photogenerated carriers are being lost, causing a reduction in the overall power production [170-172]. Kaplani and Kaplanis [173] tested PV modules that operated for 20 years. They found that 11% of the module's power loss was associated with an 80% shunt resistance reduction, making it a strong indicator for critical PV degradation [73, 164].

Additionally, the R_{sh} indicates the occurrence of PV failures such as soldering defects, cracks, shading, and mismatch [174, 175]. Most of the failures listed by Tsanakas *et al.* [58] (Section 2.4) specifically electrical failures, were found in the literature to lower shunt resistance.

Optical failures such as EVA delamination were found to lower shunt resistance. Gxasheka *et al.* [176] compared parameters of five deployed PV modules, the one affected by delamination had approximately 50% lower shunt resistance. The effect of EVA discolouration was determined by Rajput *et al.* [177] to lower shunt resistance. However, when the solar module is affected by EVA discolouration, it receives less illumination [178]. And according to Ruschel *et al.* [179], the shunt resistance increases when solar illumination decreases. Based on that, the shunt resistance should be increased if EVA experienced the same discolouration colour across the PV module. Otherwise, different colours of EVA discolouration might have the same effect as shading and will lead to a decrement in shunt resistance. A study by Sinha *et al.* [180] compared two module pairs that operated for 20 years in India, one in each pair had brown EVA discolouration. They assumed no evident link was found between brown EVA discolouration and shunt resistance.

On the other hand, [58] electrical failures, which are unlikely to be detected by visual inspection, such as microcracks failure, were found by Zhang *et al.* [181] to decrease R_{sh} significantly. Low shunt resistance was spotted from the short-circuit current slope from the *I-V* curve of a module with cracked cells [181]. Saavedra *et al.* [182] also experimentally investigated PV modules with cracked cells and reached the same conclusion as Zhang *et al.* [181]. Potential induced degradation was also directly linked with shunt resistance reduction [183, 184].

Myer and Dyk [185] simulated a PV module that consisted of 36 cells with 30% of the cells under shading failure to analyse the effect of shading on electrical

parameters. In their findings, both shading and hotspots, when presented, significantly lowered the shunt resistance. Shading failure is another common PV failure that is also strongly linked with hotspot formation [171, 185]. Failures related to soldering defects can produce excessive leakage current. When undetected increased the thermal temperature and formed a hotspot [182].

Degradation and many PV failures were associated with low shunt resistance, making it vital to investigate the behaviour of the solar cell when the shunt resistance degrades. A simulation study by Dhass *et al.* [186] developed a MATLAB model showing that there was a greater reduction in I_{SC} rather than V_{OC} as the shunt resistance degraded. In contrast, Sarkar [7] used SPICE simulator and found that degradation of R_{sh} results in a greater reduction in V_{OC} than $I_{SC.}$ These discrepancies in their results [7, 186] arise because both studies were based on simulation. Dyk and Meyer [187] used PVSIM to investigate the effect of lowered shunt resistance. They showed that low shunt resistance decreased maximum power output, open-circuit voltage, and fill factor but increased short-circuit current slightly.

Experimental studies were also undertaken and reported; in 1969, Kennerud [188] solved the *I-V* equation for a cadmium sulfide (CdS) solar cell using the Newton-Raphson technique and varied the electrical parameters, including shunt resistance, to explore their effect on the *I-V* curve. The results obtained were compared and verified experimentally and showed that lowering shunt resistance reduced V_{OC} and fill factor. Rummel *et al.* [189] used a 12-cell mono-crystalline PV module to investigate the effect of three low shunt resistance values at eight irradiance levels decreasing from 1 kW m^{-2} down to 0.09 kW m^{-2}. They compared the module efficiency before and after lowering the shunt resistance and found that the module's efficiency decreased dramatically with lowering shunt resistance.

Roy and Gupta [172] presented electroluminescence (EL) imaging techniques to quantify shunt resistance and detect unhealthy levels associated with PV failures like mismatch and hotspot failures. They investigated six shunt resistance values reducing from 300 Ω to 1 Ω. The areas displaying reduced shunt resistance appeared darker in EL imaging with the level of darkness increasing with reducing shunt resistance.

2.7 Conclusion

Most literature reviews of PV failures are based on the severity and frequency of occurrence of failures. This chapter takes a different perspective and focuses on failure mechanisms based on PV module components, reviewing each component's vulnerability to failures. Table 2.2 compares classification methodology by widely-cited articles and classification methodology followed in this chapter. Looking into the literature in depth allows for extracting the root cause of some failure and degradation mechanisms. For instance, UV, one of the environmental stress factors, is considered the root cause of the most common degradation, i.e., encapsulant EVA discolouration. Most optical failures, such as corrosion and delamination, are caused by EVA discolouration. Shading glass breakage and soldering defects can cause hotspot failure. This is applied with most PV degradation mechanisms; they lead to disastrous consequences, including human fatalities, when undetected or neglected. For this reason, the review emphasises the necessity of early detection of failures. Devices for detecting specific types of failures, such as cell cracks and hotspots, were developed. Most of these are costly, require more labour work and are time-consuming.

Shunt resistance was linked with most PV failures, particularly those classified under the electrical category. Both EVA and shunt resistance degradations impacted the *I-V* characteristics when PV module operation entered faulty or degraded modes. Furthermore, *I-V* monitoring was considered in the literature as a

typical detection technique under electrical characterization. This paved the road for the following chapters to conduct investigations of *I-V* measurements under the two dominant causes of extreme degradations: EVA discolouration and low shunt resistance. Thereby allowing models to be developed in a simple, applicable, comprehensive, and novel way to facilitate early intervention to avoid catastrophic deterioration and ensure continued safe and productive operation of the PV system.

Table 2-2 Comparison between the chapter's classification methodology and some scientific articles' classification methodology in the PV area.

Scientific Articles versus Existing Work	Classification Methodology
Köntges *et al.* [110].	The time when failures and degradation often occur.
Jordan and Kurtz [52].	Based on the severity ranking of PV failure or degradation mode where 1 referred to no effect on PV system and 10 referred to harmful effect on PV power and safety.
Pillai and Rajasekar [47].	Based on failures due to environmental stress factors and failures that physically appeared in the PV module.
Madeti and Singh [141].	Permeant failures such as delamination of EVA encapsulant versus temporary failures such as shadings from snow or dust covering.
Existing Work	Failure mechanisms based on PV module components, reviewing each component's vulnerability to failures.

3 Chapter 3| Early prediction of EVA Degradation in PV Modules from Short-Circuit Current Measurements

In Chapter 2, the literature review illustrated that most optical failures are caused by EVA degradation, which emerged as discolouration. The experimental studies have shown that significant reduction in the optical transmission due to EVA degradation leads to loss in short-circuit current and the available power by more than 50%. Accordingly, this chapter uses an electrical circuit simulator (SPICE) to evaluate the short-circuit current obtained from *I-V* measurements under varying optical transmission caused by EVA discolouration. A novel approach to predict the early degradation of EVA encapsulant was proposed by correlating EVA degradation with I_{SC}. Results showed that the reduction in I_{SC} due to EVA degradation differed from the reductions expected due to a spectrally-uniform reduction of the solar irradiance intensity. Both types of variation were linear, however, the slope due to EVA degradation was larger than the slope obtained for normal intensity variations in the solar irradiance. Therefore, the proposed model when applied, in conjunction with solar irradiance measurements, in monitoring system can predict the early onset of EVA encapsulant failure, thereby enabling preventative measures to be taken.

3.1 Introduction

Degradation of encapsulation occurs over time after prolonged exposure, typically years, of the PV module to UV light. Additional stress factors might expedite the degradation process, for example, degradation was observed to commence between 1-5 years of deployment in a humid, hot climate [190]. However, there is not a consensus in the literature as to the time required to reach the failure point as it depends on several stress factors and not only UV

exposure. Environmental stresses such as temperature, hailstorms, or sandstorms also contribute to the degradation process [80, 95].

In general, degradation and failures appear in PV encapsulation as discolouration, bubbles, corrosion, and most catastrophically delamination [52, 191, 192]. Among them, discolouration is the most common failure [72]. Delamination will lead to a significant reduction in absorbed light, thereby resulting in a dramatic reduction of short-circuit current. This, most likely, occurs long after the effects of discolouration have been observed.

Pern *et al.* [97], demonstrated the difference in transmittance between five different encapsulants, some of which were exposed to natural weathering for more than five years. For analysis, the EVA encapsulants were classified using their evolving colour i.e., from yellow to dark brown, and the difference in their electrical performance when attached to the solar cell was compared. The first encapsulant was non-exposed, the second and the third encapsulants had a yellow-brown colour, the fourth had brown colour and the fifth had a dark brown colour. They also found that in discoloured EVA, the reduction of EVA absorption toward longer solar wavelengths did not occur homogeneously in the PV module, i.e., discolouration of EVA varies from one solar cell to another in a PV module. This forms the basis for the model presented here.

This chapter used SPICE to model the influence of EVA degradation on the performance of solar cells using experimental results from Pern *et al.* [97]. Firstly, the SPICE model and its use are explained in more detail. Secondly, a comparison between the short-circuit current density (J_{SC}) resulting from reduced transmission through degraded EVA and the corresponding J_{SC} resulting from the equivalent absorbed power density from the solar spectrum is demonstrated. Thirdly, the results show that the differences in the slope of measured short-circuit current can be used as an indicator of early onset of degradation of the EVA.

3.2 Overview of the SPICE Model

SPICE is a long-established tool for electrical simulation of circuits. It was originally established and innovated by Nagel and Pederson in 1973 [193]. Since then, it has been adopted into a significant number of simulations to study and investigate PV systems. Bhide and Bhat [194] adopted SPICE to simulate *I-V* characteristics of PV modules under different climate conditions. Due to its simplicity and availability of a wide range of electronic elements, it was adopted to simulate a standalone PV system by Castañer *et al.* [195]. After that simulation to test the quality of PV inverter signal was also carried out by Simmons and Infield [196].

A study of load management conducted by Moreno *et al.* [197], adopted SPICE as conventional loads in a PV system. Castaner and Silvestre [5], who published many studies about PV simulations via SPICE, authored a book that demonstrated the adaptation of SPICE to modelling solar cells and modules. The approach outlined in that book has been adopted to the specific problem of modelling the effects of reduced optical transmission through the encapsulant.

The SPICE model has followed the three steps to determine the effects of encapsulant discolouration:

Step.1: Calculation of the transmitted solar spectrum, which was obtained by multiplying the transmittance of the EVA by the AM1.5G solar spectrum.

Step.2: Simulation of the short-circuit current density, generated from the calculated solar spectrum from Step 1.

Step.3: Using the simulated short-circuit current density obtained in Step 2 to simulate the solar cell's *I-V* curve.

The simulation informed the effects of encapsulation degradation on the PV module performance and may be used to identify early-onset degradation of the EVA.

3.2.1 Standard Solar Spectrum (AM1.5G)

The standard spectrum for PV terrestrial applications is set for air mass 1.5 [198-200]. Air mass is defined in [[201],p.1] as "the path length of the direct solar beam through the atmosphere" and can be calculated as shown in Eq. (3.1) [5] following formula:

$$AM = \frac{1}{\cos \vartheta_z} \tag{3.1}$$

Where ϑ_z is the zenith angle. Using SPICE, the standard AM1.5G spectrum was taken from Hulstrom *et al.* [202] and written as a Piecewise linear (PWL) source sub-circuit by Castaner and Silvestre [5]. In SPICE the PWL source simplifies the simulation parameters in one source. Thus, changes in any of the source's parameters will be reflected in the simulation results. As mentioned earlier, when optical transmission properties degrade, the PV module will absorb less of the solar spectrum at specific wavelengths. Such a scenario can be simulated by reducing the intensity of some of the wavelengths in the solar spectrum. A greater degradation in the encapsulant will lead to a reduction in the intensity of the transmitted spectrum to the solar cells.

Figure 3.1 shows the difference between the standard AM1.5G spectrum and the standard spectrum when reduced uniformly by 10% across all wavelengths. The resulting solar irradiance decreases from 994.5 Wm^{-2} to 895 Wm^{-2}, where the total irradiance can be calculated by using numerical integration of the spectrum from Eq. (3.2):

$$\int_a^b f(x)\ dx \approx (b-a)\frac{\int f(a) + \int f(b)}{2} \tag{3.2}$$

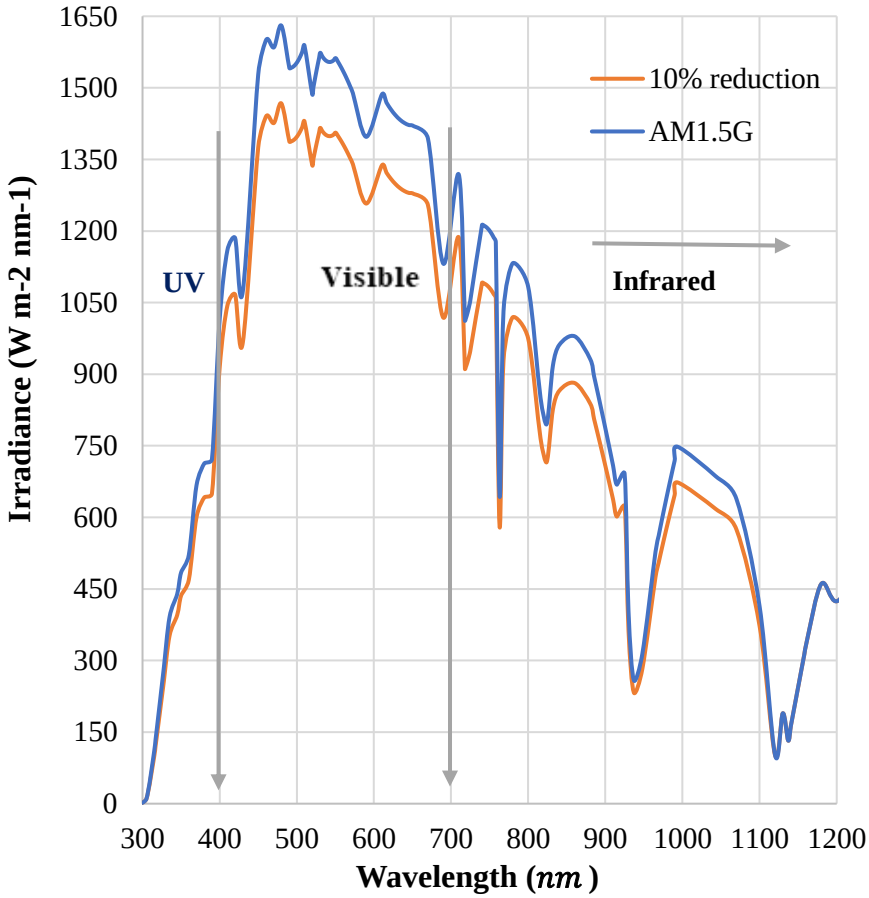


Figure 3.1 Simulation of the standard solar spectrum AM1.5G on earth, and standard solar spectrum with a 10% reduction.

3.2.2 Short Current Density, J_{SC}

A solar cell is a semiconductor diode with p-type and n-type doped regions that generate electricity from the absorption of light [5, 203, 204]. Depending on the type of semiconductor used, the properties of light reflection and light absorption vary, and they depend on many factors summarised in Eq. (3.3), and Eq. (3.4) [5]. Indeed, these factors determine the amount of generated photocurrent by the semiconductor and, hence the amount of energy produced [5].

Typically, in a solar cell, the p-type material is identified as the base and the n-type material is called the emitter, and the short-circuit current densities of each are calculated using Eq. (3.3) and Eq. (3.4) [5] below:

$$J_{scE}(\lambda) = \frac{q\alpha\phi_0(1-R)L_p}{(\alpha L_p)^2 - 1}\left[-\alpha L_p \mathrm{e}^{-\alpha w_e} + \frac{S_e\frac{L_p}{D_p} + \alpha L_p - \mathrm{e}^{-\alpha W_e}\left(S_e\frac{L_p}{D_p}Ch\frac{W_e}{L_p} + Sh\frac{W_e}{L_p}\right)}{Ch\frac{W_e}{L_p} + S_e\frac{L_p}{D_p}Sh\frac{W_e}{L_p}}\right] \tag{3.3}$$

$$J_{scB}(\lambda) = \frac{q\alpha\phi_0^{'}(1-R)L_n}{(\alpha L_n)^2 - 1}\left[-\alpha L_n - \frac{S_b\frac{L_n}{D_n}\left(Ch\frac{W_b}{L_n} - \mathrm{e}^{-\alpha W_b}\right) + Sh\frac{W_b}{L_n} + \alpha L_n \mathrm{e}^{-\alpha W_b}}{Ch\frac{W_b}{L_n} + S_b\frac{L_n}{D_n}Sh\frac{W_b}{L_n}}\right] \tag{3.4}$$

Where $J_{scE}(\lambda)$ is the spectral short-circuit current density at the emitter and $J_{scB}(\lambda)$ is the spectral short-circuit current density at the base, both measured in A $\mathrm{cm}^{-2}\,\mathrm{nm}^{-1}$. W_b and W_e are the thickness of the base and the emitter respectively, both measured in centimetres. R is the reflection coefficient, while α is the absorption coefficient measured in cm^{-1}. ϕ_0 and $\phi_0^{'}$ are the photon spectral flux at the emitter surface and the base-emitter respectively and have units of photons $\mathrm{cm}^{-2}\mu\mathrm{m}^{-1}\,\mathrm{s}^{-1}$. L_n and L_p are the length of electron and the hole diffusion at the emitter and base layers and both are measured in centimetres. D_n and D_p are the constant diffusion for the base and the emitter respectively, both measured in $\mathrm{cm}^2\,\mathrm{s}^{-1}$. Both S_e and S_b represent the recombination velocity at both sides of the emitter and base. They are also measured in $\mathrm{cm}^2\,\mathrm{s}^{-1}$.

In the simulation, the SPICE model was created based on the physical properties of silicon. PSpice version 17.2-2016 and LtSpice version XVII 17.0.0.11, (Analog Devices, USA) were used to run the simulations. To verify the SPICE model for silicon, PC1D software was also used. PC1D is a program developed and supported by the University of New South Wales in Australia that numerically determines the photo-response of a silicon solar cell [205]. When the absorption and reflection properties of silicon are calculated, they have then gathered along with the solar spectrum in a SPICE Piecewise Linear source to accurately simulate the spectral short-circuit current density.

Once light strikes a silicon solar cell, it generates photocurrents at both sides of the diode emitter and base which, when added, determine the total short-circuit current density of the cell. Consequently, the total spectral short-circuit current density is the sum of spectral short-circuit current densities at the emitter and base sides as seen in Eq. (3.5) [5].

$$J_{sc\lambda} = J_{scE\lambda} + J_{scB\lambda} \tag{3.5}$$

To find the total short-circuit current density, the sum of spectral short-circuit current densities must be integrated throughout all wavelengths as described in Eq. (3.6) [5]:

$$J_{sc} = \int_0^\infty J_{sc\lambda}\,\mathrm{d}\lambda = \int_0^\infty (J_{scE\lambda} + J_{scB\lambda})\,\mathrm{d}\lambda \tag{3.6}$$

3.2.3 Current-Voltage (I-V) Characteristic of a Solar Cell

By modelling the current density that is generated, this can be then inserted in a PSpice model as a voltage-controlled current source (G-device) modified by the incident solar irradiance:

$$G_{irrad} = \frac{J_{sc}A}{1000}.G \tag{3.7}$$

Where G is the incident irradiance in Wm^{-2}, and A is the solar cell area in cm^2. The equation uses the standard test condition for PV cells (STC), (AM1.5G spectrum, temperature at $25^{O}C$, and irradiance at 1000 Wm^{-2}).

However, to make a realistic model, all other parameters of the solar cell are considered. This is attained by using a PSpice sub-circuit to break the solar cell's equivalent circuit into three nodes; the first two nodes are the input nodes that consider the short-circuit current density, the dark current density (J_0), the recombination dark current density (J_{02}), irradiance (G), shunt resistance, and series resistance while the third node is the reference node. The irradiance represents the source that contains the two dark current densities (I_0), and (I_{02}) subtracted from the photo-generated current (I_L) as seen in Eq. (3.8) [5]:

$$I = I_L - I_0\left(e^{\frac{v+IR_s}{nV_T}} - 1\right) - I_{02}\left(e^{\frac{V+IR_s}{2V_T}} - 1\right) - \frac{V + IR_s}{R_{sh}} \tag{3.8}$$

Where V_T is the thermal voltage measured in volts.

To sum up, the model considers all solar cell parameters and encapsulant degradation can be simulated by decreasing the short-circuit current density proportional to the reduction in the optical absorption caused by the encapsulant degradation.

3.3 Simulation of EVA Degradation

In SPICE, scenarios of EVA degradation can be simulated by reducing or blocking some irradiance's wavelength as shown in Figures 3.2 and 3.3. These figures are two examples of the standard spectrum with blocking some of the wavelength range.

As can be seen in Figure 3.2, the visible wavelength ranges from 0.520 µm to 0.590 µm have been partially or entirely blocked. It is found that blocking of 0.010 µm resulted in 30 Wm^{-2} loss in irradiance, a 0.03% loss of power, whereas blocking 0.080 µm of wavelengths caused a 10% power loss. The effect of power losses on *I-V* curves can be simulated following the steps

described in Section 3.2. The power loss in Figure 3.2 can be calculated from Eq. (3.2).

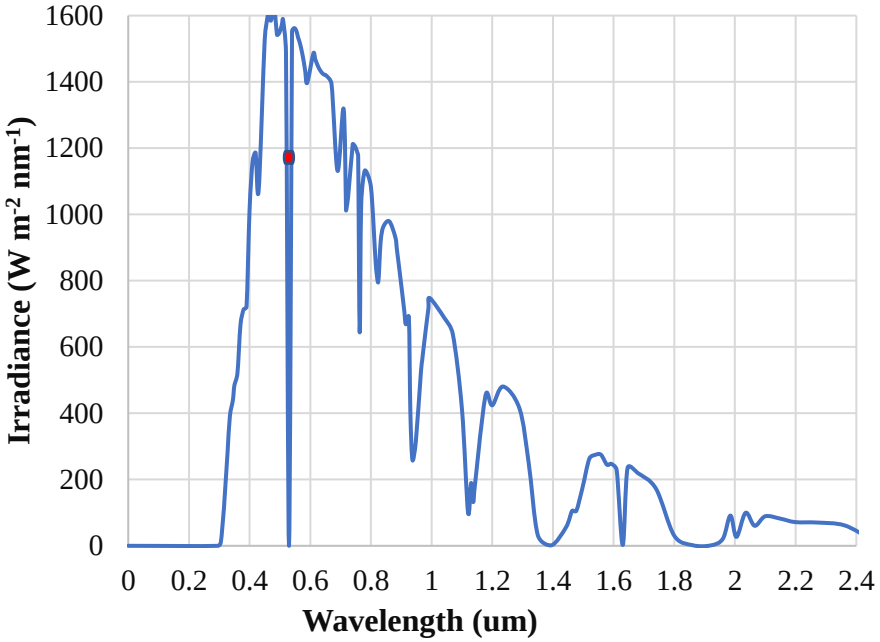


Figure 3.2 Standard solar spectrum with an obstructive wavelength from 0.523 µm to 0.530 µm.

$$\int_{0.523}^{0.530} 1000 d\lambda = 0.007 x 1000$$

As a result, 7 Wm^{-2} from irradiance was not absorbed and lost.

In Figure 3.3 scenario, the wavelengths from 0.523 µm to 0.603 µm were blocked. As a result, 80 Wm^{-2} of irradiance was not transmitted.

These two figures are presented as an example of the technique used to simulate the EVA degradation. Next, this section demonstrates the steps followed to simulate the EVA degradation following the results obtained experimentally from Pern *et al.* [97].

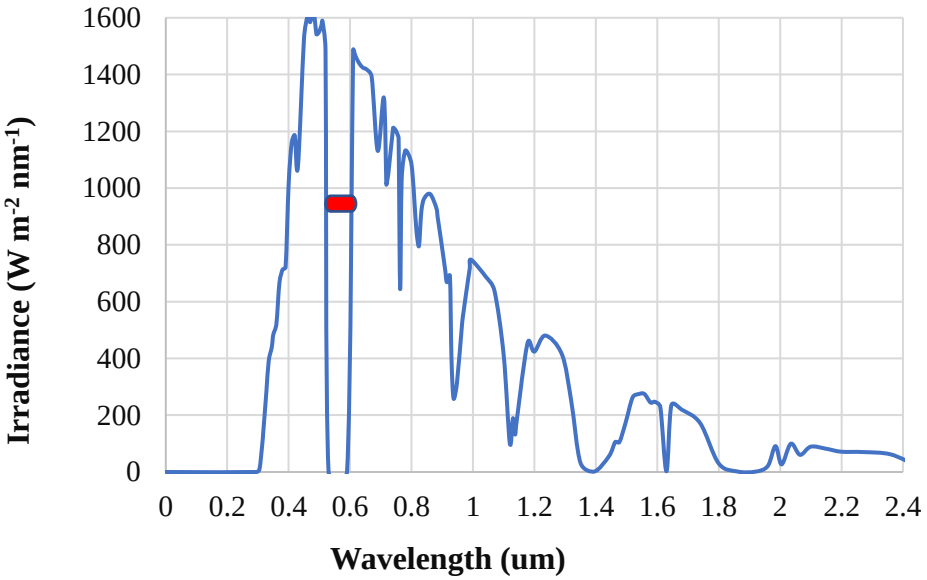


Figure 3.3 Standard solar spectrum with an obstructive wavelength from 0.533µm to 0.603 µm.

3.3.1 Transmittance Extraction from Experimental Data

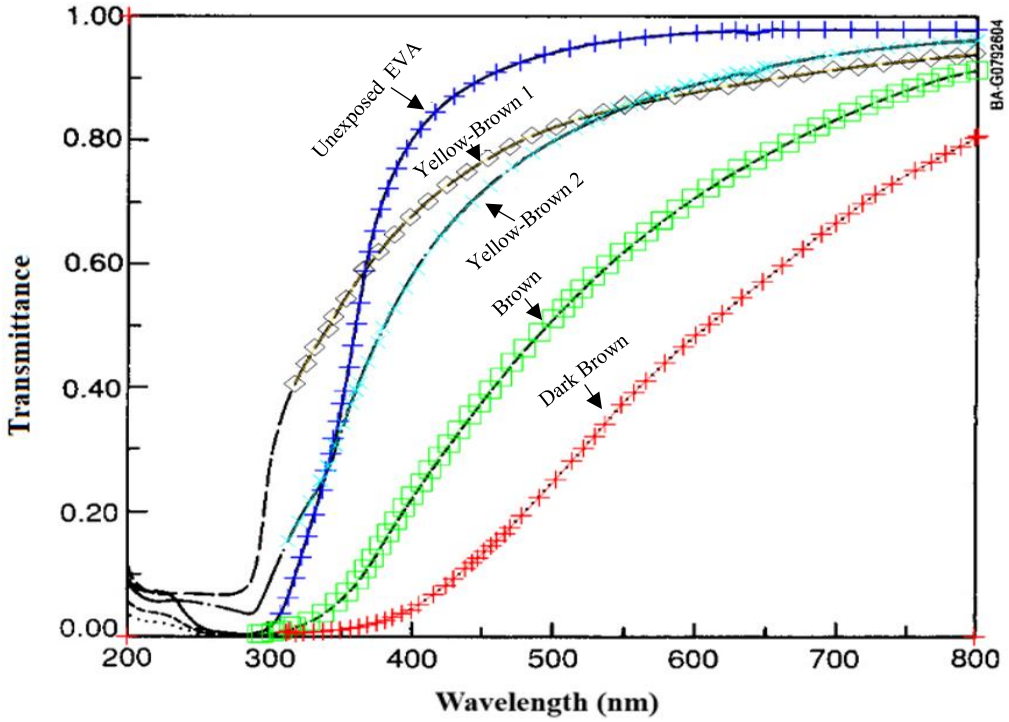


Figure 3.4 Transmittance for the five different encapsulants adapted from [97], with extracted transmittance data-points using Engauge Digitizer. Note: extraction below 300 nm was not carried out as these wavelengths are not absorbed by the silicon solar cell.

The experimental data used in this simulation study was extracted in Figure 3.4 of Pern *et al.* [97]. In their figure, they displayed the transmittance for five degraded EVA encapsulants based on their colours. Samples 1, 4, and 5 were laminated in two glass plates and exposed to an RS4 sun lamp at 90^{o}C for 1600 hours. Samples 2 and 3 were taken from weathered PV modules. Extracting the data points of the five EVA encapsulants was completed using the Engauge Digitizer Software Program Version 10.11 as shown in Figure 3.4. After obtaining the transmittance for each EVA type, these were then multiplied by the solar spectrum to obtain the modified received spectrum, and hence the expected short-circuit current density for each, as explained in Section 3.2.2.

However, this experimental data extends only as far as 800 nm with no information about the effective change in transmittance from 800 nm to 1100 nm. King *et al.* [60] conducted another study where the variation in transmittance between 800 nm and 1100 nm appeared less than 1% and thus transmittance changes over this wavelength range are considered negligible in this study. Taking into consideration Cases 4 and 5 in Figure 3.4, representing a worst-case change in transmittance of up to 12% over this wavelength range would result in an output current density increase from 17.98 mA cm^{-2} to 18.4 mA cm^{-2}, representing an error of 2.8%, which is sufficiently small that it is ignored in this study.

In addition, this model considers only a uniform reduction in transmittance across the cell. Further consideration should be given to situations where the discolouration is not uniform, for example, due to photobleaching. This is beyond the scope of the current model.

3.3.2 Simulation of Solar Spectrum for the Five Encapsulant

After obtaining transmission spectra for the five degradation scenarios of EVA, these were multiplied by the AM1.5G solar spectrum before being used in the simulation. The transmitted solar spectra are shown in Figure 3.5

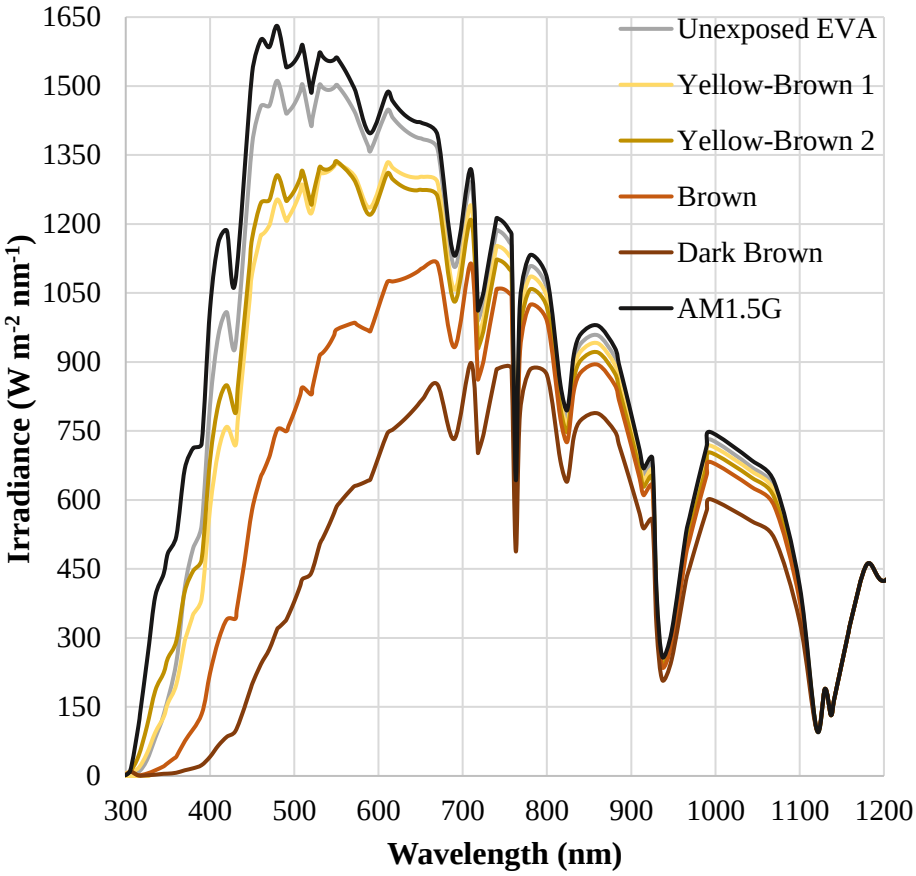


Figure 3.5: Six simulated solar spectra demonstrating the degradation of EVA encapsulant expected from Pern et al. [97].

3.3.3 Simulation of the Short-Circuit Current Densities

Using the transmitted solar spectra, the short-circuit current densities for the five degraded encapsulants are calculated. The J_{sc} is found from the wavelength integral of the spectral short current density. Simulating the $J_{sc\lambda}$ based on the photon wavelength is easily achieved using SPICE, as seen in Figure 3.6. As a result of the $J_{sc\lambda}$ simulations, it is observed from Table 3-1 that the value of J_{sc} for the two yellow-brown encapsulants differs only slightly. This is shown in Figure 3.6, where the $J_{sc\lambda}$ curves for these two cases are overlapping. This shows that even if the transmittance spectra for yellow-brown encapsulants differ, they end up generating nearly the same short-circuit current density.

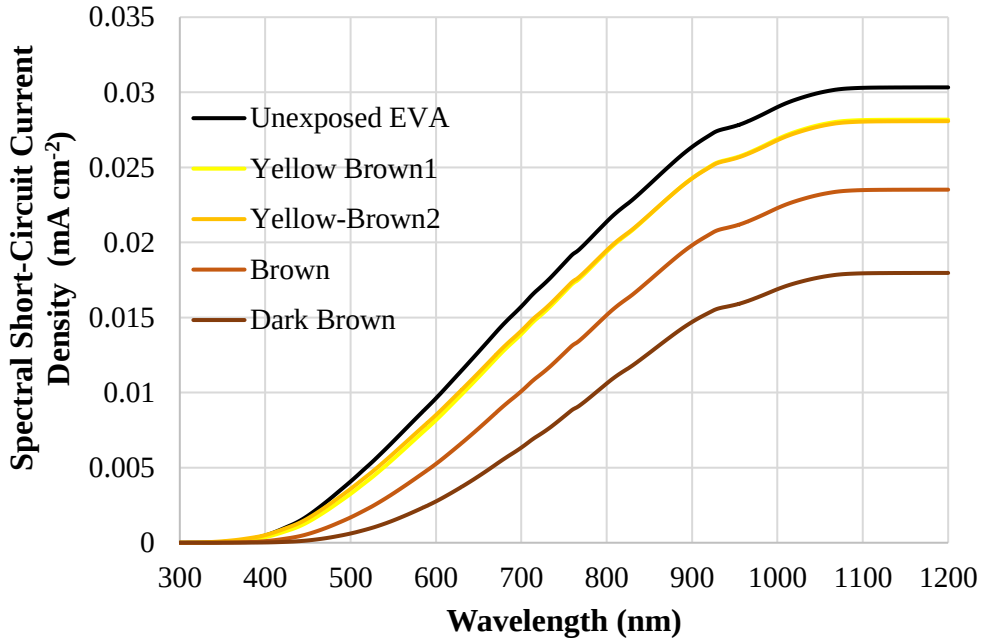


Figure 3.6: Simulation of the spectral short-circuit current density for the unexposed and four degraded encapsulant scenarios.

3.3.4 Simulation of the I-V Curves for the Five Degraded Encapsulant Scenarios

After finding the value of short-circuit current density for each degraded encapsulant in a PV solar cell, it is now possible to simulate the *I-V* curves by inserting these values into the SPICE code as explained in Section 3.3.3.

Table 3-1 Values of the short-circuit current density for the five encapsulant scenarios.

Encapsulant Colour	**J_{sc} (mA cm ^{2})**
Unexposed Encapsulant	30.34
Yellow-Brown-1 Encapsulant	28.09
Yellow-Brown-2 Encapsulant	28.2
Brown Encapsulant	23.53
Dark Brown Encapsulant	17.98

The code considers STC for photovoltaic modules by specifying the irradiance to be 1000 Wm^{-2}. It includes the calculated parameters for silicon properties, and the solar cell's parameters are benignly inserted including the J_{sc}, R_s, R_{sh}, J_0, and J_{02} values. Figure 3.7 shows the generated *I-V* curves for each encapsulant degradation scenario.

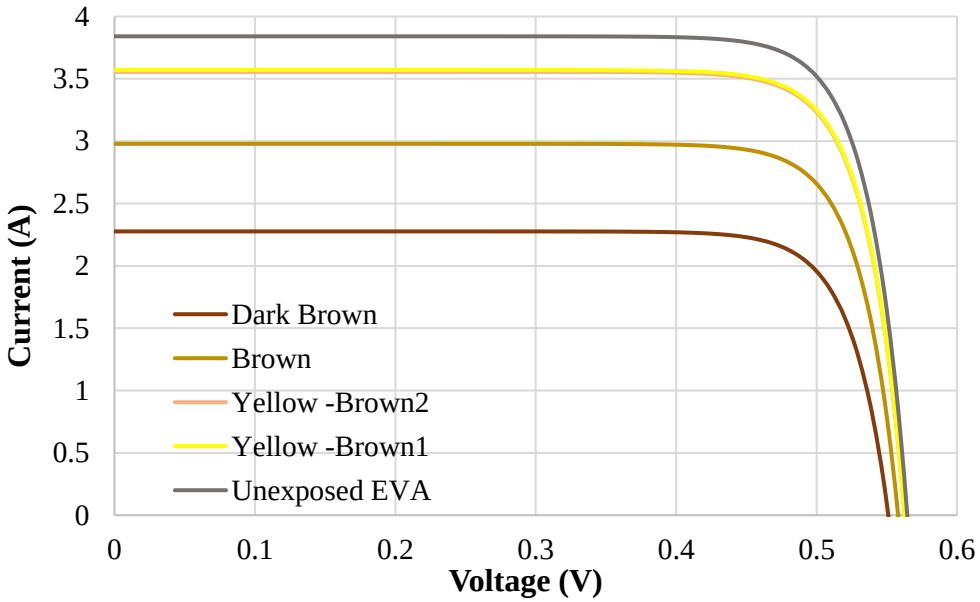


Figure 3.7: Simulation of the I-V curves for the five encapsulant scenarios.

Once the *I-V* curves are generated, other values of short-circuit current, open-circuit voltage, and maximum-power output, can be extracted and compared. It is worth mentioning that Pern *et al.* [97], had attached the discoloured encapsulants onto reference PV solar cells to compare their electrical performance.

However, it was not claimed or clarified in their study whether they attached the same encapsulants used to obtain the transmittance measurements in their Figure. Even without this clarification, the SPICE simulation here can still be compared to their results because they stated the difference in maximum-power output percentage between clear and coloured EVA.

3.4 Results and Discussion

This section compares the generated parameters obtained from the simulation of five EVA degradation scenarios, proceeding with the mathematical analogy to explore the possibility of developing a model that can detect the onset of optical degradation represented by EVA discolouration.

3.4.1 Correlations Between EVA Transmittance and Electrical Parameters

Table 3-2 Value of Isc, Voc, and P_{max} for the five encapsulant degradation scenarios along with a further 5%, and 10% reduction in the dark encapsulant transmittance, and their ratio relative to the unexposed EVA values.

Encapsulant Colour	**I_{sc} (A)**	**Ratio to I_{sc}**	**G (Wm^{-2})**	**Ratio to G**	**V_{OC} (mV)**	**Ratio to V_{OC}**	**P_{max} (W)**	**Ratio to P_{max}**
Unexposed Encapsulant	3.84	1.00	942	1	565	1	1.78	1
Yellow-Brown 1	3.57	0.930	885	0.939	563	0.996	1.646	0.924
Yellow-Brown 2	3.55	0.924	879	0.934	562	0.995	1.628	0.914
Brown	2.97	0.776	746	0.792	558	0.988	1.363	0.765
Dark Brown	2.27	0.593	588	0.624	550	0.973	1.022	0.574
Dark Brown -5%	2.05	0.532	563	0.598	549.7	0.973	0.98	0.55
Dark Brown -10%	1.94	0.503	544	0.577	546.7	0.967	0.865	0.486

For the purposes of the simulation, the solar cell surface area was taken as 126.6 cm^2 and J_{sc} was 0.0323 A cm^{-2}. The simulation did not consider the cell parameters used by Pern *et al.* [97] but only considered the optical transmission

figure presented. It is the relative change in P_{max} from the Pern study that matches those presented here in this study.

From Table 3-2, it is shown that P_{max} is reduced by more than 50% if the spectrum of the dark brown EVA is further reduced by 10%. The addition of simulated data points for reduced transmittance of 5% and 10% from dark brown have been included to take the cell to a reduction of P_{max} by more than 50% and thereby to a point of failure. The reduction in the absorbed solar spectrum is directly proportional to the reduction in the EVA's transmittance. The short-circuit current, open-circuit voltage, maximum power output, and fill factor were compared as a function of transmitted solar irradiance as shown in Figure 3.8.

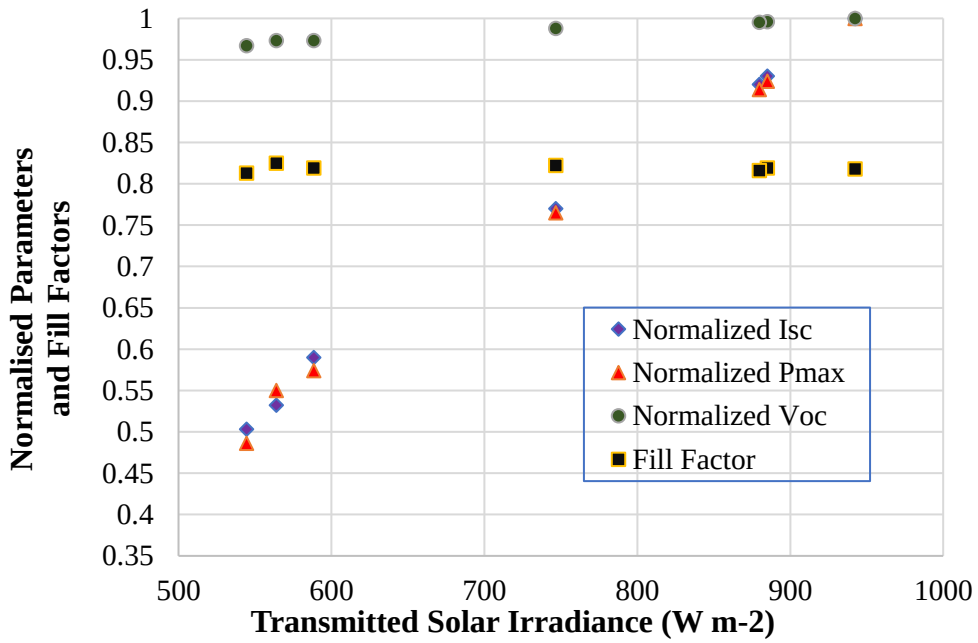


Figure 3.8: Relationships between received solar irradiance via encapsulant degradation scenarios and electrical parameters of the solar cell. The short-circuit current, maximum power output, and open-circuit voltage were normalized relative to their value in the unexposed EVA degradation scenarios and electrical parameters of the solar cell.

These findings, where I_{sc} changes significantly, and where V_{OC} is only slightly affected, agree, unsurprisingly, with the findings in the experimental results reported by Pern *et al.* [97]. However, the simulation does allow

quantification of the rate of reduction in transmitted light with increased EVA degradation and it is this the slope that can be used to determine early onset degradation, as will be shown later.

3.4.2 Simulation Verification Using the PC1D PV Modelling Software

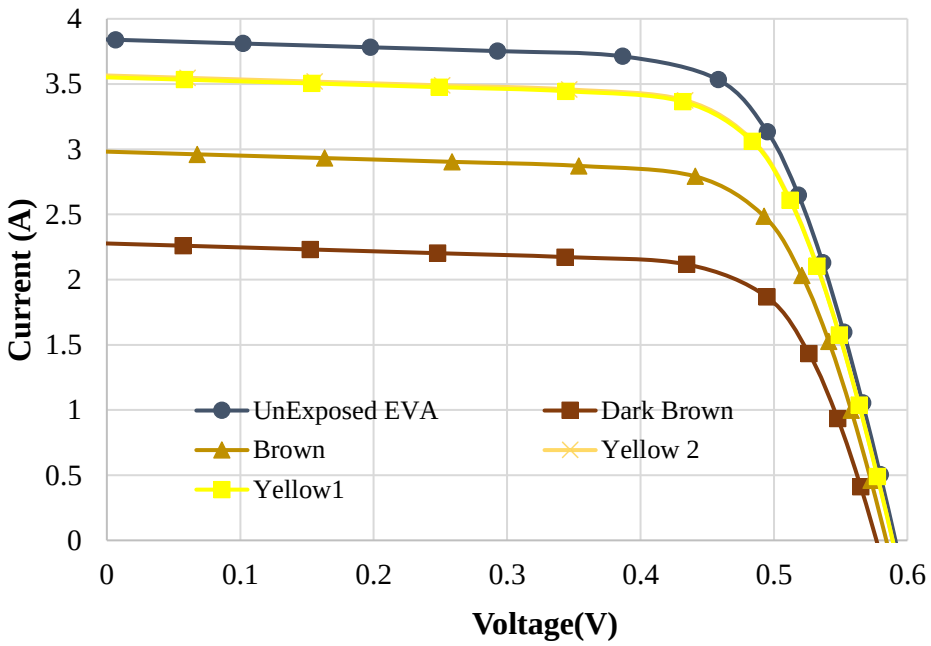


Figure 3.9: I-V curves generated from a solar cell with five encapsulant scenarios simulated in the PC1D modelling program.

For validation purposes, the encapsulant degradation scenarios were also simulated using the PC1D simulator. Since it was found from the previous section that the variation in short-circuit current is the strongest measurable indicator of the EVA degradation, the comparison is based on the generated I_{sc} values from both the SPICE and the PC1D models. In PC1D, the solar cell used in the simulation was a default cell named PVCEll.PERN. The solar spectra that were simulated for EVA degradation scenarios in SPICE were also used to run the simulations in PC1D.

Table 3-3 Comparison between the generated Isc from PC1D and SPICE for the five EVA degradation scenarios.

Encapsulant Degradation Scenario	I_{sc} (A) PC1D	I_{sc} (A) SPICE
Unexposed EVA	3.84	3.84
Yellow-brown 1	3.57	3.57
Yellow -Brown 2	3.55	3.55
Brown	2.97	2.98
Dark Brown	2.27	2.28

It is not mentioned in the PC1D's manual book that using the standard spectrum is restricted only in the file given by PC1D. Therefore, the solar spectra that were simulated and reduced in the SPICE modelling program used for the five encapsulant degradation scenarios, were also used to generate the *I-V* curves of the five encapsulant scenarios but in PC1D. The simulation results from PC1D can be found in Table 3-3.

As can be seen, the generated short-circuit current derived from PC1D corresponds favourably to the values obtained using SPICE.

3.4.3 Modelling the onset of EVA degradation

Any reduction in the absorbed solar irradiance results in a reduction in the short-circuit current. Where there is a spectrally neutral reduction in solar irradiance, due for example to seasonal variations in intensity, there is a reliably determined value for short-circuit current. In cases where a short-circuit current value is measurably lower than expected from independently measured solar irradiance, the EVA degradation process may have begun.

It is noted that I_{sc} is also reduced via other factors such as dust accumulation, corrosion, and delamination. Hence, a single reduction of short-circuit current at a particular solar irradiance cannot be used as a decisive technique for the detection of EVA degradation. In Figure 3.10, eight data

points showing different stages of EVA degradation are additionally plotted, demonstrating a linear relationship between the short-circuit current and transmitted solar irradiance reduced by EVA degradation. This linear relationship provides, through measurement of the slope, an accurate technique to determine the onset of EVA degradation in a way that a single measurement of short-circuit current cannot.

The eight more points of encapsulant degradation were not added arbitrarily. They followed the same degradation trend of the given experimental data from Pern *et al.* [97]. A difficulty, in this case, is that the solar spectrum was not reduced uniformly, i.e., the energy produced at some wavelength point was reduced by 10% others reduced by 30%.

To overcome this obstacle, the reduced percentage for each wavelength point was calculated independently for accurate estimation. The points below illustrate the estimation method:

1) The reduced percentage for each wavelength-point of the solar spectrum due to EVA discolouration was reduced or increased in accordance with Table 3-4.

2) The reduced or the increased percentage for each wavelength point was multiplied by the standard solar spectrum AM1.5G.

3) After obtaining the reduced or increased values for all the wavelength points, they were then inserted in the SPICE simulation program to generate the new solar spectrum curve.

4) The solar spectrum for each new data point was integrated to calculate the solar irradiance. It was also used to generate the short-circuit current density which in turn was used to generate the *I-V* curve. This point and point 4, are a redoing of the steps explained in Section 3.2, but for the new solar spectra subjected to encapsulant degradations.

5) The new eight-date points of the encapsulant degradation that were added are listed below:

   A. 3% and 6% less degradation points of the yellow-brown1 (Y-B1) encapsulant.

   B. 10% and 15% more degradation points of the yellow-brown2 (Y-B2) encapsulant

   C. 8% and 16% more degradation points of the brown encapsulant.

   D. 5%, and 10% more degradation points of the dark brown (DB) encapsulant which were added earlier in Table 3-2.

In deployed PV plants, instruments that measure electrical parameters and solar irradiance are regularly installed to monitor the system [206-208]. The measured data is collected and stored as part of the Data Acquisition System. This can be compared to a linear model relating solar irradiance to measured and expected short-circuit current. The slope of the linear fit can be used as a control model to observe the EVA condition.

Routinely, new data is collected for short-circuit current at the same irradiance level, and if the new linear fit shows an increased slope over that expected for normal irradiance changes, it can be determined that the EVA degradation process has begun.

As can be seen in Figure 3.10 normal (uniform) reductions in solar irradiance when correlated with the generated I_{sc} have a different slope to the one that demonstrates EVA degradation. Based on this deviation from the expected slope the early onset of EVA degradation can be predicted even before yellowing is observable.

Table 3-4 Short-circuit current relative to the unexposed encapsulant.

Encapsulant Colour	**Solar Irradiance (W m^{-2})**	**Received solar irradiance relative to the unexposed EVA**	**I_{sc} (A)**	**Generated I_{sc} relative to the unexposed EVA**
Unexposed EVA	942.3	1	3.85	1
Y-B1 +6%	926.6	0.983	3.77	0.979
Y-B1 +3%	905.9	0.961	3.66	0.95
Y-B1	885.1	0.939	3.57	0.927
Y-B2	879.8	0.934	3.55	0.922
Y-B2 -10%	811.1	0.861	3.21	0.833
Y-B2 -15%	777.9	0.826	3.03	0.787
Brown	746.6	0.792	2.97	0.771
Brown -8%	702.3	0.745	2.74	0.712
Brown -16%	657.9	0.698	2.49	0.647
Dark Brown (DB)	588.4	0.624	2.27	0.59
DB -5%	563.9	0.598	2.05	0.532
DB - 10%	544.4	0.577	1.94	0.503

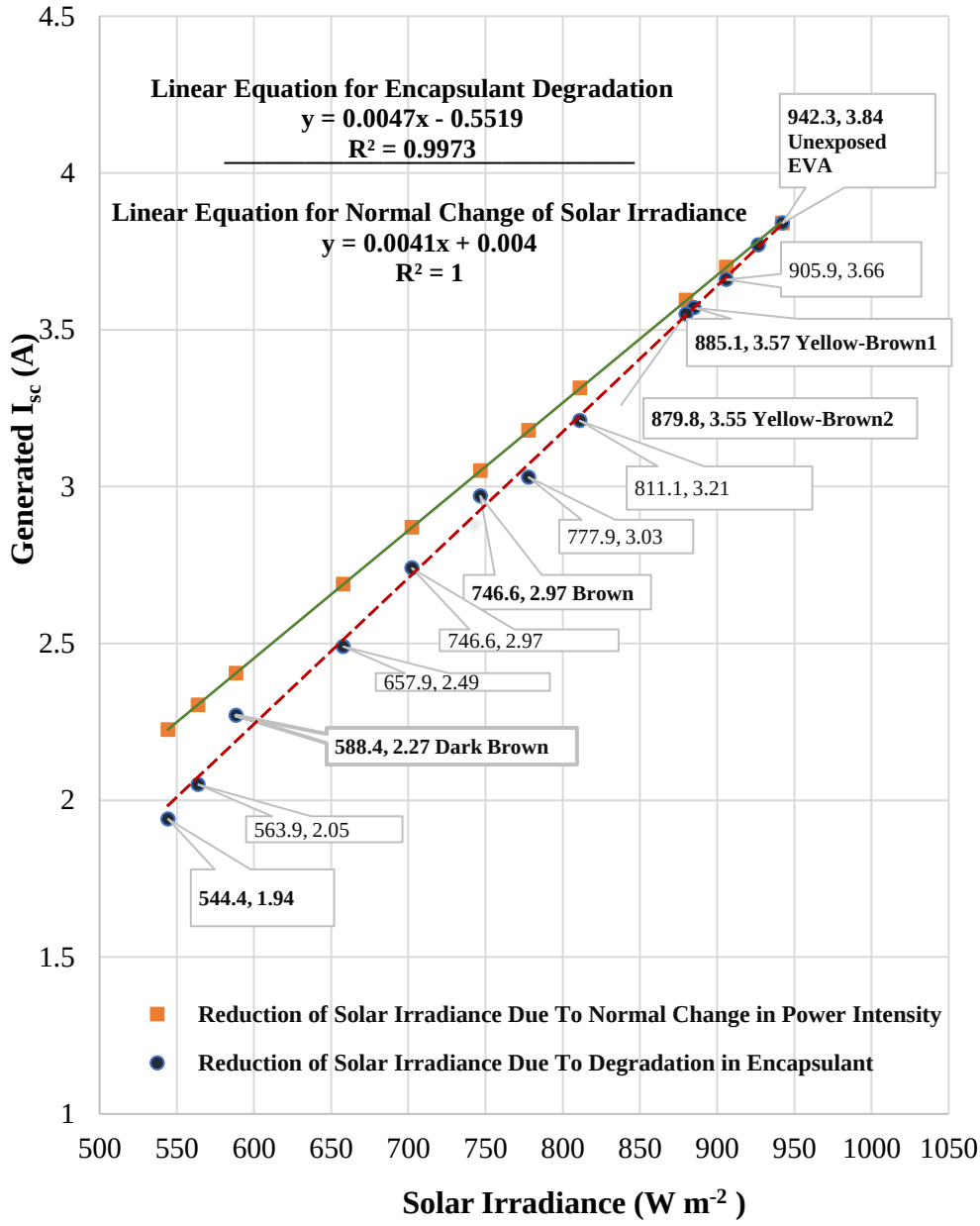


Figure 3.10 Linear fit models between the solar irradiance and the generated short-circuit current for EVA degradation Vs normal change of solar irradiance started from the same irradiance EVA received when it was clear. When the P_{max} falls below 50% of the original power the cell is considered to have failed.

It could be argued that due to EVA discolouration series resistance will be increased in the PV module and as a result, the short-circuit current will be affected. Consequently, the proposed linear fit model is neither accurate nor effective. For example, Sinha *et al.* [175] found that the series resistance

increased by roughly 80% in discoloured PV module that was deployed for 20 years.

The increase in series resistance of PV module degraded by EVA discolouration is due to corrosion of the metallic bond caused by the release of EVA's acetic acid [75, 175]. Corrosion causes an increase in series resistance, but this will not be reflected in changes to the I_{SC} until the series resistance has been increased by a factor of 10 [188, 209]. In a study by Dechthummarong *et al.* [98], corrosion was not detected in light yellow discolouration but was detected from dark yellow to dark brown discolouration. It has been demonstrated elsewhere [190] that the mean increase in series resistance due to corrosion is a factor of 8.5. This has also been simulated in SPICE.

Thus, this expected change in series resistance caused by corrosion will not significantly affect the model presented in this thesis.

3.5 Conclusion

Most commercial solar cell manufacturers continue to use EVA as an encapsulant, despite its vulnerability to UV degradation over the operating life of the cells, resulting in reduced power output and even complete failure of modules. The literature review in Chapter 2 showed that most of the studies report results of lab experiments via exposing the EVA encapsulant to different stress factors. Some studies had found that EVA degradation starts before the colour alters to yellow and becomes more severe once the colour changes to brown. This chapter focused on the simulation of such scenarios based on encapsulant discolouration, and hence optical transmission.

Due to a lack of sufficient studies that investigate the *I-V* parameters due to EVA discolouration, this chapter focuses on investigating these parameters. Each encapsulant colour generated a different *I-V* curve when attached to a solar cell and delivered a different P_{max}. Table 3-5 compares the approach used

by widely-cited EVA discolouration articles and the approach followed in this chapter.

Table 3-5 The approach used by widely-cited EVA discolouration articles and the approach followed in this chapter.

Scientific Articles versus Existing Work	Approach Used
Pern *et al.* [97].	Investigating the effect of five discolouration scenarios of EVA on solar cell efficiency, the reduction in $P_{max,}$ I_{SC} and V_{OC} was in agreement with the findings in this chapter. The fill factor was not evaluated.
Pern [210].	Investigating the effect of discolouration from filed EVA as well as lab experiments. Parameters of the cell with degraded EVA scenarios ($P_{max,}$ $I_{SC,}$ fill factor and V_{OC}) were not evaluated except for solar cell efficiency.
Pern [211].	Investigating factors that accelerate EVA discolouration. Factors were summarised into two categories: chemical and physical. Neither EVA discolouration by chemical factors nor discolouration by physical factors' effects on solar cell parameters ($P_{max,}$ $I_{SC,}$ fill factor and V_{OC}) were evaluated.
Existing Work	Simulation of EVA discolouration using SPICE software program. $P_{max,}$ $I_{SC,}$ fill factor and V_{OC} parameters due to EVA discolouration were quantified. Results were employed to develop a novel model that detects the early onset of EVA discolouration.

A novel method has been proposed whereby the slope of the linear relationship between the degree of EVA degradation and the corresponding short-circuit current is compared to the slope expected in the case of uniformly reduced optical transmission. The application of this model requires the use of monitoring devices to determine the local solar irradiance thereby differentiating between generated I_{sc} and expected I_{sc}. However, the model accuracy may reduce in the case of shading, a PV failure classified in the electrical category [50]. Hence, shading and most electrical failures are linked with low shunt resistance. In this regard, the following two chapters investigate the effect of shunt resistance in PV cells and modules.

4 Chapter 4 | Early Prediction of Shunt Resistance Degradation in PV Modules

In Chapter 2, the scientific literature presents many studies that evaluate shunt resistance at PV failure modes, mainly failures categorised in the electrical group such as shading. However, only a few studies employed shunt resistance to predict PV malfunction. Thus, this chapter investigates the effect of reduced shunt resistance on the *I-V* characteristics of a PV cell to identify degradation before it becomes hazardous. Five commercial polycrystalline solar cell samples were measured with artificially lowered shunt resistance. Reduction in shunt resistance is correlated with the cell's electrical parameters to predict degradation before it leads to catastrophic failures. Linear models have been developed relating reduction in shunt resistance to the solar cell's P_{max} and V_{OC}. As with the proposed model in Chapter 3, these relationships are suitable for implementation in online monitoring systems for operational PV modules as robust indicators and observers of shunt resistance degradation.

4.1 Introduction

A solar cell can be modelled as an ideal p-n junction diode with series resistance and shunt resistance. The solar cell performs more efficiently with large shunt resistance, ideally infinite, and low series resistance, ideally zero. Otherwise, a reduction in the shunt resistance over time can lead to cell and module degradation, resulting ultimately in module failure [130][147-151]. Chapter 2 showed that most PV failures, specifically classified in the electrical group by Tsanakas *et al.* [58], are associated with low shunt resistance e.g., [156-160]. This

is the first study, to the authors' best knowledge, which experimentally investigates the effects of decreased shunt resistance on cell operating parameters; short-circuit current, open-circuit voltage, maximum power output, and fill factor, using R_{sh} to indicate the early onset of critical PV degradation. We have identified a key threshold of shunt resistance, at which corrective action should be taken by photovoltaic system operators to avoid the development of catastrophic failures. A linear model has been developed which allows this degradation to be monitored in terms of key operational parameters. This can be applied to operational photovoltaic systems even under varying levels of solar irradiance in order to improve the reliability of operational solar photovoltaic systems.

In this chapter, the shunt resistance is modified using fourteen different resistor values on five separate samples of polycrystalline cells. Artificially lowering R_{sh} is one technique to help understand the solar cell's behaviour, allowing observation of the *I-V* characteristics as the critical degradation mechanism initiates. Experimental setup and procedure to reduce the shunt resistance and extract its value are described in Section 4.2. Section 4.3 quantifies any errors that possibly arise during the experiment to be taken into account. Section 4.4 describes the results of the shunt resistance's effect on the cells' *I-V* curve, helping develop linear models to predict the early onset of PV critical degradation.

4.2 Experimental Procedure

A Newport Solar Simulator Model No. Sol1A with a Xenon lamp was used to illuminate the solar cell surface consistent with the AM 1.5G irradiance. The Xenon lamp current was adjusted to set the irradiance at 1000 ± 45 W m^{-2}. A solar

cell housing was constructed to stabilise the solar cell inside the solar simulator. Figure 4.1 shows the designed solar cell housing, drawn using Autodesk Fusion 360 [212].

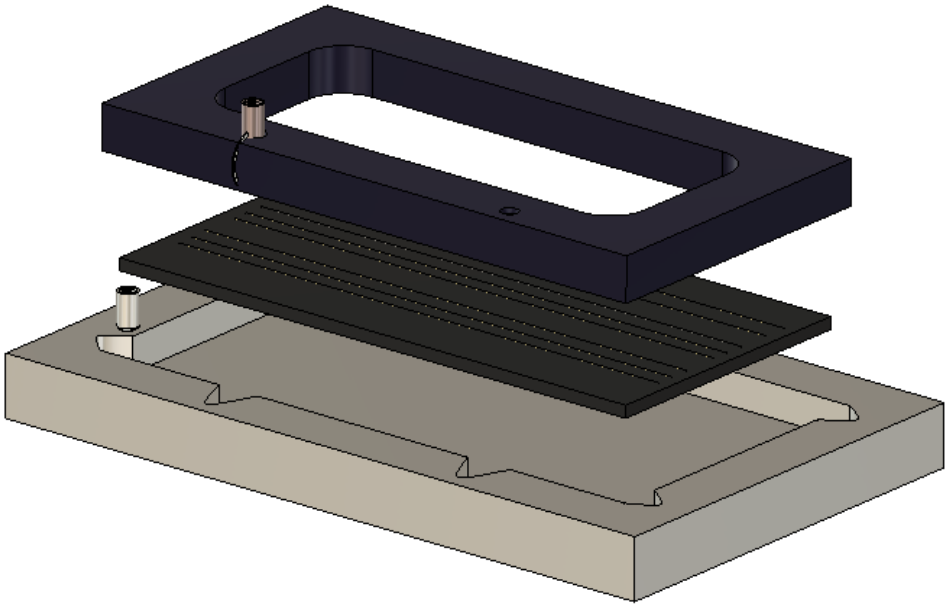


Figure 4.1 Solar cell housing designed using Autodesk Fusion 360

The measurements started at 0.0 V and ended at 0.6 V with a sequence reading of 0.01 V. The open-circuit voltage of the solar cell is determined when the current is at 0 A, (V_{oc},0), and the short-circuit current is determined when voltage is at 0 V, (0, I_{sc}). The other parameters of the solar cell, maximum voltage, and current, maximum power output, and fill factor, were calculated and extracted using Microsoft excel and Python Software Program-Spyder 4.2.5. Figure 4.2 shows the experiment setup using the Keithley source meter to take measurements of the solar

cell electrical parameters as well as some resistors that were added to the solar samples to decrease the shunt resistance.

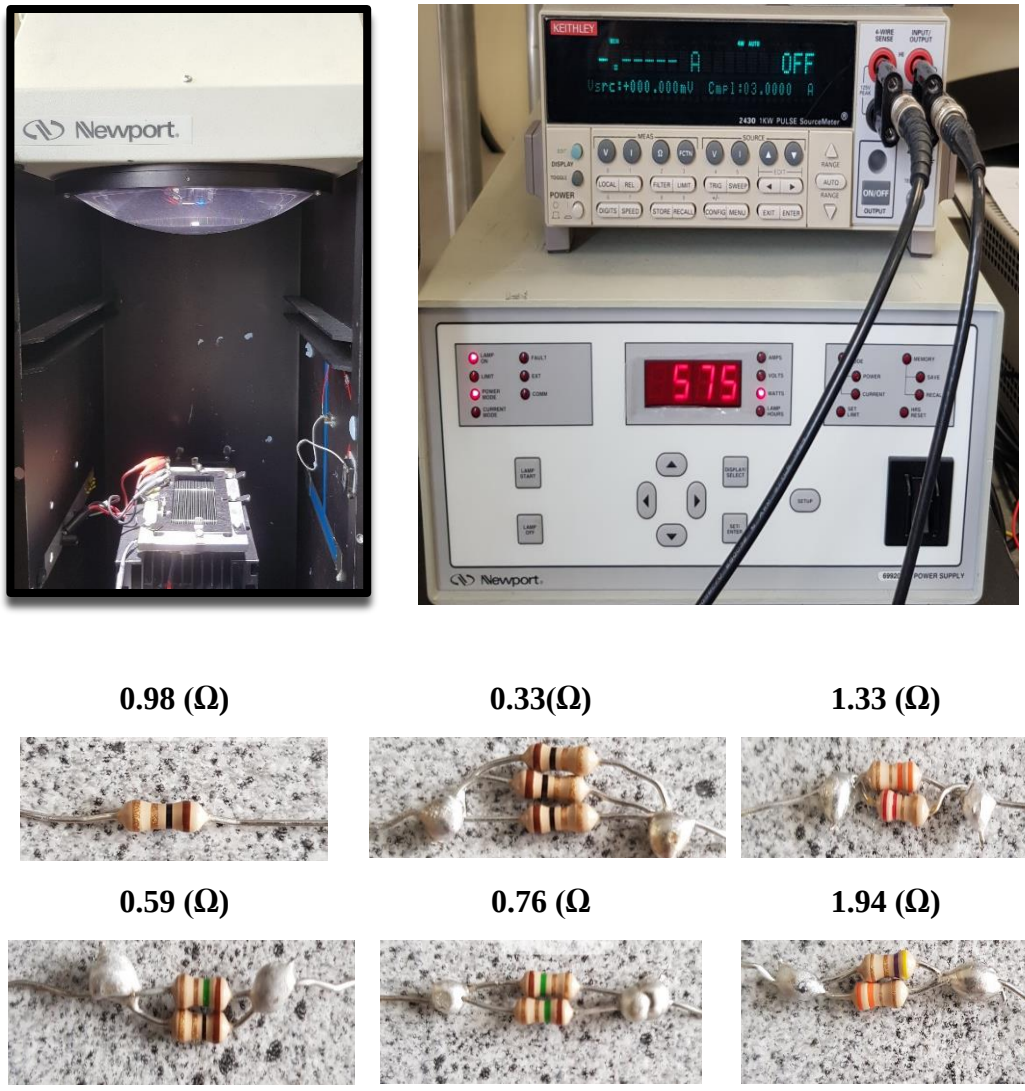


Figure 4.2 Newport Sol1A, solar simulator along with Keithley Source Meter used to take measurements of the electrical parameters of the solar cell samples and some resistors that were added in parallel to the shunt resistance.

Whenever the solar cell or resistor was changed, the resulting disturbance caused an average of 4.5% fluctuation in solar irradiance. The housing consists of two main components: a metal base and a black PVC lid that establishes the active cell area 12 cm in length and 5 cm in width, exposing 60 cm^2 of the solar cell's surface area to light. The metal base made electrical connection with the solar cell's P-type layer on the rear surface of the solar cell. A conductive bolt soldered to the front surface busbar on the cell allowed electrical contact with the n-type terminal on the front surface.

The shunt resistance value was extracted using the mathematical model provided by Chan *et al.* [213]. Despite the experiment followed a simple way, it was set in an optimum design to precisely reach robust results:

Firstly, measurements were conducted on five separate solar cells, each adjusted using the same set of resistor values to vary the shunt resistance of the cell and to ensure steady results across all solar cell samples. Thereby, discovering the nature of poly-crystalline cell with low shunt resistance.

Secondly, each measurement was made ten times and averaged for each resistor value to account for measurement errors.

Thirdly, after measuring and recording the output data of the five samples, measurements of Sample 2, Sample 3, and Sample 5 were repeated after had been saved for four weeks in the lab to verify that they produce the same results. This assists to determine the shunt resistance level that indicates the onset of critical degradation. The same procedure used in the first measurements had been followed in the second measurements, attaching fourteen resistors from 9.88Ω to 0.33Ω in

parallel to the shunt resistance, each resistor had been measured 10 times, and the mean values were calculated.

Fourthly, to investigate the effect of reducing shunt resistance on different solar cell surface areas, one additional plastic cover with window dimensions of 5.30 cm × 8.50 cm was used, making the exposing surface area to become 42.5 cm^2. This provided another verification that the obtained experiments' results were accurate.

Finally, irradiance and temperature fluctuations were investigated and taken into account.

4.2.1 Adding External Resistance in Parallel to the Shunt Resistance

The study is motivated by Ohm's law whereby adding resistors in parallel reduces the overall resistance. An external resistor was connected between the solar cell's positive and negative terminals and held stable via conductive clamps. The resulting equivalent circuit of the single diode model of the solar cell has the shunt resistance divided into two components, as illustrated in Figure 4.3, with the resultant shunt resistance calculated using Equation 4.1.

Resistors with values from 97 Ω down to 0.33 Ω were successively added to the 1st cell sample. The resistor values that showed a significant impact on the 1st cell's electrical characteristics were used for the other four samples.

Fourteen significant resistor values were identified, ranging from 9.88 ± 0.10 Ω to 0.33 ± 0.07 Ω. They were measured using a digital programmable multimeter (Thurlby Thandar Instruments (TTI), model No. 1705).

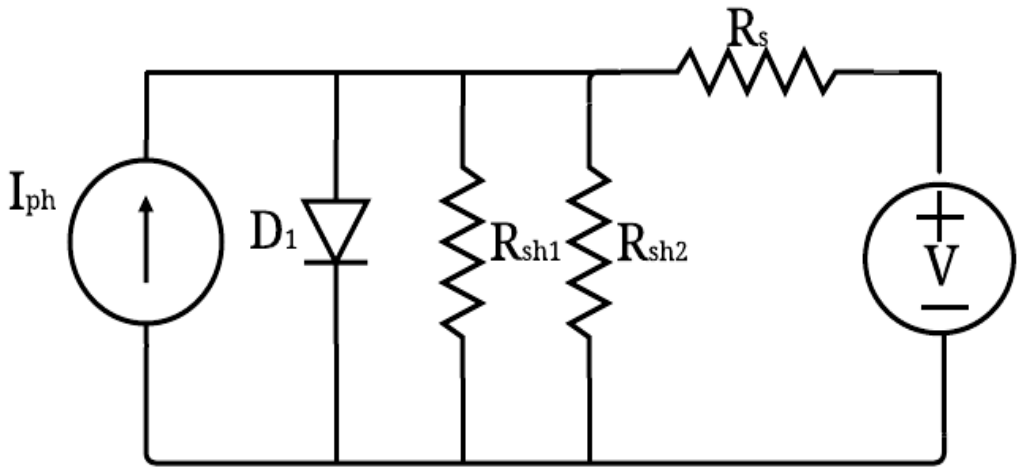


Figure 4.3 The equivalent circuit of the solar cell's single-diode model, modified by adding a resistance R_{sh2} in parallel with the cell's internal shunt resistance R_{sh1}.

$$R_{sh} = \frac{R_{sh1} \times R_{sh2}}{R_{sh1} + R_{sh2}} \quad (4.1)$$

The measurements were repeated using two other multimeters of the same type to statistically account for calibration errors. As the TTI uses a Two-Wire Resistance Measurement method, the measurement was repeated using the Four-Wire Resistance Measurement method using a Keithley Source Meter Model No. 2400 to eliminate errors due to the measurement wire resistance [214]. A constant difference of $0.10\,\Omega$ was observed between the two-wire and four-wire measurements and the two-wire resistor values were adjusted accordingly. Table 4-1 lists the resistors added parallel with the cells' internal shunt resistance samples.

Table 4-1 The resistors' mean values (MV) that were added to the solar cell's samples, with the resulting total shunt resistance.

Added Shunt Resistance R_{sh2} (Ω)	Total Shunt Resistance R_{sh} for Each Sample (Ω cm^2)				
	Sample 1	Sample 2	Sample 3	Sample 4	Sample 5
9.88 ±0.10	509.70	516.22	544.35	504.32	541.37
7.88 ±0.08	418.39	422.78	441.46	414.76	439.50
6.31 ±0.05	342.90	345.83	358.24	340.45	356.94
4.64 ±0.11	258.60	260.27	267.23	257.21	266.51
3.32 ±0.06	188.85	189.74	193.41	188.11	193.04
2.20 ±0.09	127.38	127.78	129.43	127.04	129.27
1.94 ±0.07	112.79	113.11	114.40	112.52	114.27
1.50 ±0.06	87.83	88.02	88.80	87.67	88.72
1.32 ±0.07	77.51	77.66	78.27	77.39	78.21
0.98 ±0.09	57.86	57.95	58.29	57.79	58.25
0.76 ±0.08	45.04	45.09	45.29	44.99	45.27
0.59 ±0.08	35.06	35.09	35.21	35.03	35.20
0.50 ±0.07	29.75	29.78	29.87	29.74	29.86
0.33±0.07	19.69	19.70	19.74	19.68	19.74

4.2.2 Extracting the Internal Shunt Resistance

Several methods were found in the literature to extract the R_{sh} from an illuminated *I-V* curve. The Chan *et al's.* [213] a mathematical model which was developed to identify the parameters of the solar cell's single diode model at illumination above 1 AM was followed. Due to its simplicity and accuracy, their approach has been widely cited and evaluated by many researchers, e.g., [215-217]. From this model, the shunt resistance is equal to the slope at the I_{SC} point identified as reciprocal of slope at short-circuit point (R_{sho}) and can be extracted by applying a linear least-squares fit near $I_{SC,}$ as seen in Eq. (4.2) [213].

$$R_{sh} = R_{sho} = -\left(\frac{dv}{dI}\right); \quad I = I_{sc} \tag{4.2}$$

It is worth mentioning that the externally added resistor primarily determines the overall R_{sh}. That is, any error in identifying the internal R_{sh} of the cells is rendered negligible by the externally added resistor. The internal shunt resistance of the cell samples was equal to 3636 Ω cm^2, 3996 Ω cm^2, 6660 Ω cm^2, 3379 Ω cm^2, and 6240 Ω cm^2 respectively, when calculated using Eq. (4.2).

4.3 Effect of Irradiance and Temperature Fluctuation

4.3.1 Effect of Irradiance Fluctuation on I-V Measurements

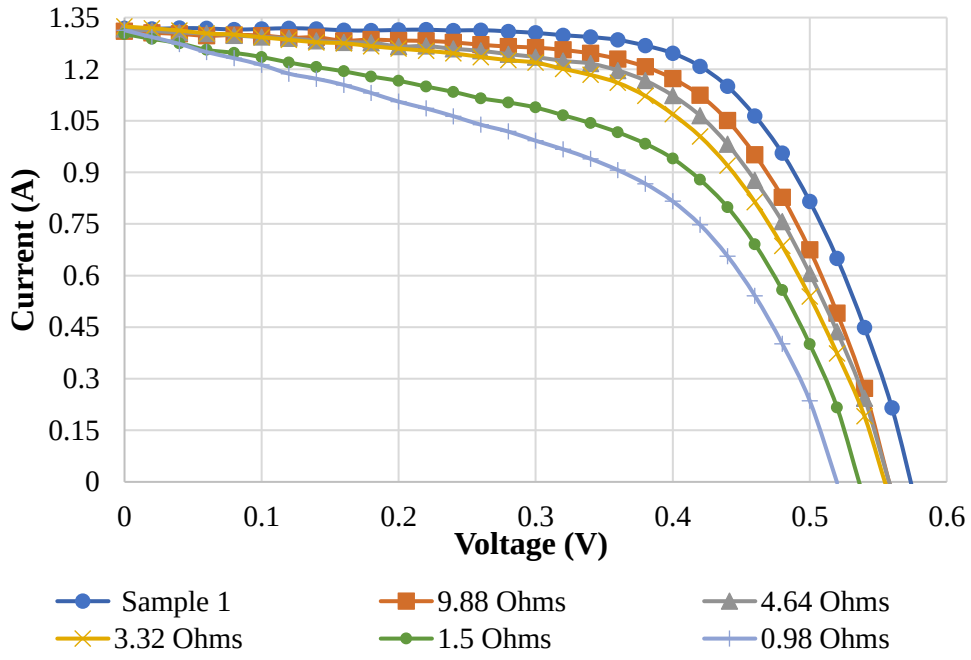


Figure 4.4 I-V curves obtained at different shunt resistance levels with 1-2% limited variations of solar irradiance.

Fluctuation in the lamp irradiance led to fluctuations in the output currents resulting in an average variation of 4.5% in I_{SC}. This also causes a variation in P_{max}. To investigate if the variation in I_{SC} was caused by low shunt resistance or due to irradiance fluctuation, the measurements of the 1st sample were repeated until the irradiance fluctuation was limited between 1% to 2%. The results showed that lowering the shunt resistance did not affect the I_{SC}. Figure 4.4 shows six *I-V* curves obtained at limited fluctuations of irradiance.

4.3.2 Effect of Temperature Rise on I-V Measurements

The room temperature fluctuated between 23°C and 26°C during the measurements. The cell temperature was also affected by the heat build-up of the solar simulator's Xenon lamp. To minimise these effects the ten measurements for each externally added resistor were completed in less than 240s, limiting the temperature rise to less than 3°C. Errors caused by this temperature rise were taken into account by measuring the 2nd sample with two different resistors in place for 300 seconds. The temperature increased gradually with time and caused I_{SC} to increase by 3.4% at most; hence, P_{max} was increased slightly by about 3.37%. In contrast, V_{OC} tended to decrease by less than 1.25%. These findings of I_{SC} increasing and V_{OC} decreasing when temperature rises are in agreement with those of Dash and Gupta [218]. Figure 4.5 shows the results from measurements taken for every 30 seconds of Sample 2 with 2.2 Ω attached resistor.

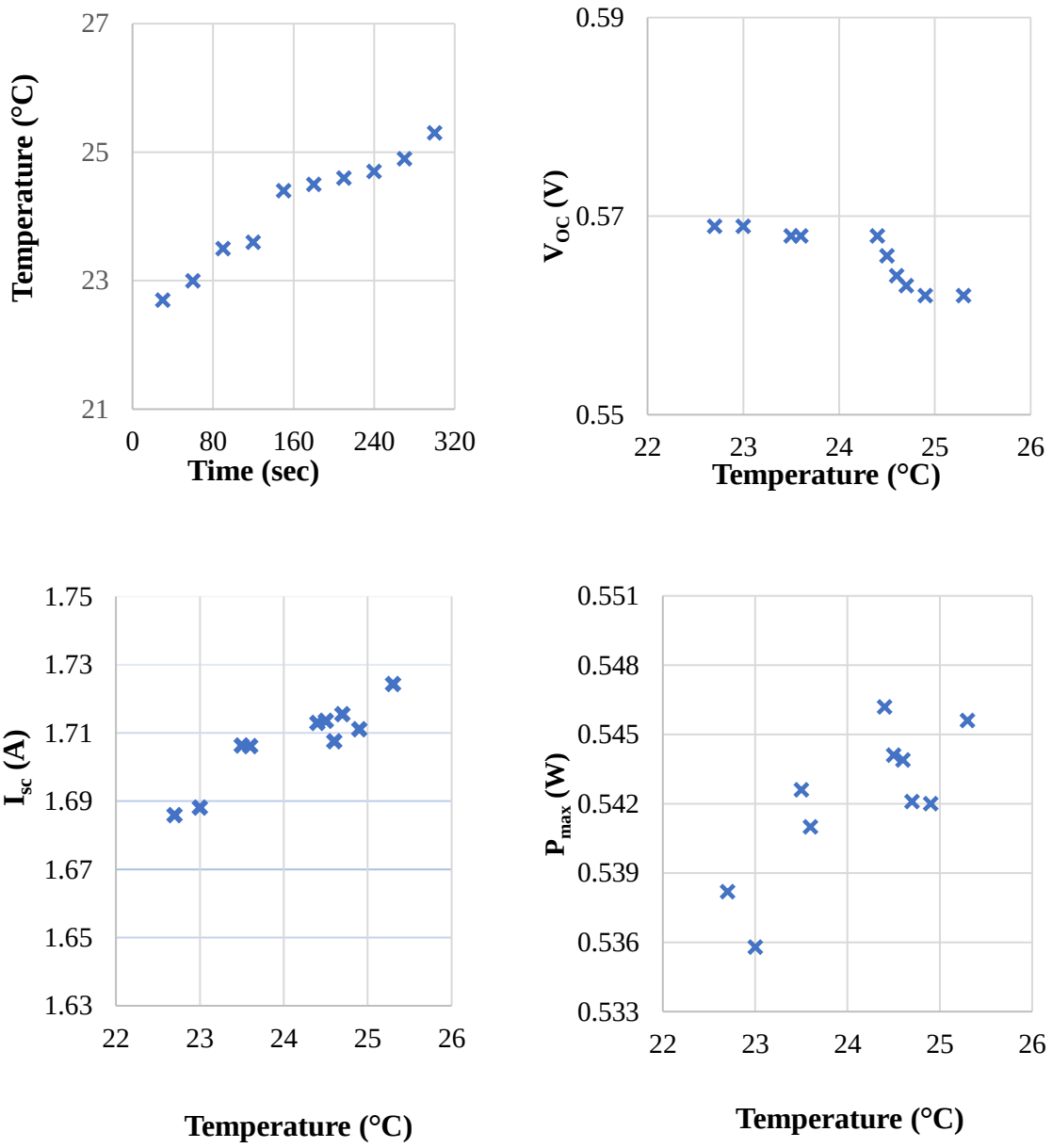


Figure 4.5 10 Measurements taken for every 30 seconds of electrical parameters of Sample 2 with a parallel resistor of 2.2 Ω.

4.4 Results and Discussion

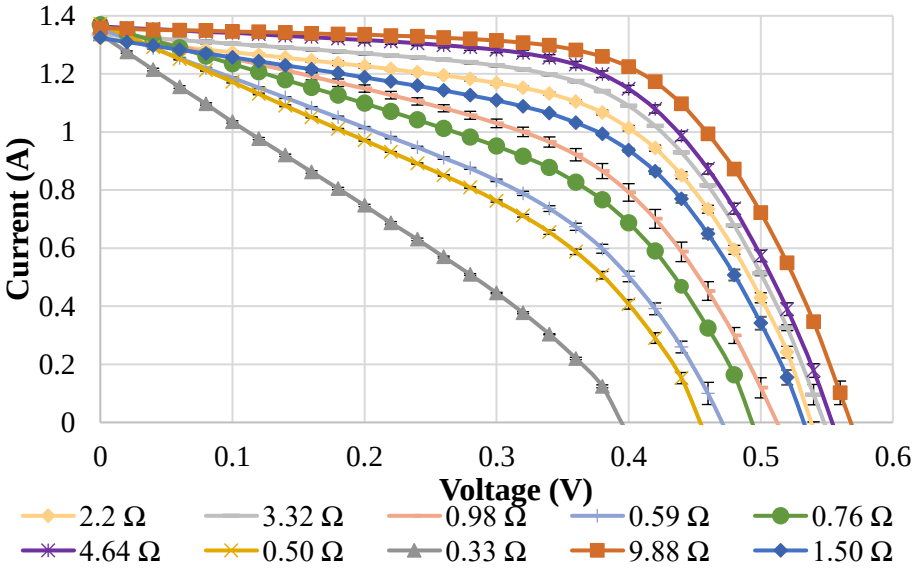


Figure 4.6 The mean I-V curves from 10 measurements of the second sample for different externally added resistors; ± standard deviation error bars were calculated and presented in the figure.

Adding the external resistors lowered the shunt resistance of all cell samples and altered their *I-V* curve characteristics substantially. Figure 4.6 shows the *I-V* curves of the second sample cell generated after lowering the shunt resistance.

It was noticed that significant deterioration of the *I-V* curve occurred after adding 9.88 Ω (592.8 Ω cm^2), which lowered R_{sh} to 516.2 Ω cm^2. No significant effect was observed on the *I-V* curve when R_{sh} was above 516.2 Ω cm^2 for all five samples. Deterioration became more severe when the 2.2 Ω resistor was added, which lowered the R_{sh} to just above 127 Ω cm^2, until the *I-V* characteristic collapsed when adding the 0.5 Ω resistor, resulting in R_{sh} of approximately

30 Ω cm^2. It was observed that V_{OC} reduced more significantly with reduced R_{sh}. I_{SC} was more affected by irradiance fluctuations.

4.4.1 Effect of Low Shunt Resistance on Open-Circuit Voltage, Maximum Output Power and Fill Factor

In contrast to the short-circuit current, the maximum power, fill factor and open-circuit voltage all changed in proportion to the shunt resistance. Of these three parameters, maximum power shows more drastic reduction. Figure 4.7 shows the correlation between reduction in shunt resistance and these parameters using Sample 2 and 5 as an example. The results were similar across all samples, deviating by less than 6 %. For instance, P_{max} was reduced by 50% when the shunt resistance was approximately 30 Ω cm^2 for all measured solar cells.

The reductions in fill factor and open-circuit voltage can be correlated with shunt resistance levels. The initial decrease in these values follows a linear relationship with shunt resistance until the shunt resistance reaches around 100 Ω cm^2. At this point, the slope increases significantly indicating a severe degradation of the solar cell performance.

According to the Electrical Power Research Institute [50], a photovoltaic module is considered to have failed when the maximum output power is 50% lower than the rated power. By this definition, the cells failed when the shunt resistance was at 29.8 Ω cm^2. However, abnormal changes when P_{max} was reduced by 20% are still noticeable and can be used as a cautionary threshold to proceed with more investigations of the PV system to avoid irreversible power degradation and

catastrophic failure. It is worth highlighting that a 20% reduction in output power was considered a failure by Jordan and Kurtz [49].

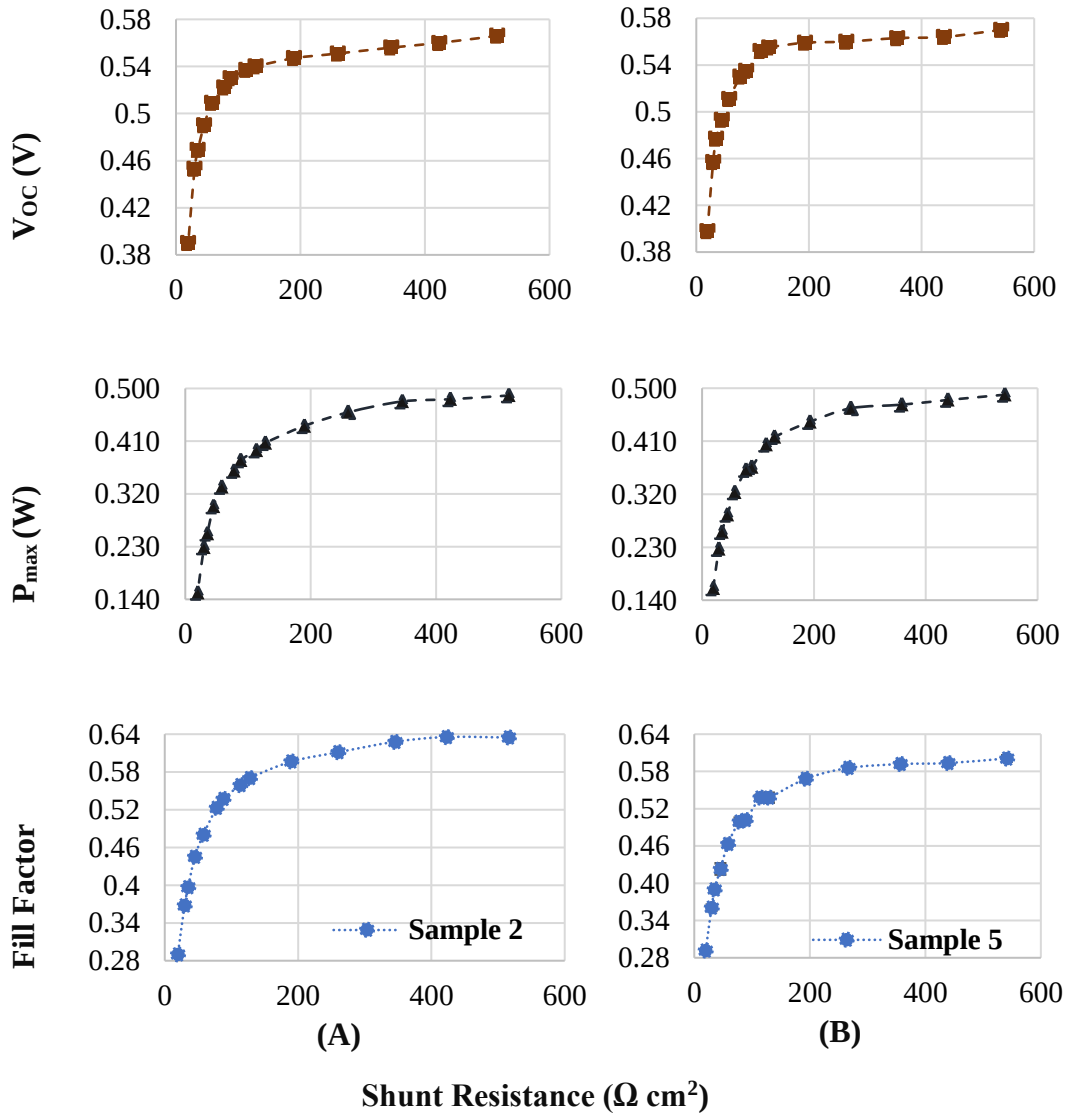


Figure 4.7 V_{OC}, P_{max}, and fill factor versus shunt resistance for Samples 2 and 5, the points represent the mean value of ten measurements. ± Standard deviation error bars were negligibly small and omitted from the figures.

As shown in Figure 4.7, the reduction in open-circuit voltage is smaller relative to the reduction in maximum power, making it more difficult to observe above shunt resistance value of 100 Ω cm^2, although the monitoring system should observe the changes. The reduction in open-circuit voltage becomes more obvious below 100 Ω cm^2.

The fill factor follows a similar pattern to the maximum power; however, the fill factor is a more sensitive parameter than maximum power for detecting PV degradation related to the reduction in shunt resistance for two main reasons. Firstly, the fill factor is not affected by degradation and failure in the PV encapsulation, unlike P_{max} [178], and secondly, the fill factor is more likely to reduce with shunt resistance reduction even in the presence of fluctuations in irradiance, i.e., some measurements with lower shunt resistance were exposed to a higher irradiance which increased P_{max}, but the fill factor continued to reduce. For example, in the first sample, the irradiance measured when the shunt resistance was 418.7 Ω cm^2 was higher than that received when the shunt resistance was 509.4 Ω cm^2, giving a higher maximum power at the lower shunt resistance. By contrast, the fill factor decreased with reducing shunt resistance. This means that the fill factor is a potentially robust determinant of degradation linked to shunt resistance in operational modules which are subjected to constantly varying irradiance.

To conclude this section, all three parameters, open-circuit voltage, maximum power, and fill factor, were reduced by reducing shunt resistance. Maximum power was the most significantly affected parameter. However, to distinguish between shunt resistance degradation and other PV failure mechanisms the reduction in maximum power should be matched by a decrease in the fill factor and open-circuit

voltage. The drop in open-circuit voltage was small until the shunt resistance reduced below 100 Ω cm^2.

4.4.2 Verification of the Measurements

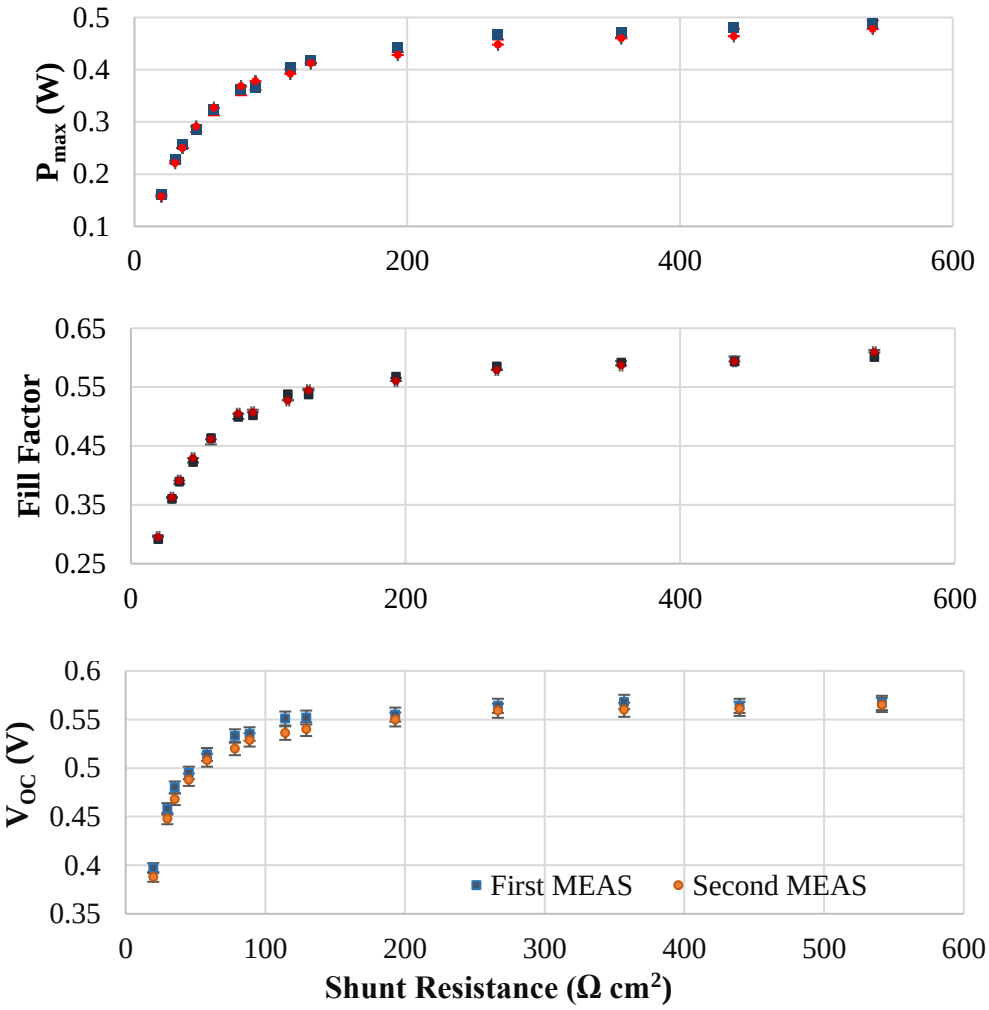


Figure 4.8 Electrical parameters of the 1st and 2nd Measurements (MEAS) of Sample 5. Error bars refer to the difference in two experiments conditions due to irradiance and temperature fluctuations.

The second, third, and fifth samples were stored in the lab for four weeks for measurements repetition to verify the measurements were not arbitrarily obtained. The first and the repeat measurement results were matched after considering the errors relating to temperature and irradiance differences. Figure 4.8 shows the 1st and 2nd measurements of sample 5.

4.4.3 Reducing the Surface Area of Solar Cell

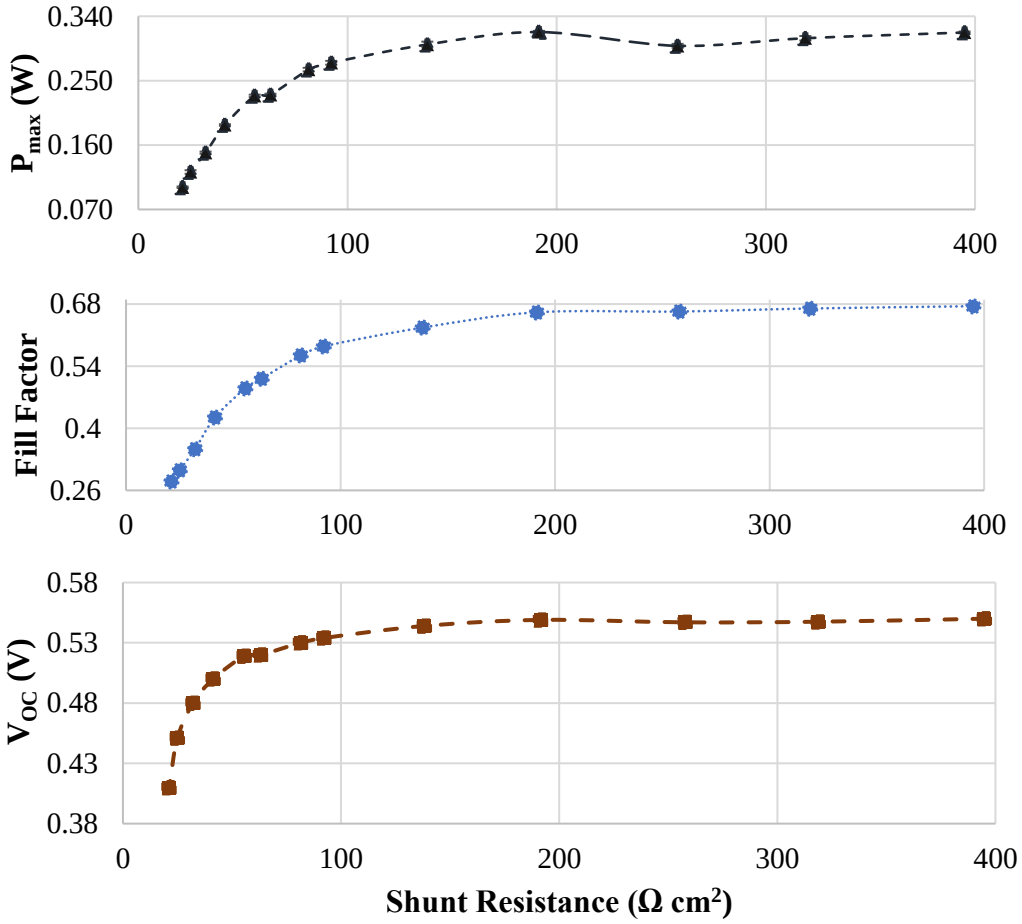


Figure 4.9 Electrical parameters of Sample 3 with a reduced surface area of 42.5 cm^2.

As shunt resistance is multiplied by the surface area, it increases in larger cells and decreases in smaller cells. Thus, the expected results of lowering shunt resistance in larger solar cells should be less severe than in smaller cells. In this regard, one other plastic lid was used to change the cell's surface area to 42.5 cm^2. As expected, results showed more significant degradation in the cell with a smaller surface area than the cell's samples with a larger surface area. This provides further validation that the measurements were conducted appropriately. Figure 4.9 showed the electrical parameters of the 3rd cell sample with decreased surface area to 42.5 cm^2. A deviant jump can be seen from the P_{max} correlation graph after around 258 Ω cm^2 which was caused by fluctuation in irradiance.

4.4.4 Determining the Critical Degradation Point for Solar Cell

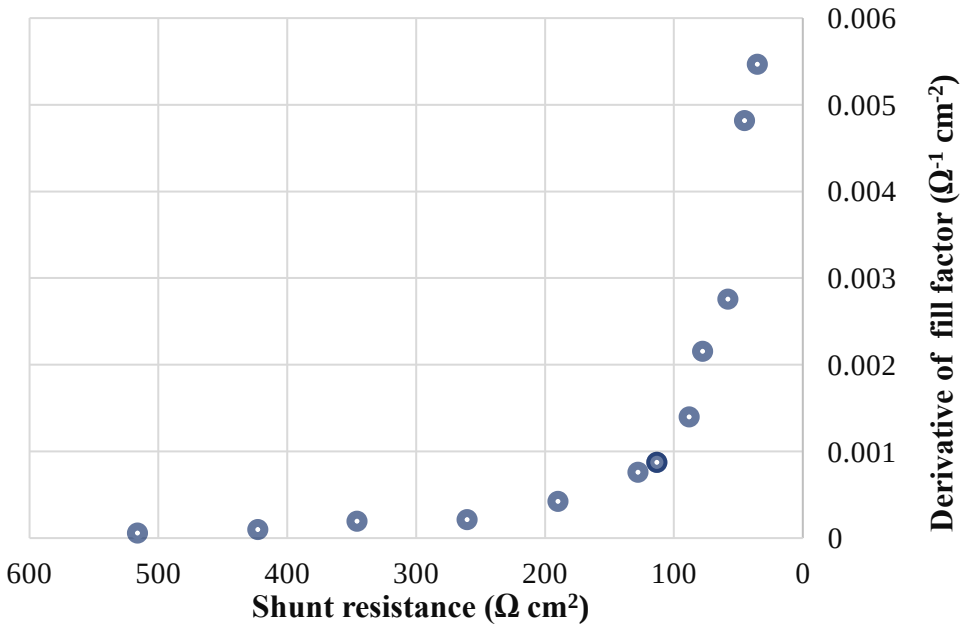


Figure 4.10 The derivative of fill factor with respect to shunt resistance vs shunt resistance values for the second cell.

The critical degradation point can be found by looking at the derivative of the fill factor with shunt resistance. As illustrated in Figure 4.10, for the second solar cell sample, the degradation of the cell started around 350 Ω cm^2 until it turned toward critical deterioration at *c.* 100 Ω cm^2. In this case the maximum power, open-circuit voltage and fill factor have been reduced by 25%, 7%, and 17% respectively from their initial values.

4.4.5 Modelling the Onset of Shunt Resistance Degradation

The results have clearly shown the deterioration of the sample cell performance due to the reduction in shunt resistance indicating PV degradation or failure. As there was no significant impact on short-circuit current, it can be treated as a stable metric to signify any change in the other parameters. Therefore, using the same concept previously presented to detect EVA degradation in Chapter 3 [178], a simple linear fit model that employs open-circuit voltage is proposed to detect the onset of critical PV degradation or failure related to shunt resistance.

To obtain this relationship experimentally, the irradiance was increased to the 1200-1220 W m^{-2} range. Increasing the irradiance increased the I_{SC} to 1.71 A and boosted the P_{max} to 0.634 W. The irradiance was reduced gradually over eight steps: 1135 W m^{-2}, 950 W m^{-2}, 865 W m^{-2}, 780 W m^{-2}, 710 W m^{-2}, 670 W m^{-2}, 625 W m^{-2} and 570 W m^{-2}. Two measurements were taken at each reduced level, one taken at reduced shunt resistance. The two measurements generated the same $I_{SC,}$ but the lower shunt resistance produced a lowered value of P_{max} and V_{OC}. The change in open-circuit voltage shown in Figure 4.11 is small with changes in irradiance, as expected [5, 7, 219]. Its reduction is relatively small when compared

to P_{max}, giving a relatively small slope. However, the open-circuit voltage is reduced at lower R_{sh} and can be linearly correlated with shunt resistance reduction until reaching the turning point around 100 Ω cm^2, showing a significant slope increment.

In this regard, both measurements are employed to derive linear models relating I_{SC} to P_{max} and $V_{OC,}$ as illustrated in Figure 4.11. Variations in the reproduced values of I_{SC} due to reasons mentioned earlier in Section 4.3 were kept below 2%. As observed in Figure 4.11, when the solar cell is affected by reduced $R_{sh,}$ the I_{SC} versus P_{max} has almost double the slope obtained when only the irradiance is reduced. By calculating the slope of P_{max} and regularly monitoring V_{OC} against I_{SC}, these two models together can be used to detect the early onset of critical PV degradation in a way that measurement of a single one of these parameters cannot.

Typically, solar irradiance begins to fall in the afternoon as part of the diurnal cycle. As it gradually reduces, the I_{SC} versus P_{max} and V_{OC} levels can be recorded as a control model. Routinely, at the same levels of I_{SC}, the P_{max} and V_{OC} levels can be monitored; if the slope increases compared to the control model, it can be determined that the onset of PV degradation or failure mode has begun in the PV module. The fill factor may also be followed to verify this abnormality. Employing I_{SC} instead of irradiance is cost-effective for a residential PV system as there will be no requirement for irradiance measurement tools.

Both the EVA degradation model presented in Chapter 3 *[178]* and the model proposed in this Chapter indicated a reduction in P_{max} in response to different degradation modes, however, the extent of the reduction due to R_{sh} degradation is more substantial.

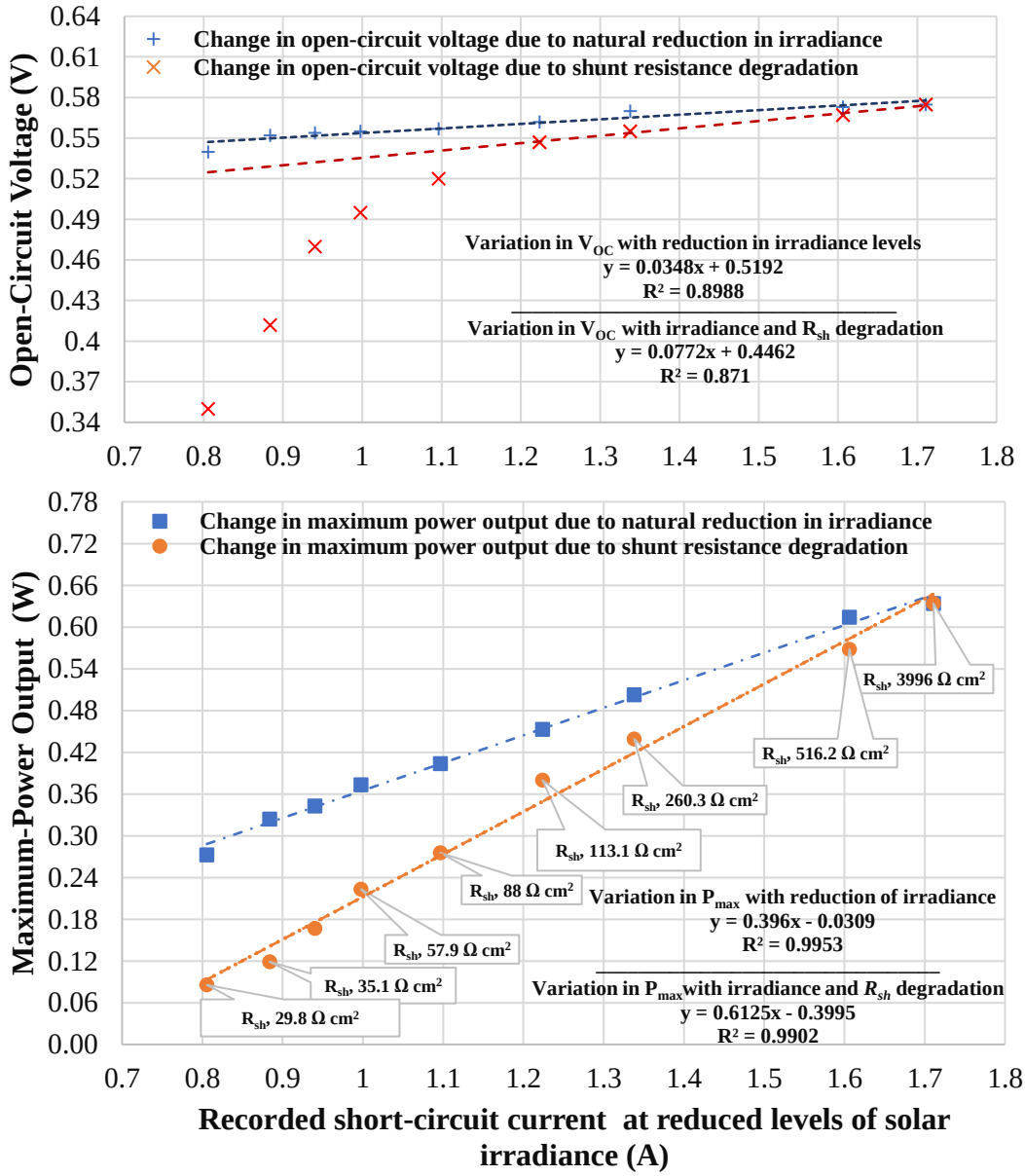


Figure 4.11 Linear models correlate Isc vs V_{OC} and P_{max}, for solar cells in healthy and degraded (reduced shunt resistance) states. Employing I_{SC} instead of irradiance is cost-effective for a residential PV system as there will be no requirement for irradiance measurement tools.

The distinction between the two models can be made through I_{SC} and fill factor: (a) I_{SC} was reduced in the EVA degradation from the early stages of degradation but was not reduced in the case of shunt resistance degradation; (b) the fill factor decreased with reduced shunt resistance but remained almost constant in the case of EVA degradation.

4.5 Conclusion

This chapter introduced a way to experimentally decrease the shunt resistance of a solar cell; each shunt resistance value generated an *I-V* curve characteristic indicating the extent of the cell deterioration, relative to the undeteriorated state. The work presented in this chapter took a different approach than widely cited articles, experimentally lowing the solar cell's shunt resistance and extracting its *I-V* parameters. Table 4-2 compares two available articles and the experimental approach followed in this chapter.

Extensive experiments were conducted to arrive at a robust result. Open-circuit voltage, maximum power output, and fill factor were found to be directly affected by reduced shunt resistance levels. The derivative of the fill factor with respect to the shunt resistance as a function of shunt resistance levels was considered to extrapolate the critical shunt resistance point, providing a threshold level for corrective action to be taken. The critical point turned out to be *c*. 100 Ω cm^2, and the reduction in V_{OC} and P_{max} before reaching this point were quantified.

I_{SC}, on the other hand, was not affected; on this basis, linear models were derived and proposed correlating V_{OC} and P_{max} as a function of I_{SC} (acting as a proxy for irradiance) to detect R_{sh} degradation. These models can be easily applied

to detect the onset of critical PV degradation or failure caused by shunt resistance degradation. The R_{sh} levels investigated in this study can start the next chapter on modelling and simulation of defective PV modules, simulating scenarios where the PV module contains solar cells degraded by low shunt resistance.

Table 4-2 The approach used by widely-cited shunt resistance articles and the one followed in this chapter.

Scientific Articles versus Existing Work	Approach Used
McMahon *et al*. [220].	Investigating three low levels of shunt resistance on a PV module that consists of twelve cells. Where each cell has a lowered value of R_{sh}. PV module parameters ($P_{max,}$ $I_{SC,}$ fill factor and V_{OC}) were not assessed despite the module's efficiency being evaluated. Results were not employed to develop a model to detect PV failures.
Dyk and Meyer [187].	Followed the same experimental approach by McMahon *et al*. [220] to experimentally evaluate the shunt resistance of a CIS module after outdoor exposure of 130 kWh m^{-2}. PV module parameters ($P_{max,}$ $I_{SC,}$ fill factor and V_{OC}) were evaluated at one low level of shunt resistance. Limited results were not employed to develop a model to detect PV failures related to shunt resistance.
Existing Work	Experimentally lowered R_{sh} in a novel and simple way into 14 levels. $P_{max,}$ $I_{SC,}$ fill factor and V_{OC} parameters due to low R_{sh} were quantified. Results were employed to develop a novel model that detects the early onset of PV critical degradation.

5 Chapter 5 | Early Prediction of Failed Cells in a PV Module Using Open-Circuit Voltage

In the previous chapter, we proposed linear correlations to predict shunt resistance degradation and failure mechanisms in PV cells. Some PV failures begin with a few cells in the PV module and then distribute to the other cells. In this chapter, the effect of PV cells with low shunt resistance on a PV module is studied using SPICE simulation. The simulation follows four steps: simulation of the healthy *I-V* curve of the PV cell; simulation of eleven *I-V* curves at a reduced level of shunt resistance; simulation of a PV module using the simulation parameters obtained from former steps; and lastly, simulation of four different scenarios depending on the number of faulty cells in a PV module. The effect of these scenarios on the *I-V* curve parameters is compared. A linear model correlating open-circuit voltage with I_{SC} (acting as a proxy of Irradiance) at different shunt resistance levels shows that it is feasible to detect failed cells (reduced R_{sh}) in a PV module.

5.1 Introduction

Increased demands for renewable energy across the globe to restrain air pollution and slow the rate of climate change have positively impacted the photovoltaics industry. According to [221], the growth rate of photovoltaics between 2004-2009 was remarkable, as high as 49%. It even surpassed 50% in some years of the last decade [222]. With such a high growth rate, the development of photovoltaics simulation programs skyrocket. The primary purpose of these

commercially available simulation tools is to assist manufacturers or researchers in conducting further investigation scenarios to forecast and record the power output of PV modules or array systems at different weather conditions.

A study by Chouder *et al.* [223] utilized LabVIEW™ (Laboratory Virtual Instrument Engineering Workbench) software tool for online monitoring of PV system. The same author has adopted the MATLAB software tool to predict the power generation from a grid-connected PV system [224]. It has also been adopted by Jiang *et al.* [225] to simulate the *I-V* curves at different solar irradiances and different ambient temperatures.

Researchers also benefited from these simulation programs to investigate scenarios of PV failures and degradations to assist in avoiding, predicting, and detecting them, hence protecting the PV system. For example, a shading scenario, a common failure mode in PV, was simulated Using MATLAB in different studies, e.g., [123, 226]. A brief review of simulation studies to address the effect of shunt resistance has been shown e.g., [7, 186, 227] (Refer to Chapter 2). Consequently, a unique method was presented to artificially lower the shunt resistance has resulted in the development of novel models to detect failures and degradations related to shunt resistance (Refer to Chapter 4).

However, many PV failures start with one cell or a few cells, such as PID, burnt cells (burn marks), soldering, and microcracks failures. These early-stage failures, when they occur, have only caused minor impacts on the PV module's electrical parameters, i.e., these minor impacts lead to minor power losses that will be difficult to detect. After a short time, they will trigger more defects in the PV

module's components and lead to severe failures and degradations, reducing the module's lifetime significantly [36, 54, 115, 151, 176, 228-230].

Since most of these failures and degradations were linked to reducing shunt resistance of a solar cell [181, 183-185], this chapter investigates the effect of low shunt resistance cells performing in a typical PV module using SPICE. Experiencing the behaviour of solar cells with low R_{sh} when they exist in a PV module is crucial for failure and degradation prediction, particularly for defects starting with a few cells in a PV module. Thus, simulation of PV module with four different scenarios, depending on the number of cells with degraded shunt resistance is performed in Section 5.3. Key results from analysing the simulation outputs of the PV module's parameters, maximum power output, open-circuit voltage, and fill factor are introduced and discussed in Section 5.4.

5.2 SPICE Model for Solar Cell

The same approach outlined by Castaner and Silvestre [5] (Refer to Chapter 3) has been adopted to model the impact of low shunt resistance cells in PV modules. The adopted SPICE model follows four steps:

Step 1: Simulation of the solar cell's experimental *I-V* curves generated at different shunt resistance levels.

Step 2: Simulation of a PV module that consists of 36 solar cells connected in series.

Step 3: Simulation of four scenarios based on the number of low R_{sh} cells in a PV module; A) PV module has only one cell with low R_{sh}. B) PV module has two cells with low R_{sh}. C) PV module has three cells with low R_{sh}. D) PV module has

six cells with low R_{sh}. The influence on the PV module performance will be analysed using the generated PV module's *I-V* curves from the simulation scenarios. This assists in identifying faulty cells in a PV module.

5.2.1 Equivalent Circuit Model of Solar Cell Used in SPICE

Many equivalent circuit models have been presented in the literature [7]. The approach outlined by Castaner and Silvestre [5] started from the ideal solar cell model which describes the theory of photovoltaic; the current of the cell is gained from the generated photo-currents density (J_L) subtracted from the dark current density (J_0). The photo-currents density is also referred to as short-circuit current density as seen in Eq. (5.1) [5]:

$$J = J_{sc} - J_0\left(e^{\frac{V}{V_T}} - 1\right) \tag{5.1}$$

The J_{sc} value depends on the type of material of the semiconductor. The short circuit current density of the silicon semiconductor is the sum generated at the p-type material 'base' and the n-type 'emitter', both measured in A cm^{-2} (Refer to Chapter 3). Another formulated of current density at both surfaces: base, and emitter, called dark current density and is calculated as follows [5]:

$$J_{\text{dark}} = J_{\text{darkE}} + J_{darkB} = J_0\left[e^{\frac{V}{V_T}} - 1\right] \tag{5.2}$$

Where J_{darkE} is the dark current density of the emitter semiconductor, J_{darkB} is the dark current density of the base semiconductor, V is the voltage of the cell, and V_T is the thermal voltage both measured in volts.

The open-circuit voltage of the cell is the voltage when the current is zero and can be extracted as seen from Eq. (5.3) [5].

$$V_{oc} = V_T \ln\left(1 + \frac{J_{sc}}{J_0}\right) \tag{5.3}$$

The ideal circuit model cannot be used to simulate commercial PV cells for the reason that it does not account for the effect of series and shunt resistances. Commercial PV cells began to exhibit series and shunt resistances (Refer to Chapter 1).

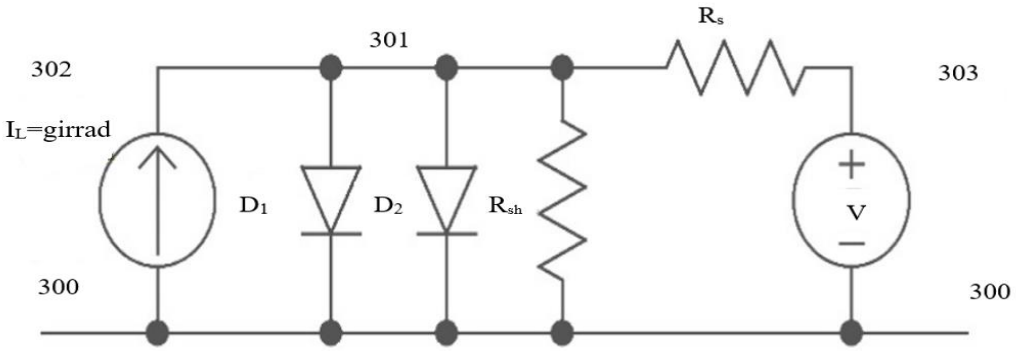


Figure 5.1 Equivalent circuit of two diodes model adopted in SPICE [5].

Three additional models have been introduced in the literature on top of the ideal circuit model to account for the series and shunt effects. They differ from each other by adding more parameters to maximise the model's accuracy. The single diode model, also mentioned as the five-point model, introduced the series and shunt resistances [213]. However, the SPICE model adopted by Castaner and Silvestre [5] has facilitated the second dark saturation current (J_{02}), with its non-ideality (n) factor, which corresponds to losses of recombination of the carriers in the space. Recombination is a phenomenon where electron returns from the conduction band to the valance band to maintain thermal stability [231], thereby

dropping the photons that have been already absorbed. By adding J_{02} to the model, the SPICE model follows the well-known two diodes model which was first demonstrated by Sah *et al.* [232]. The SPICE model equivalent circuit is shown in Figure 5.1.

Extraction of the PV cell parameters can be followed using Eq. (3.8) [5] which was presented earlier in Chapter 3:

$$I = I_L - I_0\left(e^{\frac{v+IR_S}{nV_T}} - 1\right) - I_{02}\left(e^{\frac{V+IR_S}{2V_T}} - 1\right) - \frac{V + IR_s}{R_{sh}} \quad (3.8)$$

Where the currents I,I_L I_0, and I_{02} are equal to their current density multiplied by the area of the solar cell in cm^2. Numbers 300 -302 in the circuit model presented in Figure 5.1 referred to the three SPICE nodes. These nodes are connected to a SPICE's subcircuit containing all listed equations, Eq.(5.1-5.3, 3.8) [5] to simulate the expected *I-V* curve of the solar cell.

Though studies elsewhere have proposed a three diodes model, e.g., [233, 234], it is not commonly used due to its complexity [7]. Thus, the SPICE model demonstrated and adapted by Castaner and Silvestre [5] has considered all necessary parameters to simulate the PV *I-V*'s characteristics with high accuracy.

5.3 Simulation of the I-V Curves at Degradation Modes

Six parameters of the solar cell are needed to run the SPICE model and to accurately estimate the PV cell's *I-V* curve. These parameters are: area of the solar cell, the current density, first saturation current density, the second saturation current density, series resistance, shunt resistance, and solar irradiance. The values of these parameters are inserted based on the experimental values. Then, they were

varied slightly until the simulated and the experimental *I-V* curves matched. The surface area of the solar cell was 60 $cm^{2,}$ and illuminated irradiance was measured to be 1000 ± 45 W m^{-2}. The irradiance is subjected to up to 4.5% fluctuations which were considered in the simulation (Refer to Chapter 4 for detailed explanations).

An accurate estimation of the shunt resistance value was obtained following the five-point extraction method presented in Chan *et al.* [213] (Refer to Chapter 4). The series resistance, on the other hand, can be estimated using the same extraction method by solving the following numerical set of equations [213]:

$$Rso = -\left(\frac{dv}{dI}\right) \qquad V = V_{OC} \tag{5.4}$$

$$R_{S=}Rso - \frac{nV_t}{I_0}\exp(-\frac{V_{OC}}{nV_t}) \tag{5.5}$$

$$A = V_m + R_{SO}I_m - V_{OC} \tag{5.6}$$

$$B = In\left(I_{sc} - \frac{V_m}{R_{sh}} - I_m\right) - In\left(I_{sc} - \frac{V_{OC}}{R_{sh}}\right) \tag{5.7}$$

$$C = \frac{I_m}{I_{SC-}\frac{V_{OC}}{R_{sh}}} \tag{5.8}$$

$$(the\ ideality\ factor\ of\ diode)\ \eta = \frac{A}{V_t\,(B + C)} \tag{5.9}$$

$$Diode\ Saturation\ crrent: I_0 = (I_{sc} - \frac{V_{OC}}{R_{sh}}) \exp\ (-\frac{V_{OC}}{\eta V_t}) \quad (5.10)$$

Where V_t is the thermal voltage calculated by kt/q , k is Boltzmann constant, t is the temperature of the solar cell in kelvin and q is the electronic charge. R_{so} is the slope at open-circuit voltage. I_m and V_m are the maximum current and maximum voltage, respectively. As Chan *et al.* [213] considered the single diode model only, unlike the SPICE model which considered the double diode model, the saturation current densities were varied until the simulated *I-V* curve matched the one from the experiment.

The first saturation current density was firstly estimated from Eq. (5.10). Its estimated value was inserted into the SPICE and varied along with the second saturation current density. Their magnitude ranges agree with Castaner and Silvestre [5] and Chan and Phang [235], where the first saturation current density and the second saturation current density ranges should be between 10^{-14}A cm^{-2} to 10^{-9} A cm^{-2}, and 10^{-9}A cm^{-2} to 10^{-6}A cm^{-2}, respectively. In addition to the 2nd cell *I-V* curve, eleven *I-V* curves at lowered shunt resistance values were selected to be simulated in SPICE among the fourteen values investigated in Chapter 4.

The strategy for picking these levels is the inclination of the *I-V* characteristics toward failure and collapse. They were the *I-V* curves of the 2nd solar cell at lowered shunt resistance; 516.2 Ω cm^2, 345.8 Ω cm^2, 260.3 Ω cm^2, 189.7 Ω cm^2, 113.1 Ω cm^2, 88.0 Ω cm^2, 77.7 Ω cm^2 57.9 Ω cm^2, 45.1 Ω cm^2, 35.1 Ω cm^2, and 29.8 Ω cm^2. Some of which were combined with the experimental ones and presented in Figures 5.2 and 5.3.

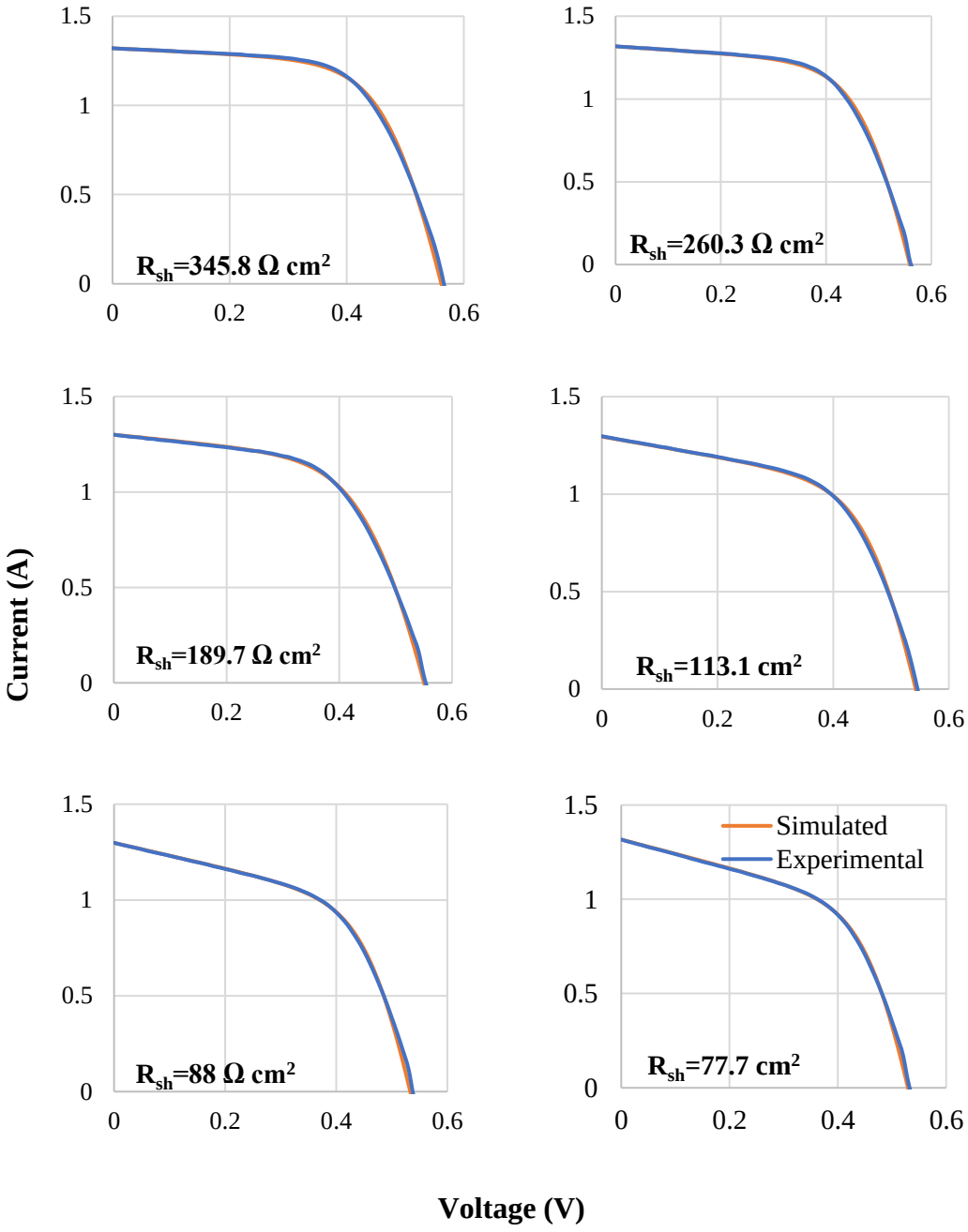


Figure 5.2 Simulation of I-V curves at different shunt resistance levels using SPICE.

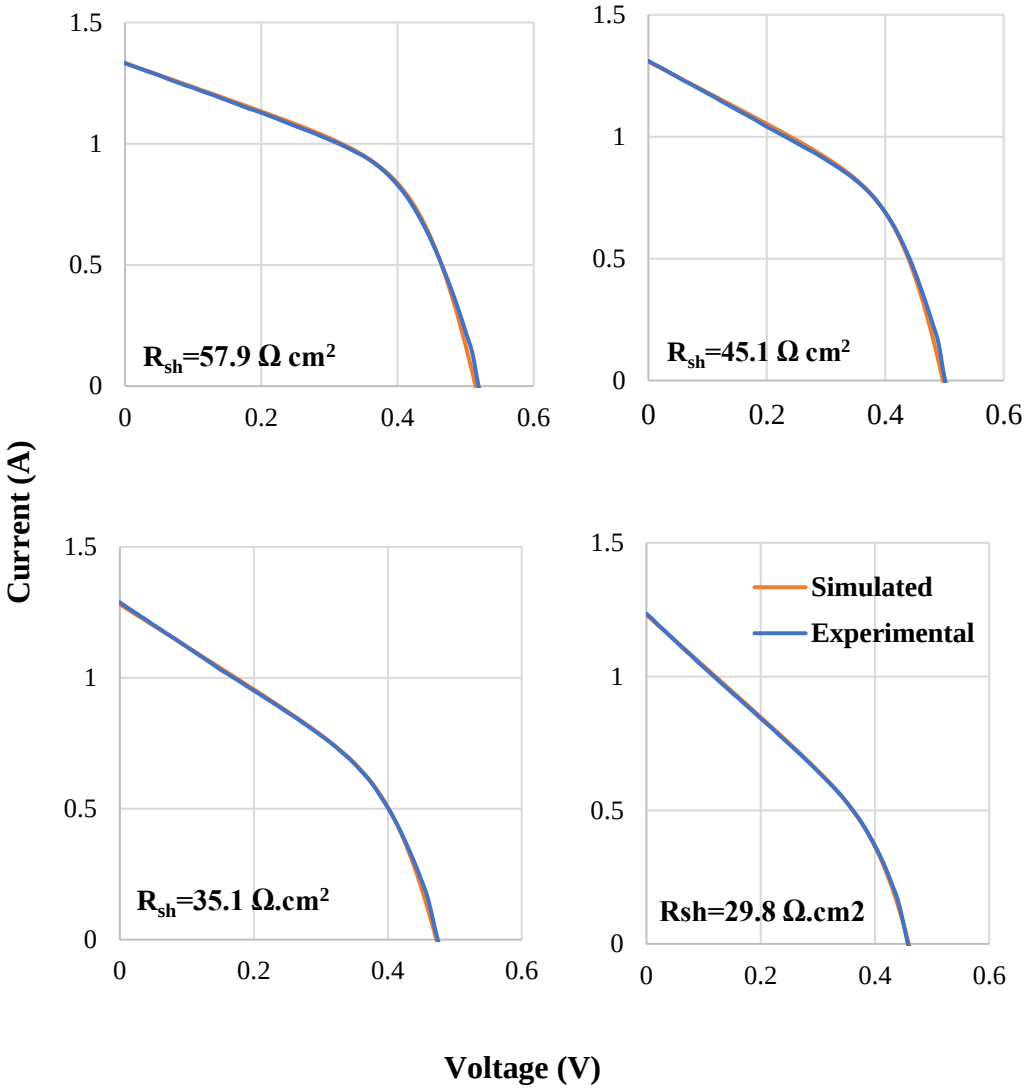


Figure 5.3 Simulation of I-V curves at different shunt resistance levels using SPICE.

Overall, the simulated *I-V* curve must match the values of short-circuit current, maximum output power, and the open-circuit voltage with the ones generated from the experiment. The simulated *I-V* curves were also compared to the experimental curves by calculating the Root Mean Square Error (RMSE). The RMSE of the 2nd

solar cell accounted for 0.017, indicating that the simulation model stands for high accuracy. Although RMSE was criticised by Willmott *et al.* [236] to be an ambiguous metric for model evaluation, it is assumed by Chai and Draxler [237] to be otherwise and even more appropriate over the Mean Absolute Error (MAE) model. For this purpose, the so-called Modelling Efficiency Formula (EF) as shown in Eq. (5.11) [238]. The result from Eq. (5.11) should be between 0 and 1 to indicate a good simulation model. Where 1 indicates a very accurate model.

$$\text{Efficiency Formula} = 1 - \left(\frac{\text{MSE}}{Measured\ Data\ Variance}\right) \tag{5.11}$$

Table 5-1 shows the RMSE and the EF values for the simulated *I-V* curves.

Table 5-1 Root Mean Square Error and Modelling Efficiency for the Simulated I-V Curves.

Shunt resistance (Ω cm$^{2)}$	**RMSE**	**EF**
3996	0.017	0.997
516.2	0.015	0.997
345.8	0.013	0.998
260.3	0.013	0.998
189.7	0.013	0.999
113.1	0.012	0.999
88.0	0.015	0.996
77.7	0.013	0.997
57.9	0.015	0.988
45.1	0.016	0.997
35.1	0.009	0.997
29.8	0.005	0.999

It is worth mentioning that some of the simulated *I-V* curves needed a slightly smaller value of shunt resistance to be inserted to match the experimental ones. The simulated *I-V* curves at shunt resistance of 77.7 Ω cm^2, 45.1 Ω cm^2, 35.1 Ω cm^2, and 29.8 Ω cm^2, have smaller R_{sh} values of 1.15%, 1.73%, 3.58%, and 5.24%, respectively. As it can be noticed, the error is likely to increase gradually with the reductions in shunt resistance. Series resistance was also increased with the reductions in shunt resistance gradually. It was increased by up to 80% in combination with the shunt resistance reductions. The 2nd saturation current densities were also gradually increased with shunt resistance reductions, albeit in the expected range magnitude. This agrees with McMahon *et al.* [220], that the decrease in shunt resistance increases the recombination losses.

To sum up, different cell parameters' values are needed to be adjusted in the SPICE circuit model. Despite following the numerical set of equations Eq.(5.4-5.10) [213] to extract their values accurately, their extracted values do not necessarily indicate the actual values of the experienced cell. Regardless, as long as their values are in the expected range and simulate similar *I-V* curves as those experimentally generated, it is then feasible to use these values to simulate the *I-V* curve for a PV module. By this means, investigating different scenarios where a PV module contains defective cells.

5.3.1 Simulation of PV Module's I-V Curve at Degradation Modes

In the experiment, the effect of decreasing shunt resistance in a single solar cell has been investigated (Refer to Chapter 4). It was concluded that three major parameters P_{max}, FF, and V_{OC} were degraded significantly. However, solar cells are

rarely used alone (Refer to Chapter 1). The non-uniform decreasing of shunt resistance in solar cells, when packaged in a PV module, has not yet been accurately quantified.

SPICE is used to simulate the generated *I-V* curves from the repeated measurement of the 2nd solar cell with decreased R_{sh}. SPICE's tool is capable to include defective cells in a PV module to predict their negative effect on the output characteristics. By doing so, a PV module consisting of 36 solar cells is simulated by SPICE, which can be achieved by increasing the number of circuit nodes in the SPICE netlist.

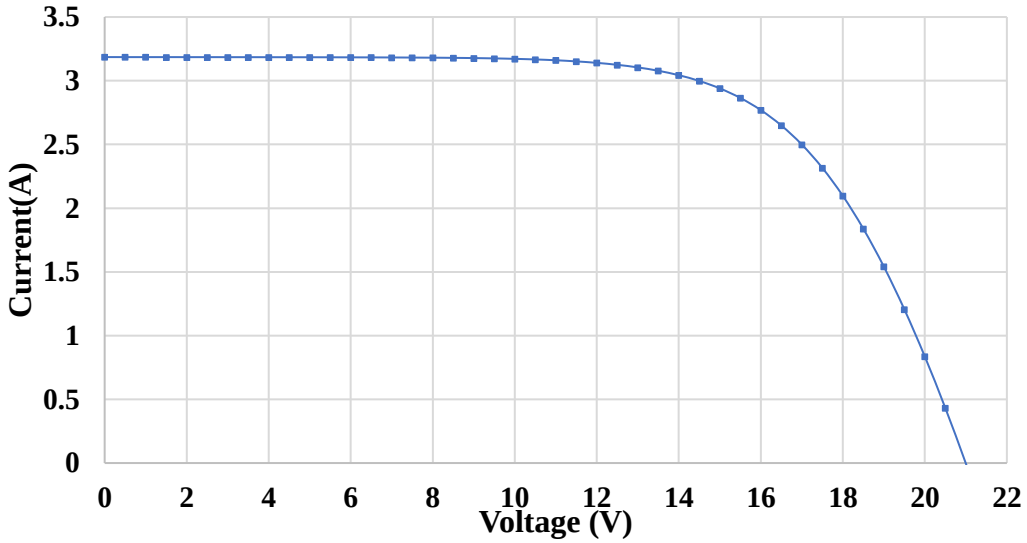


Figure 5.4 I-V curve of simulated PV module, consists of 36 solar cells connected in series using SPICE

Each circuit node represents one solar cell with its parameters' values. Only one subcircuit is needed to simulate a single solar cell. Increasing the number of circuit nodes to 36 will formulate a PV module consisting of 36 solar cells connected in series. The parameters' values can be modified for each cell, making it simple to examine the module's output characteristics with defective cells. The open-circuit

voltage was 0.585 V in a single solar cell and was increased by 36 fold in the module to become 21 V. The solar irradiance in the simulation was kept steady at 1000 Wm^{-2} in all module simulations. The area was increased from 60 cm^2 to 125 cm^2 which increased the short-circuit current to 3.18 A and boosted the maximum power output to 44.7 W. Figure 5.4 shows the generated *I-V* curve of the PV module.

5.4 Results and Discussion

From the *I-V* curves shown in Figure 5.5, the PV module's performance became poorer when containing more cells with low shunt resistance. Also, it can be seen that there is a correlation between shunt resistance levels and severity. The lower the shunt resistance becomes, the more severe the degradation on the module. The module characteristics: maximum-power output, fill factor, and open-circuit voltage will be extracted in the following sections for a better analysis of the resulting *I-V* curves.

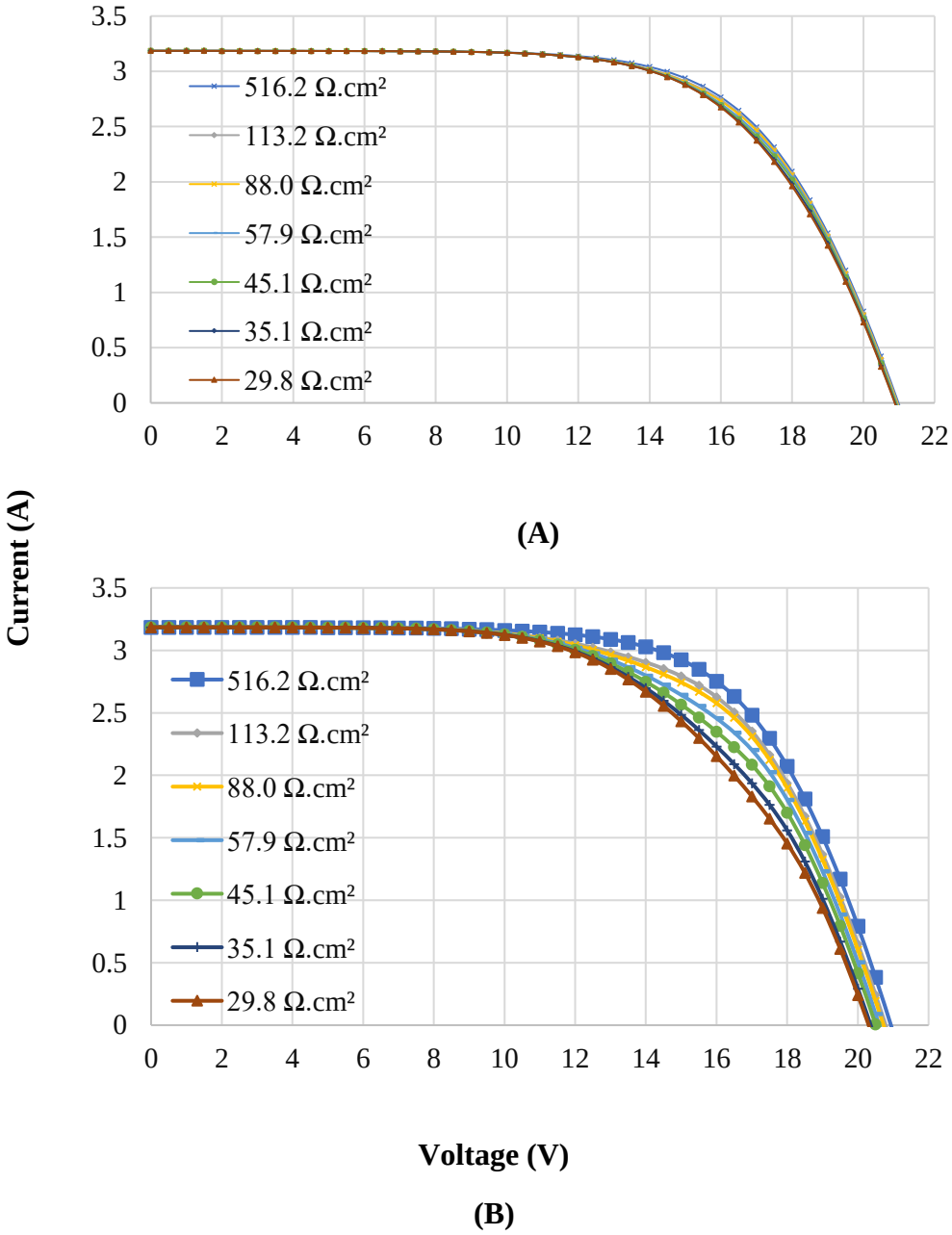


Figure 5.5 I-V curves for a PV module simulated using SPICE showing the effect of lowering shunt resistance in a different number of solar cells. Where (A) is one cell with low R_{sh} and (B) six cells with low R_{sh}.

5.4.1 Correlation between Fill Factor and Shunt Resistance

The derivative of the fill factor with respect to shunt resistance obtained from the experiment was used as a measure to calculate the failure turning point. Derivative is utilized as a microscopic scale measure to identify a system status turning point [239]. It was found that the turning point toward failure mode was around 100 Ω cm^2. This can also be concluded from the simulation results shown in Figure 5.6 for the PV module where there's almost a logarithmic correlation between the shunt resistances levels and the fill factor.

Figure 5.7 indicates the severity and can be used to estimate the time left for the PV module towards complete failure based on the number of defected cells. As mentioned earlier, in some failure mechanisms, the failure starts with a few cells and then distributes to the other cells [36, 115, 151, 228-230]. Therefore, the slope of the fill factor can be employed to detect the number of defective cells in the PV module, the slope became larger when more cells failed.

5.4.2 Correlation between Maximum Power Output and Shunt Resistance

The degradations' figure of the maximum power output has nearly the same trend as in the fill factor figure. Both figures formed almost two linear relationships, one above the turning point and one below the turning point. The one above refers to the slow degradation of a PV module. Once the shunt resistance reached the turning point *c.* 100 Ω cm^2, the PV module tends toward catastrophic failure.

Figure 5.7 shows that the pattern of the P_{max} is close to the fill factor; both demonstrate a relationship between the number of defective cells and the severity of the degradation.

Aside from the number of faulty cells, when shunt resistance decreased further, a higher decline was noticed in the module's P_{max} and fill factor. For instance, the reduction of P_{max} was more significant in a PV module having one cell at shunt resistance of 35.1 Ω cm^2 than in a PV module having six cells at shunt resistance of 260.3 Ω cm^2.

5.4.3 Correlation between Open-Circuit Voltage and Shunt Resistance

When comparing the change in open-circuit voltage at reduced shunt resistance with maximum power output and fill factor, the latter two declined more severely than the open-circuit voltage. Nevertheless, a slight reduction in V_{OC} can also be used to determine the degradation of the PV cell in the PV module. Figure 5.6 and Figure 5.7 clearly show the V_{OC} is impacted even if only a single cell was failed.

It is well known that whenever there is a PV degradation process, P_{max} will be the first parameter that indicates the failure [33]. And for this, the P_{max} model presented previously was accompanied by monitoring V_{OC} to distinguish between PV failures or degradations related to low shunt resistance and other failure mechanisms. However, it is feasible to employ the V_{OC} alone in detecting failed cells existing in the PV module. In Chapter 4, it was proven that even though the V_{OC} was reduced at natural reduction of solar irradiance [5, 7, 219], the slope of V_{OC}, in a linear relationship with I_{SC}, due to shunt resistance reduction was

significantly larger. Furthermore, the correlation to detect faulty cells in PV modules is continuously linear until approximately more than half of the PV module's cells failed. Unlike the model demonstrated in Section 4.4.5, Chapter 4, which showed the correlation between shunt resistance and V_{OC} turned to logarithmic after shunt resistance decreased to 88.0 Ω cm^2. This provides a great potential to employ V_{OC} alone to detect failed cells associated with low shunt resistance in a PV module.

In Figure 5.6-C, the reduction in V_{OC} was double when comparing one cell failed PV module with a two-cell failed module. According to Fuentes *et al.* [229], failed cells in PV modules decreased the average lifetime from twenty years to seven years. Using V_{OC} helps estimate the operation time left for the PV module when some solar cells failed, allowing corrective action to be planned and taken. Hence, a comparison between power loss, risks, and cost can be analyzed to determine the optimal time.

Moreover, a mathematical equation can be extracted in Figure 5.6-C to detect the number of failed cells, where the shunt resistance of the cell decreased to 29.8 Ω cm^2. This can be applied if the reduction magnitude in V_{OC} due to one failed cell can be identified. In this simulated module, approximately 0.115 V in V_{OC} was lost due to the failed cell. Thus, Eq. (5.11), can be proposed:

$$No.\,of\ failed\ cells\ in\ \text{the simulated } 36-\text{cells}-\text{PV module} = \frac{V_{OC}-V_{OCr}}{0.115} \tag{5.11}$$

Where V_{ocr} is the recorded open-circuit voltage and 0.115 is the difference between the open-circuit voltage of a healthy PV module and a PV module with one failed cell.

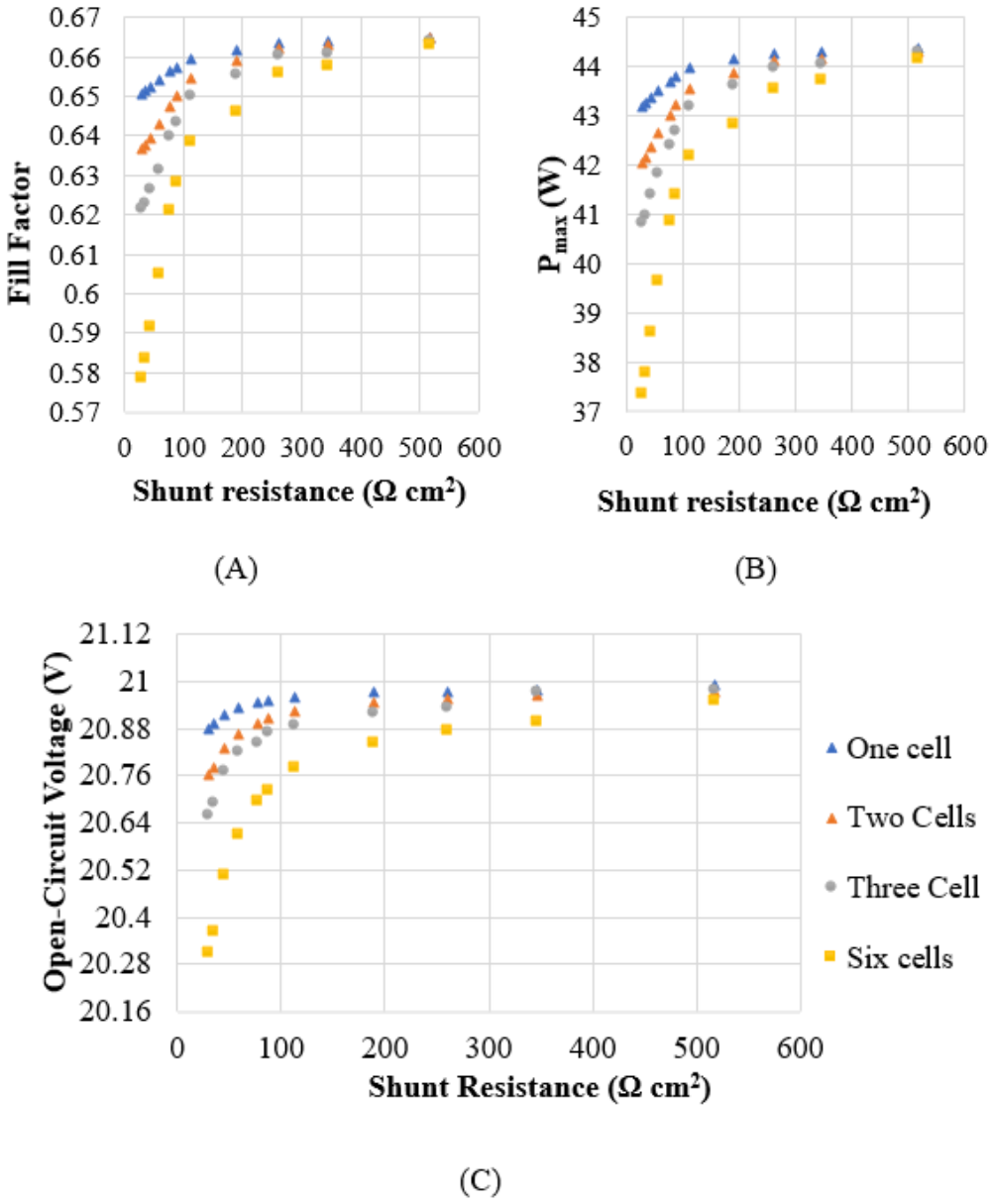


Figure 5.6 Correlation with PV module's shunt resistances and (A) fill factor, (B) Maximum-power output, and (C) Open-circuit voltage.

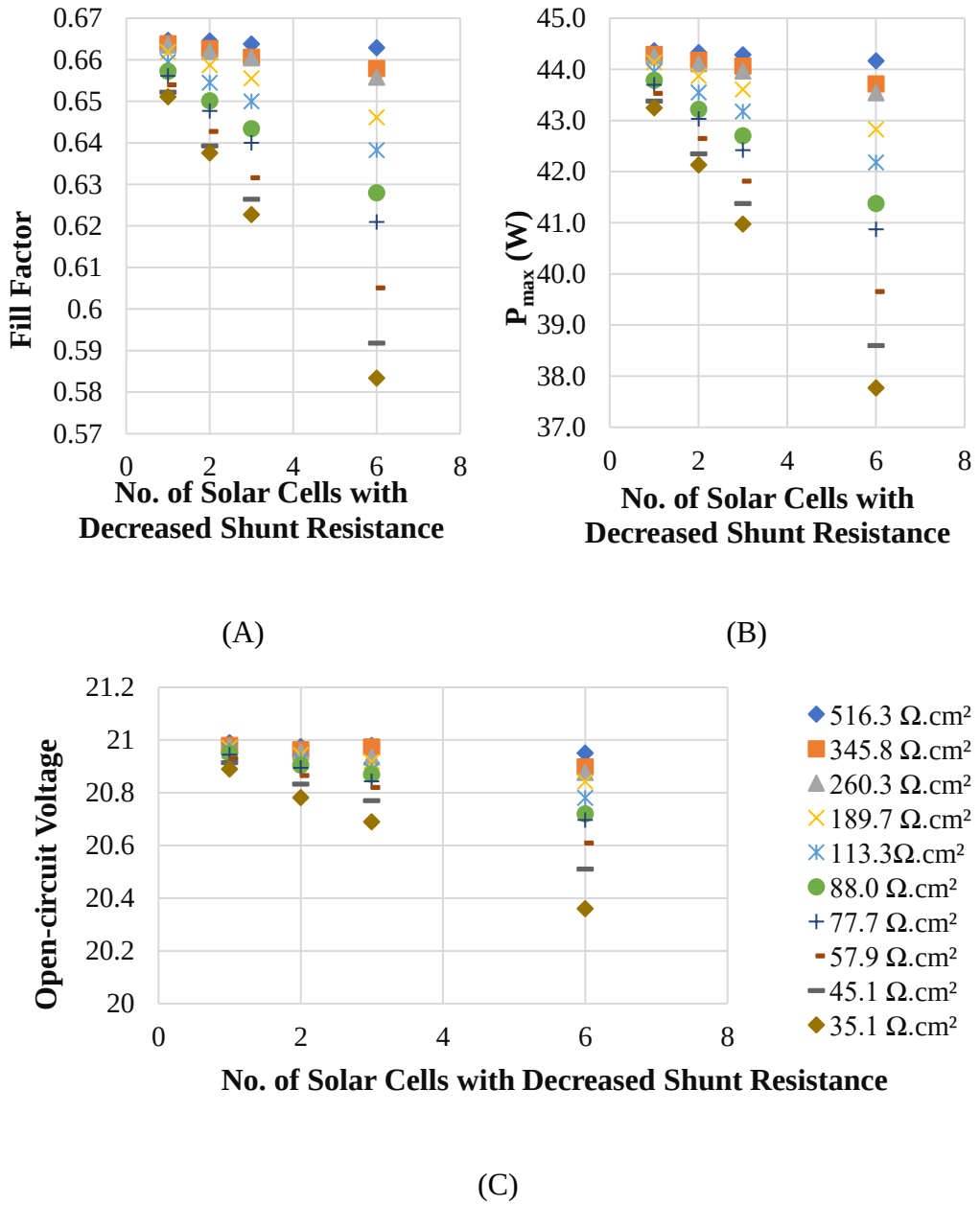


Figure 5.7 Correlation between the number of defective cells in PV module with the (A) fill factor, (B) Maximum-power output, (C) Open-circuit voltage.

5.4.4 Model to Detect Cells with Degraded Shunt Resistance in a PV Module

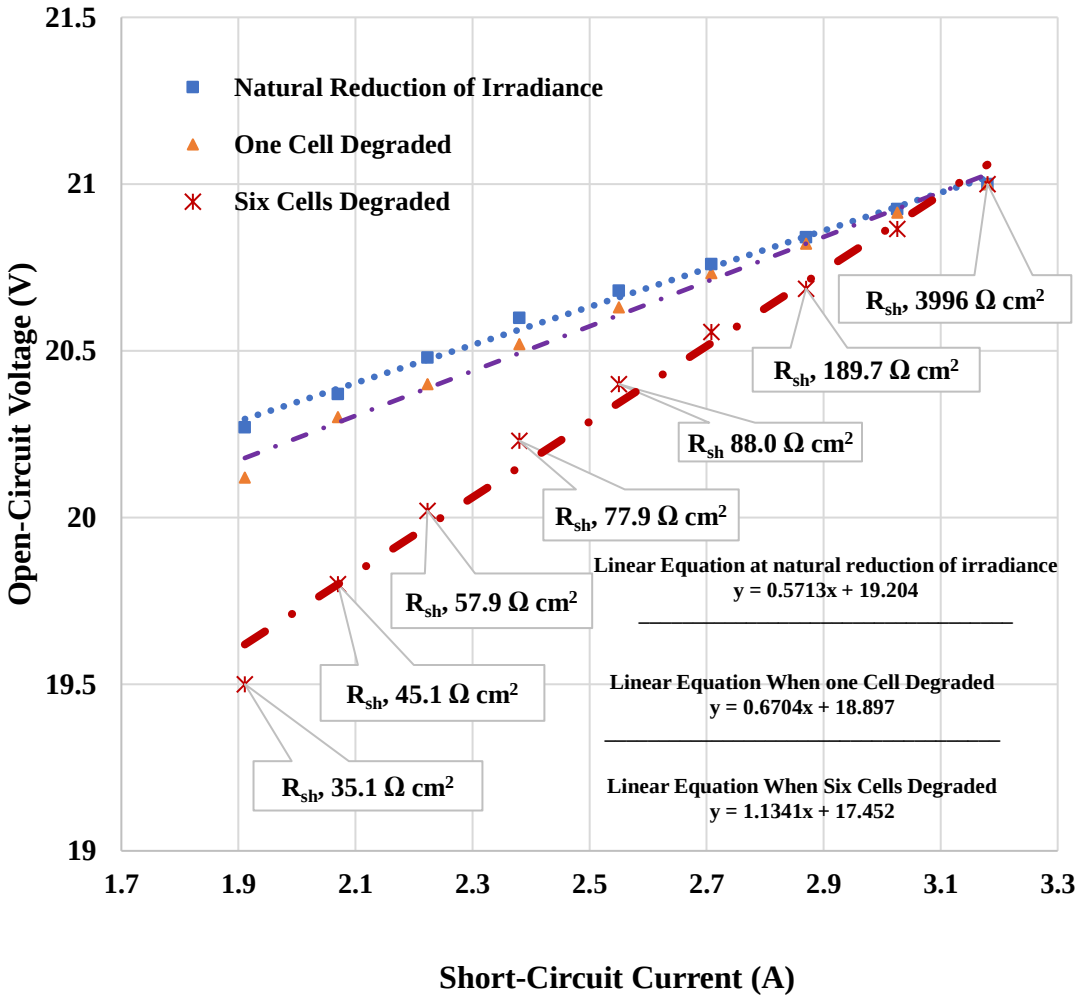


Figure 5.8 Linear fit models correlate I_{sc} and V_{oc} to compare between healthy and faulty states of a PV module, the model can be used to detect the onset of PV cells degradation or failure in PV module caused by shunt resistance reduction.

To make the model cost-effective for a residential PV system, this model also used short-circuit current as a substitute for solar irradiance to be correlated with open-circuit voltage as there will be no requirement for irradiance measurement tools.

As illustrated previously in Chapter 4, when solar irradiance begins to fall in the afternoon as part of the diurnal cycle, the short-circuit current versus open-circuit voltage levels can be recorded as a control model. Routinely, at the same levels of I_{SC}, the V_{OC} levels can be monitored; if the slope increases compared to the control model, it can be determined that a single solar cell has turned to failure or degradation mode in the PV module. This would be a great potential application of machine learning: extracting this diurnal pattern of solar irradiance and checking the corresponding I_{SC} and V_{OC} cycles and looking for deviations from their previous relationships, which would indicate the number of defective solar cells that exist in the PV module.

5.5 Conclusion

When one or more cells in a PV module fails or degrades, the module continues to generate significant power unless most cells become infected, ultimately leading to noticeable power reduction and catastrophic failure. Thus, this chapter has used the simulation of the PV module via SPICE to investigate the effect of failed cells linked to low shunt resistance in the PV module. These simulations help detect these failure mechanisms before a failure gets propagated to the neighbouring cells. The degraded or failed cell linked to low shunt resistance in a PV module was found to reduce the PV module's fill factor, open-circuit voltage, and maximum-power output. Results showed that it is still feasible to detect them by implementing

a simple linear fit model that correlates open-circuit voltage with short-circuit current as a proxy of solar irradiance. A mathematical equation was also proposed to detect the number of failed cells based on the reduction magnitude of the open-circuit voltage. The work presented in this chapter took a different approach than widely cited articles, aiming to detect failed cells by simulating the *I-V* curve of a typical PV module when existing solar cells with low shunt resistance. Table 5-2 compares two available articles and the simulating approach followed in this chapter.

Table 5-2 The simulation approach used by widely-cited shunt resistance articles and the one followed in this chapter.

Scientific Articles versus Existing Work	Approach Used
McMahon *et al*. [220].	Simulating three low levels of shunt resistance in a PV module that consists of 12- cells using PSpice. Simulated PV module parameters ($P_{max,}$ $I_{SC,}$ fill factor and V_{OC}) were not assessed despite the module's efficiency being evaluated. The effect of different numbers of cells with low shunt resistance on the PV module was not compared. Not mentioned if series resistance needed to be increased for accurate simulation.
Dyk and Meyer [187].	Used PVSIM to simulate the effect of two lowered shunt resistance. They showed that low shunt resistance decreased maximum power output, open-circuit voltage, and fill factor but increased short-circuit current slightly. Limited results were not employed to develop a model to detect failed cells in a PV module.
Existing Work	Simulating experimental *I-V* curve of low R_{sh} cell accurately to investigate the *I-V* parameters ($P_{max,}$ $I_{SC,}$ fill factor and V_{OC}) of a PV module with low R_{sh} cells. Results were employed to develop a novel model that detects the number of failed cells in a PV module.

Depending on the type of failure, shunt resistance degradation may relate to reversible or irreversible failure. The next chapter will demonstrate these two failures from experiments conducted at KFUPM. Furthermore, it can be suggested to classify them, whether they are reversible or irreversible, by using machine learning models.

6 Chapter 6| Failed PV Modules at KFUPM: Corrective Actions and the Potential of Machine Learning Applications

It was stated in the previous chapter that failures might be reversible and irreversible. This chapter shows examples through an experiment conducted in deployed PV modules at King Fahd University of Petroleum and Minerals, Dhahran, Saudi Arabia. *I-V* measurements of the PV modules affected by dust accumulation and hotspot were taken. Dust accumulation can be cleaned to restore power losses whereas only replacement of damaged module by hotspot is recommended. PV modules are exposed to many failures like this, some of which are reversible others are not. Within sufficient *I-V* data, these failures can be classified easily by training machine learning models. As an instance, this chapter presents a classification ML model between the degradation's mechanisms investigated in Chapter 3-5, EVA and shunt resistance degradations.

6.1 Introduction

When it comes to solar energy, Saudi Arabia is located in an exceptional geographical location on the planet, universally recognized as the sunbelt. In addition to the higher solar irradiance, most regions in Saudi Arabia are in clear-sky conditions on most days of the year [240]. Nevertheless, some Saudi cities face environmental stress factors, such as high relative humidity, hot air, and dust storms which reduce the power output of the PV modules substantially.

Dhahran city is one of those cities, the weather, in general, is dusty and combined with humid and hot air. This blend of environmental factors causes extreme stress on the PV module (Refer to Chapter 2). As explained earlier in Chapter 2 due to the severe impact of the dust in Dhahran, its characteristics were studied and explored [117]. Thus, the city was favoured to conduct an experiment to address the effect of dust accumulation on PV modules. The PV modules were deployed at KFUPM, Department of Electrical Engineering.

In addition, there was a PV module with one cell failed by a hotspot deployed at the same location. The *I-V* measurement of that PV module was also taken.

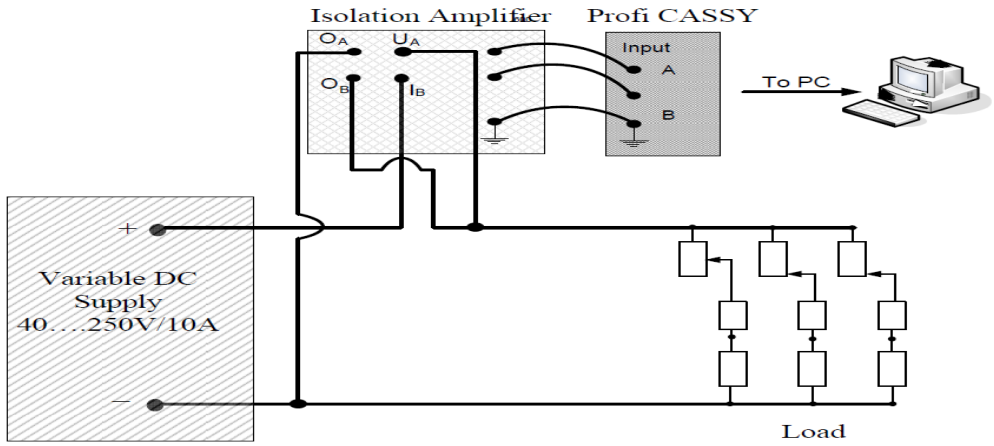
This chapter consists of two main sections; the first section outlines the effect of dust accumulation and hotspot failures on the PV module's parameters. The second section discusses corrective actions, and the potential application of the machine learning models.

6.2 Experimental Procedure and Results

The PV modules were connected to an isolation amplifier and Profi-Cassy sensor, Model No. LD-524 016, these two components worked as data acquisition system. During the experiments, the output parameters, current, and voltage signal were transmitted to the isolation amplifier to be scaled down to a suitable range for the Profi-Cassy sensor to read. The signals were then transmitted to the computer system to be presented and stored by the Profi-Cassy software as illustrated in the experiment set up in Figure 6.1.

The *I-V* curves were experimentally generated by connecting a resistive load bank to the PV module to vary its current value over a short period. The resistive

bank can gradually reduce a current of 3.0 A by increasing the load resistance from 1% to 100%.



(A)



(B)

Figure 6.1 (A) Typical experiment for DC measurement at KFUPM lab [241]. (B) Experiment set up for the dust accumulation and hotspot measurements.

Three resistive banks were connected in series to be able to decrease a current of 9.0 A gradually. The load resistance was progressively increased at roughly 40

points to generate the *I-V* curves of the investigated modules. Measurements of the current and voltage were taken at each point synchronously.

6.2.1 Effect of Dust Accumulation on PV Module Surface

The weather condition in Dharan is hot with high relative humidity and dusty most of the time. The experiment was conducted on poly-crystalline modules for a duration of three days. Even though the time used for the experiments is considerably short, the results show a significant influence on PV module parameters.

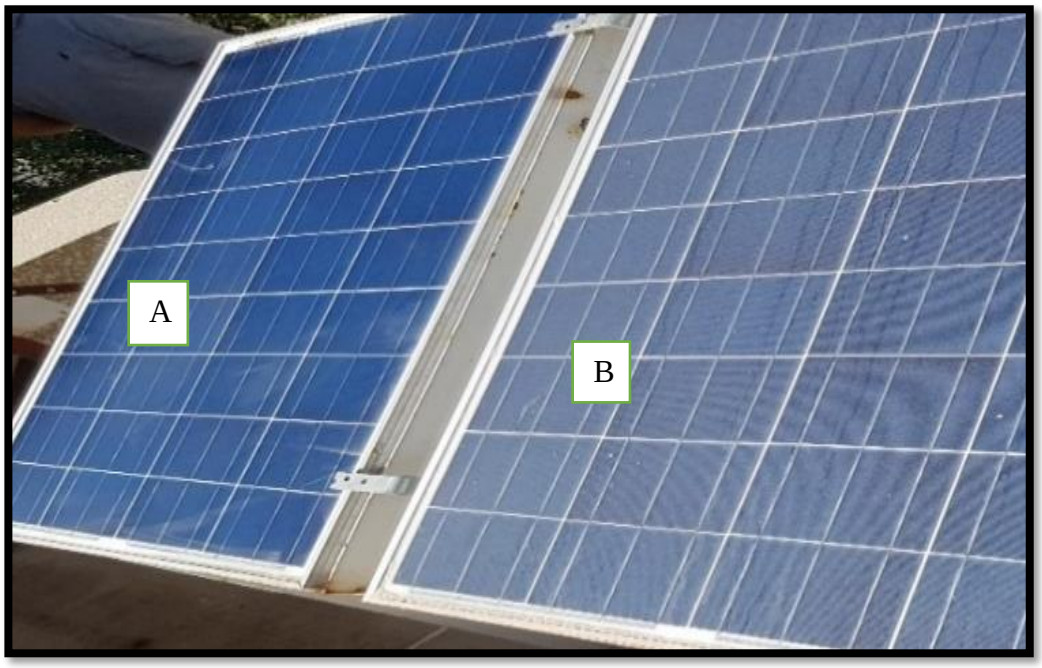


Figure 6.2: (A) Cleaned PV module v. (B) dusty PV module.

The two PV modules used in this experiment have the same manufacturer, Simax Green New Energy (Europe) GmbH, Model No. SQP636- 100. The rated maximum-power output for both was 100 W, their expected V_{OC} was 21.8 V, and 6.14 A was rated for the I_{SC}. They were both tilted horizontally at an angle of 23º.

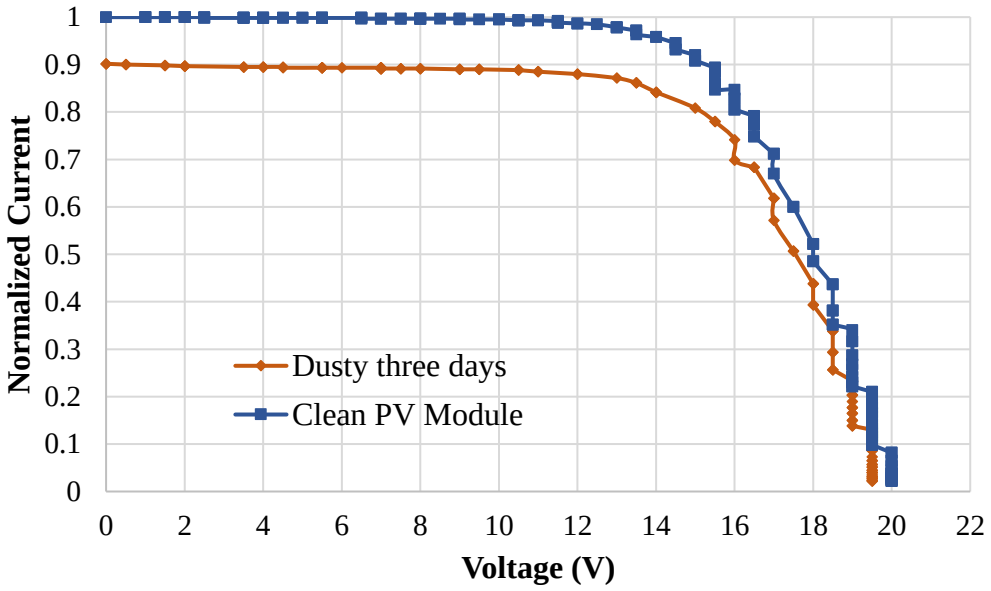


Figure 6.3 I-V curve of the dusty module versus the I-V curve of the cleaned PV module surface. Y-axis is the current normalized to 1.0 A.

First, both modules were measured when cleaned to confirm their electrical performance was similar. Then, one module was left to accumulate dust for three days while the other cleaned regularly. Measurements were taken from both modules, cleaned and non-cleaned, twice: in two days and three days. Figure 6.2 shows the two PV modules, one accumulated dust for two days.

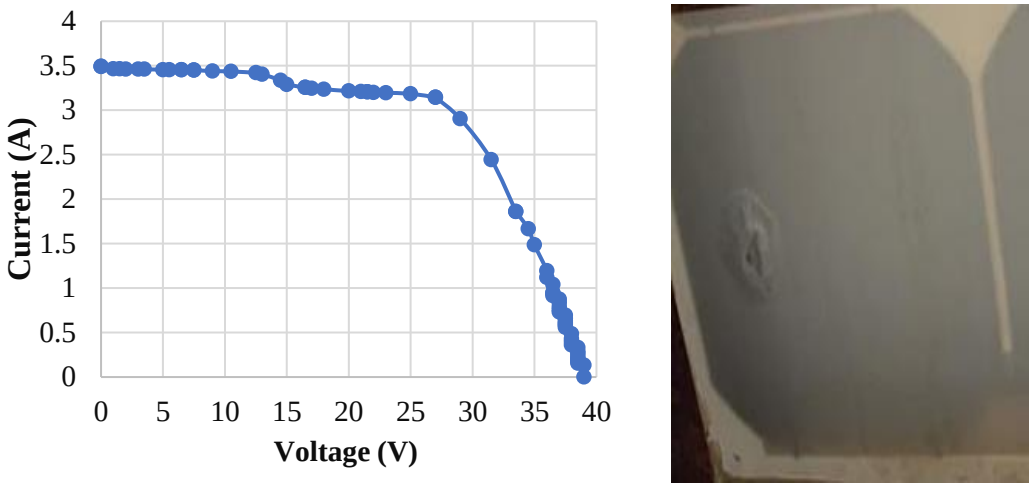
Considering the dusty weather in Dhahran, within two days, the I_{SC} of the dusty PV module was lower by 5.5% at 5.37 A than the cleaned PV module, which was

5.68 A. The measurements were taken at a tilted global irradiance of 850 W m^{-2}. Eppley Radiometer, Model. PSP was used for irradiance measurements. Other measurements were taken at tilted global irradiance ranging between 462-475 W m^{-2} on the next day, the reduction of I_{SC} became 4.5% lower in the dusty PV module; it was 2.7 A while the cleaned module was 3.0 A.

The difference in the maximum-power output was also evident in both cases; the P_{max} in the cleaned PV module was 9.7% higher at 68.1 W, while the dusty module was 62.1 W at two days of dust accumulation. The gap increases in the three-day accumulation; the cleaned PV module produced 13% higher energy than the dusty one. The cleaned PV module produced 41.8 W whereas the dusty produced 36.0 W. Figure 6.3 shows the difference between the *I-V* curves of cleaned PV modules and the dusty PV module. This result agreed with Zaihidee *et al.* [134] and Saidan *et al.* [135], the longer the dust accumulates on the PV surface, the more the reduction in the short-circuit current and the power output.

6.2.2 PV Module Diagnosed with Hotspot Failure

At the same location in KFUPM, a mono-crystalline module was deployed and tilted at the same angle, 23º. The module's P_{max} was rated at 150 W, its rated V_{OC} was 43.2 V. The short-circuit current was rated at 4.49 A. One of the PV module's cells was damaged due to hotspot heating, as seen in Figure 6.4. The *I-V* curve measurements at an irradiance of 740 Wm^{-2} were taken using the same measurement technique applied for the dusty experiment.



(A) (B)

Figure 6.4 (A) I-V curve of PV module with one cell damaged by hotspot. (B) snapshot of hotspot damage

The *I-V* curve indicated a normal operation until reaching almost 15.0 V, where the PV string containing the damaged cell was located. Once it reached the hotspot's string, the current was reduced by 8 to 9% until reaching the P_{max} point, causing a jump-down in the curve. The *I-V* curve also indicated a reduction in fill factor and the open-circuit voltage was less than rated. Unlike shading caused by dust accumulation, which can be fixed by removing the shading object, the damaged solar cell caused by the hotspot resulted in a permanent reduction of the I_{SC} and fill factor and cannot be reversed.

6.3 Corrective Actions and Potential of Machine Learning Models

Corrective action dealing with degraded PV modules depends on the failure type and whether the module can be fixed. From the KFUPM experiments, shading

failures are usually temporary and can be fixed by removing the shading object. From Han *et al.* [31], failures related to the j-box were fixed by replacing the failed j-box. On the other hand, the hotspot failure may cause permanent damage to the module. PV modules with permanent loss, like a hotspot or a high degradation rate, cannot be fixed, and therefore they can only be replaced as a corrective action.

However, module replacement depends on several factors, climate, cause of degradation, and type of PV system. A survey study by Köntges *et al.* [115] found that the mean degradation rate for PID failure was 15% per year. Therefore, early detection of this degradation may protect the PV array from a substantial power loss.

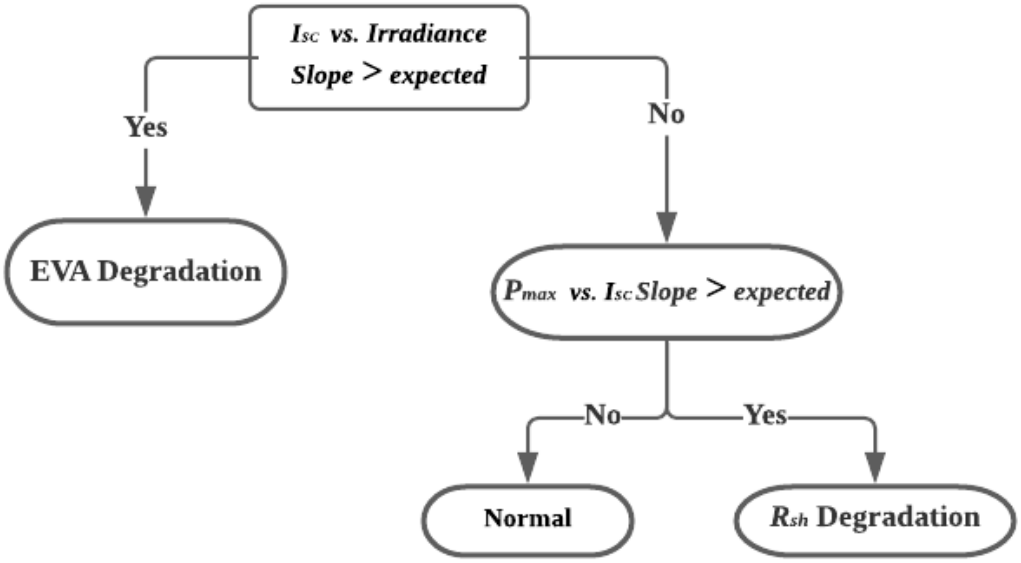


Figure 6.5 Decision tree model classifies between EVA and R_{sh} degradation mechanisms.

Furthermore, monitoring systems in PV plants apply machine learning models nowadays [242]. The *I-V* parameters and solar irradiance are stored through

a data acquisition system. The stored data can train and test a simple classification ML model to classify reversible failures, such as shading, from irreversible failures, such as a module damaged by a hotspot.

Hence, this dissertation develops novel models to detect EVA and shunt resistance degradations, where EVA reduces $I_{sc,}$ and shunt resistance reduces both V_{OC} and P_{max}. The distinction between the two degradations can be precisely obtained by training a machine learning model, even with employing P_{max} only. This is because machine learning models can classify using the P_{max} reduction range when provided with sufficient data. Figure 6.5 demonstrates an example diagram of a decision tree classifier (DTC) that can be applied conveniently, classifying EVA degradation from R_{sh} degradation.

As an illustration, small-scale data that contains 334-inputs of slope values were generated to be implemented in a machine learning, decision tree model. The slopes were calculated from seven irradiance points; the points were 942.3 W m^{-2}, 879.8 W m^{-2}, 746.6 W m^{-2}, 702.3 W m^{-2}, 657.9 W m^{2}, 588.4 W m^{-2}, and 544.4 W m^{-2}. In the EVA degradation, the I_{sc} versus irradiance slope increased by roughly 4.8% from 0.00398 to 0.00418 A W^{-1} m^{-1}. That is before EVA turned yellow, whereas, in the shunt resistance degradation, the P_{max} versus I_{sc} slope increased by 37% from 0.485 to 0.787 W A^{-1}. That is when the natural R_{sh} decreased up to 519 Ω cm^{2}. In other words, the slope represented EVA indicated a healthy operation until reaching 0.00418 A W^{-1} m^{-1}, and the slope represented shunt resistance indicated a normal operation until reaching 0.787 W A^{-1}.

The ML model was derived from the sci-kit-learn library in Python. The model also used NumPy, Pandas, and Matplotlib libraries to import, display, visualise and

plot the data. In a decision tree model, the first split, described as the root node, is determined by the Gini-impurity; a mathematical analysis to find the ideal split among all feature inputs. The feature input with the lowest Gini-impurity is selected as the root node, and then the splits continue on this basis until reaching the last node known as the leaf node.

The 334-input data were separated into three categories and supplied to the ML model. The three categories were:

- One represented a healthy operation of the PV module and contained different healthy values of slopes representing EVA and shunt resistance. To obtain healthy values, the slope represented EVA and shunt resistance was increased slightly until their threshold points, 0.00404 A W^{-1} m^{-1}, and 0.787 W A^{-1}, respectively.
- The second category represented a degradation mode of EVA and is determined when the slope representing EVA is 0.00418 or higher.
- The third category represented a degradation mode of R_{sh} and is determined when the slope representing R_{sh} is 0.785 or higher.

About 34, 10% of the feature inputs were arbitrary numbers inserted to test the ML model's accuracy in classifying each category.

Figure 6.6 shows the DTC model in Python, demonstrating the split and the decision boundaries of the model. It can be noticed that the DTC model suggested by Python is different from the proposed one in Figure 6.5. As explained earlier, the ML model decision boundaries are based on the Gini-impurity calculated from the fed data, i.e., the DTC model has considered the slope represented shunt resistance as the root node as its Gini-impurity was the lowest. The value of

0.765 W A^{-1} was determined to split and determine the shunt resistance degradation as most healthy inputs were below this value. If the R_{sh} slope is lower, further analysis for EVA degradation was computed. Then, if the slope of the EVA degradation was higher than 0.004 A W^{-1} m^{-1}, the model indicated a degradation mode in EVA, else the PV module is running in healthy operation. The suggested ML model was straightforward and 96% accurate when validated.

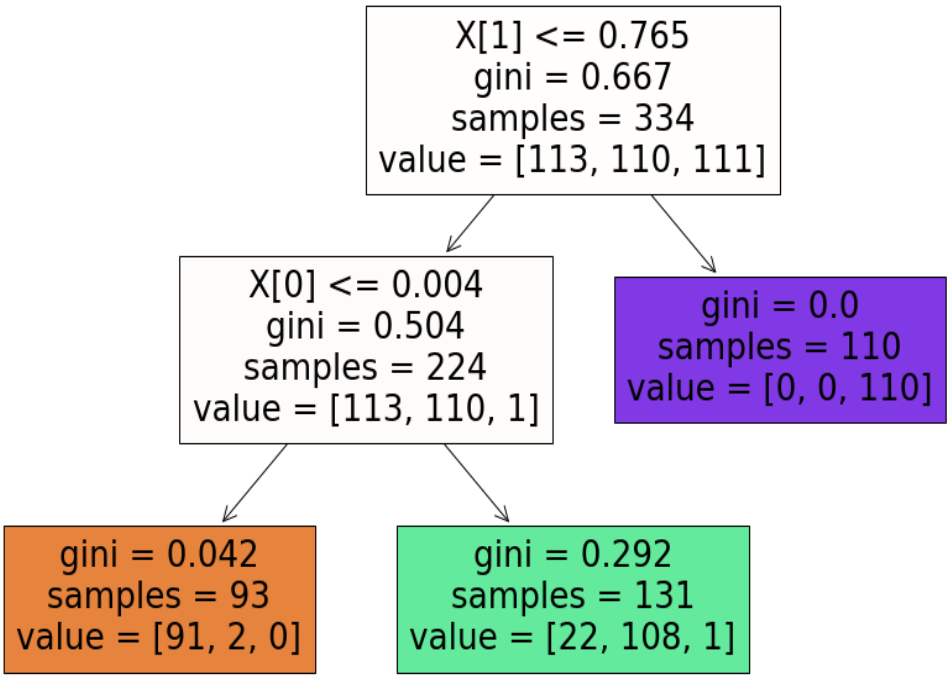


Figure 6.6 Decision tree ML model for small-scale data used to predict, detect and classify shunt resistance and EVA degradations of PV module. X [1] is the slope used to detect shunt resistance degradation, and X [0] is the slope used to detect EVA degradation.

Sometimes, a temporary shading is caused by an object, which will reduce P_{max} and I_{sc} simultaneously and increase EVA and R_{sh} slopes. Depending on the

irradiance level, the slope will be affected differently. For example, shading of up to 60 % above 700 W m^{-2} won't increase the slope to the threshold point. However, if the shading is below 700 W m^{-2}, the slopes increase significantly, specifically for EVA. This may be influencing the results and substantially decrease the DTC model's accuracy, although some arbitrary slope values were introduced in the data.

In this scenario, two solutions can be proposed to optimise the DTC model; the first is to take the average slopes from two consecutive days. A drawback of this solution is a delay in corrective actions when dealing with hazardous failures. The second solution is to add more attributes and targets to the DTC model to differentiate between temporal shadings scenarios, EVA, and shunt resistance degradations. The latter is safer and is convenient to apply.

6.4 Conclusion

Corrective actions to be taken with PV failures depend on whether the failure can be reversed or not. This chapter showed that the experimented module affected by dust accumulation can be mitigated by appropriate and regular cleaning. Whereas the one affected by hotspot cannot be reversed. It also indicated that early detection of some reversible failures like extreme shading prevents the failure from becoming irreversible. Machine learning model (decision tree) was shown useful to be trained to classify between these failures. Table 6-1 compares a widely-cited article that used a decision tree ML model approach and the approach followed in this chapter.

Table 6-1 Comparison between decision tree ML model used by widely-cited article and the one followed in this chapter.

Scientific Articles versus Existing Work	**DTC ML Model Purpose**
Zhao *et al*. [243].	A large data set (over 700k) was used to train a decision tree ML model to classify four types of PV failures: solid line to line, solid line to line with low impedance, open circuit, and partial shading failures. The ML model has an accuracy of 99%.
Existing Work	A small data set was generated from SPICE simulation based on experimental results to classify two degradation mechanisms of PV (EVA and shunt resistance). The ML model has an accuracy of 96%.

In terms of irreversible degradations, only replacement of that failed module can be taken as a corrective action to restore maximal power. This is also applied to EVA and shunt resistance degradations investigated in Chapters 3-5. However, in the case of EVA and shunt resistance degradations, the optimal time to proceed with PV module replacement in a cost-effective way needs to be analysed. Hence, this dissertation accurately identified the shunt resistances and EVA degradations and their corresponding output power. Modelling and simulation of the expected power loss can be used for further economic analysis to determine the optimal time. In the next chapter, cost analysis to find the optimal time to replace a PV module affected by irreversible degradations caused by EVA discolouration and low shunt resistance will be demonstrated.

7 Chapter 7| Cost Analysis for Substituting a Degraded PV Module as A Corrective Action

Chapters 3-5 introduced simulations and experiments to develop models to predict and detect PV degradations at the early onset. Chapter 6 showed an example that some degradations are temporary others are permanent and cannot be reversed. If they are permanent, replacement of the module is recommended, particularly in PV arrar or PV string system as the degraded module will drag down the PV system's power generation. However, the replacement of the degraded PV module must be cost-effective. Thus, this thesis ends with a cost analysis to discover the optimal replacement time for a PV module degraded by either low shunt resistance or EVA discolouration.

7.1 Introduction

In the previous chapter, corrective actions were discussed; replacement is advised if the PV module is damaged. In some cases, however, the damage is mild and does not lead to dangerous consequences or a significant power loss. Chapters 3 and 4 have addressed the effect of PV failures due to EVA degradation (optical) and shunt resistance degradation primarily (electrical).

This chapter presents an economic analysis to determine if replacing an irreversibly degraded PV module, EVA discolouration and low shunt resistance in particular, before causing hazards in a string or array system is cost-effective. Section 7.3 expands the investigations of a degraded PV module to PV string and

array systems via SPICE and mathematical calculations. Once these investigations address the effects on the electrical parameters, Section 7.4 estimates the energy production from a healthy PV system and a system containing a degraded PV module. Based on Ireland's PV market, the cost of a PV system (string or array) with a degraded PV module versus the cost of replacement is compared in Section 7.6. This likely helps in identifying the optimal time to replace a degraded PV module in array or string systems.

7.2 Cost Analysis for Substituting a Degraded PV Module

Positive impacts of the growing ratio of renewable energy over conventional energy on the environment have been studied and highlighted extensively (Refer to Chapters 1 and 5). However, the variability of generation and cost-effectiveness leads to hesitancy in proceeding with more deployments of renewable energy systems. In terms of the latter, it has been claimed by Quaschning [244] that although conventional energy systems may seem more cost-effective than renewable energy systems, they are highly affected by uncertainty due to environmental and political variables. For instance, the oil crisis that took place in 1970 led to a dramatic surge in energy prices. Alternatively, cost-effectiveness related to renewable energy, such as solar and wind, is unlikely to be influenced by such variables [244].

However, this is not always the case as failure or critical degradation, which may arise in any operational year of the PV system, will also create uncertainty about cost. It was demonstrated from the introductory chapter that PV failures and degradations, if undetected, cause a significant power loss and lead to catastrophic

consequences. Even so, the only cost will be taken into consideration when proceeding with replacement as a corrective action.

When it comes to the cost evaluation for EVA or shunt resistance degradations in the PV systems, the subsequent steps are followed to address the issue accurately:

Step 1: Effects of EVA and shunt resistance degradations in PV string and array systems are analysed and compared: SPICE simulation is used to assist in the analysis. The generated power as well as the energy production from two PV systems of the same rating, one of which has a degraded module affected by either EVA or R_{sh} defect, are compared.

Step 2: Finding the installation cost and the expected energy production from the PV system. The Sustainable Energy Authority of Ireland (SEAI) has evaluated the cost and energy production from PV systems in Ireland.

Step 3: Referring to the approach and mathematical models provided by Quaschning [244], the cost for a PV string and array with and without replacement of degraded module are calculated and compared.

7.3 Simulation of PV Array and String to Extract Parameters

Simulation of PV string and PV arrays using SPICE requires a very high number of nodes. Castaner and Silvestre [5] provided the following approach for PV string and array simulations:

- Firstly, the PV solar cell was scaled to a PV module. This is achieved by scaling up the current, voltage, and series resistance of the *I-V* equation of the solar cell to a PV module *I-V* equation.

- Secondly, the electrical parameters from the PV module were inserted into SPICE circuit code with the preferred number of nodes. In other words, apply the same technique to simulate PV module by increasing the number of nodes of solar cells (Refer to Chapters 5) but, this time, increasing the number of nodes for PV module.

Scaling PV cell to module neglects the effect of shunt resistance. The second saturation current and the photogenerated currents (I_{ph}) are regarded as the short-circuit current as seen from Eq. (7.1) [5].

$$I = I_{sc} - I_0\left(e^{\frac{V+IR_S}{nV_T}} - 1\right) \tag{7.1}$$

Scaling the short-circuit current in a PV module increases the number of cells connected in parallel (N_p), whereas scaling the open-circuit voltage increases the number of cells connected in series (N_s) as seen from Eq. (7.2-7.3) [5].

$$I_{scM} = N_p I_{sc} \tag{7.2}$$

$$V_{ocM} = N_s V_{oc} \tag{7.3}$$

Where V_{ocM} and I_{scM} are the module's open-circuit voltage and the short-circuit current, respectively. Substituting parameters from Eq. (5.1) with parameters from Eq. (7.1) formulates the *I-V* curve equation for the PV module as seen from Eq. (7.4) [5].

$$I_M = I_{scM}\left(1 - e^{\frac{V_M + I_M R_{SM} - V_{\mathrm{ocM}}}{nV_T N_S}}\right) \tag{7.4}$$

Series resistance can be obtained and calculated by correlating its effect on the fill factor as seen in Eq. (7.5) [5].

$$R_{sM} = \frac{V_{ocM}}{I_{scM}} - \frac{P_{maxM}}{FF_{OM} I_{scM}^2} \tag{7.5}$$

The Equations (7.4-7.5) are inserted in a SPICE netlist. The values of I_{SCM}, V_{OCM}, maximum output power (P_{maxM}), and the number of cells in parallel and series can be inserted in SPICE code to simulate the expected *I-V* curve of a PV module.

Although SPICE code did not consider the shunt resistance, the effect of shunt resistance was investigated in Chapter 4 and found to cause a reduction in P_{max} and V_{OC}. Thus, reduced percentages of P_{max} and V_{OC} from their initial values were quantified and used to calculate the shunt resistance effect on a PV module; this is explained further in Section 7.5.3.

7.3.1 Extracting Parameters from Simulated PV Module

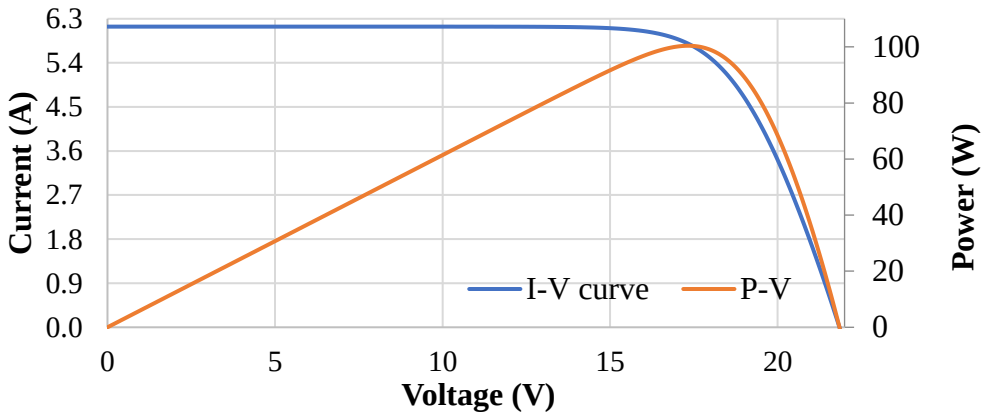


Figure 7.1 I-V and P-V curve of PV 100 W PV module.

A PV module with electrical characteristics close to the ones found in the real-world is simulated using SPICE. The simulated *I-V* characteristic of the module has 6.14 A as short circuit-current, an open-circuit voltage of 21.8 V and a maximum current of 5.80 A, maximum voltage of 17.24 V, producing roughly a maximum-power output of 99.3 W. Figure 7.1 shows the generated *I-V* and power curve from SPICE simulations.

7.4 Estimated Energy from PV Systems in Ireland

Table 7-1 Estimated yearly energy production in Ireland for a PV string with five peak power ratings facing south tilted at 60º angle, at three different scenarios, (1)Without extreme degradation, (2) One module with EVA yellow-brown degradation, and (3) One module with shunt resistance degradation at 113.1 Ω cm^2.

Peak power of PV string (kW)	**Estimated annual energy (kWh)**	**Estimated annual energy subjected to EVA degradation (kWh)**	**Estimated annual energy subjected to R_{sh} degradation (kWh)**
0.6	493.0	455.2	455.2
1.2	986.0	910.3	925.9
1.8	1478.9	1365.5	1397.5
2.4	1971.8	1820.7	2026.1
3	2464.0	2275.8	2340.7

After simulating the *I-V* curve characteristics using SPICE, the energy produced by a PV string that consists of six modules in Ireland for one year can be anticipated by referring to the National Standards Authority of Ireland) (NSAI) [245]. It was stated that energy produced from a PV system in kilo-Watt-hours (kWh) could be estimated using Eq. (7.6) [245].

$$\text{Energy from the PV system (kWh)} = 0.8 \times \text{kW}_p \times S \times Z_{pv} \qquad (7.6)$$

Where 0.8 refers to the performance ratio determined by several variables such as thermal and cable losses. kW_p is the peak power or maximum power output of the system. S is the annual solar radiation in kWh. Z_{pv} refers to the overshading factor; which equals one in clear sky condition and 0.5 in heavy shading. The annual solar radiation for different tilt angles was given by Dwelling Energy Assessment Procedure (DEAP) software, software offered by SEAI [201] to estimate energy production.

For example, the annual solar radiation for PV string facing south and tilted in 60º is 1027 kWh. Substituting this value in Eq. (7.6) [245] for a PV string with peak power of 600 W, the energy production will be *c.* 493 kWh annually in clear sky condition, and for a 6×5 array system, the estimated energy production will be *c.* 2464 kWh.

Based on these results, Tables 7-1 and 7-2 show the estimated energy production for five array and string systems with different peak power.

Table 7-2 Estimated yearly energy production in Ireland for PV array with five peak power rating facing south tilted at 60⁰ angle at three different scenarios, (1) Without extreme degradation, (2) One module with EVA yellow-brown degradation, and (3) One module with shunt resistance degradation at 113.1 Ω cm².

PV System Peak Power (kW)	**Estimated annual energy (kWh)**	**Estimated annual energy subject to EVA degradation (kWh)**	**Estimated annual energy subject to R_{sh} degradation (kWh)**
6×5 array = 3	2465	2424.5	2358.0
6×10 array = 6	4929.6	4887.7	4736.5
6×20 array = 12	9859.2	9813.2	9495.2
6×40 array = 24	19718.4	19660.9	19011.8
6×80 array = 48	39436.8	39354.6	38044.2

7.5 Energy Loss from PV Systems with a Degraded Module

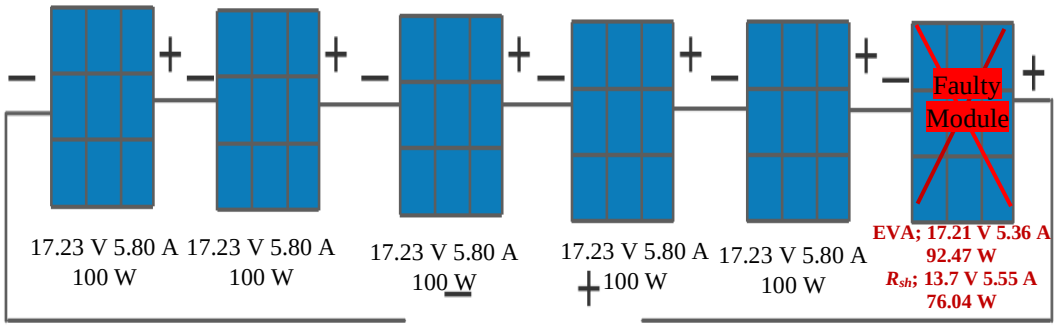


Figure 7.2 Diagram demonstrates the V_m, I_m, and P_{max} parameters of a PV-string consisting of 6 PV modules connected in series, one of which shows the parameters of a degraded module by yellow-brown EVA or by low shunt resistance at 113.1 Ω cm².

To quantify the EVA degradation effect on PV string and array systems: Firstly, as EVA degradation decreased P_{max} and I_{SC}, the lost percentage in P_{max} and I_{SC} from their initial values of the solar cell (Refer to Chapter 3) is multiplied by the P_{max} and I_{SC} of the PV module. Secondly, the calculated P_{max} and I_{sc} of the degraded module are inserted in SPICE to simulate the expected *I-V* curve. Thirdly, from the simulated *I-V* curve, I_m, V_m and P_{max} of the degraded module can be extracted to investigate its effect when existing in PV string or array systems.

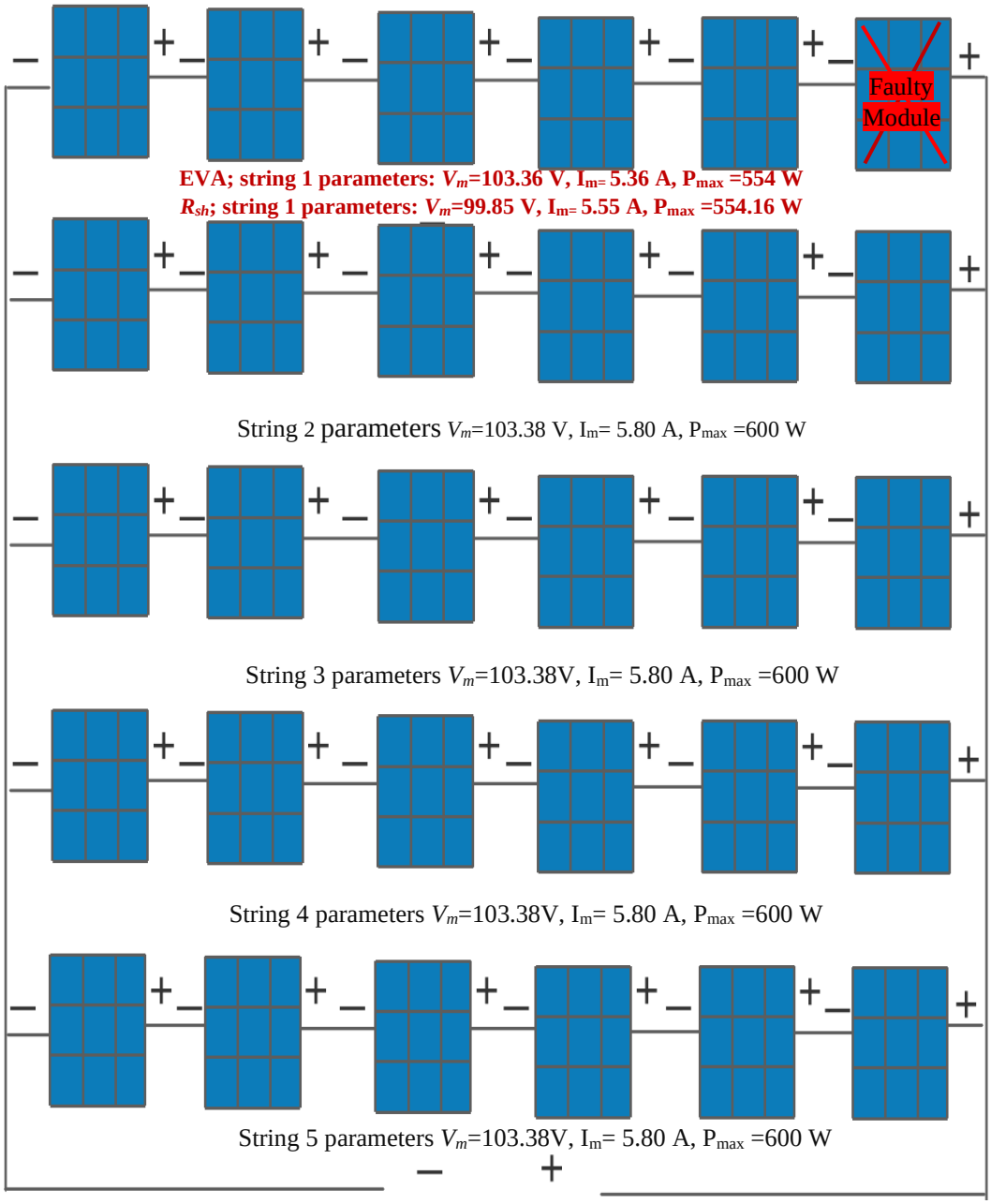


Figure 7.3 Diagram demonstrates the V_m, I_m, and P_{max} of a 6×5 array, one of which shows the parameters of a degraded module by EVA or by shunt resistance at 113.1 Ω cm^2.

Low shunt resistance of the solar cells reduces P_{max} and V_{OC} (Refer to Chapter 4). Thus, the effect of the shunt resistance degradation on PV string and array systems can be obtained by following the same way of quantifying the EVA effect, but for P_{max} and V_{OC}. After, simulating the *I-V* curve of the degraded module with low shunt resistance, I_m, V_m and P_{max} can be extracted to investigate its effect when existing in PV string or array systems. Further calculations are demonstrated to estimate the energy loss due to EVA and shunt resistance degradation in Sections 7.5.1 to 7.5.3.

7.5.1 PV String with a Module Showing Yellow-Brown EVA

A reduction in the maximum current of one module connected in a string affects the whole string power output. This is because the I_m of the string is determined by the lowest I_m among all PV modules, whereas the V_m of the string is the modules' maximum voltages added altogether [246].

After simulating the *I-V* curve of the affected module by EVA discolouration via SPICE, its I_m, when extracted, was reduced by 7.59%. Maximum voltage was also reduced slightly. Figure 7.2 shows V_m and I_m values for each module of 6-module- string.

In this scenario, the peak power of the 6-module's string reduces to 553.42 W, a 7.67% lower than the rated value. The reduction in P_{max} percentage for the PV strings listed in Table 7-1, when containing a module with yellow EVA discolouration, was also 7.67%. This is because the module with the lowest current in a string, as in EVA degradation scenarios, determines the string current as explained earlier, i.e., given that the decreased current of yellow EVA causes a

reduction in the 6-module-string's P_{max} by 7.76%, it will also reduce the P_{max} of a 30-module string by the same percentage.

7.5.2 PV Array with a Module Showing Yellow-Brown EVA

When the EVA discolouration occurs in a PV array, the loss in maximum power becomes smaller; the maximum voltage of the array is determined by the lowest string's $V_{m,}$ whereas the maximum current of the array is the sum of the strings I_m.

For example, Figure 7.3 shows a 6×5 PV array system with specified parameters for each string. Based on this setting, the peak power of the array system becomes 2951 W, a 1.63% lower than rated, reducing the energy production in Table 7-2, the EVA case, by 1.63%. It can be concluded that in the case of the EVA degradation, the lost power percentage becomes less when the number of strings increases in the array system.

7.5.3 PV Systems with a Module Degraded by Low Shunt Resistance

Following the same steps in Sections 7.5.1 and 7.5.2 but for the shunt resistance's degradation settings, the P_{max} and V_{OC} of the affected PV module are inserted into SPICE code to simulate the *I-V* curve and extracted V_m and I_m. The level selected for the degraded shunt resistance was before reaching the critical point at 113.1 Ω cm^2. The average reduction in P_{max} and V_{OC} from the five cells' samples investigated in Chapter 4 were 24.4% and 6.4%, respectively. As a result, the output V_m and I_m at P_{max} were 13.7 V and 5.55 A.

Based on this setting, the peak power of the 6-modules string shown in Figure 7.2 will be *c.* 554 W, 7.63% lower than the rated power, whereas if the module exists in a 6×5 array, the output power will be 4.34% lower than the rated. These percentages will be reflected in the annual energy production of the system. As the effect of low shunt resistance reduces the module's voltage, the loss percentage in both string and array systems will become smaller when they contain a higher number of modules connected in series.

7.6 Optimal Time for Replacement of Degraded Module

According to Quaschning [244], the cost for a renewable energy system with a return on capital can be calculated by considering the interest rate (ir) and annuity factor. Return on capital typically refers to investment and profiting from installation costs in the long run. The interest rate is determined by the financial institution that offers the debt and is usually depending on the risk factors associated with renewable energy such as deficiency of renewable resources. The method calculated the cost in € per kWh.

To estimate the cost of the renewable energy system; firstly, the total cost (C_{tot}), investment cost or installation cost in the commence year (A_0), and maintenance cost in the year of maintenance (A_i) is calculated using Eq.(7.7) [244].

$$C_{\text{tot}} = A_0 + A_i \tag{7.7}$$

The compound interest rate, also known as the discounted rate, is added to the equation to be:

$$c_{\text{n}} = A_0 \cdot (1 + ir)^{\text{n}} = A_0 \cdot q^{\text{n}} \tag{7.8}$$

Where n is the number of the investment years (the lifecycle of the PV system), 1 is the initial capital (A_0) given by the financial institute plus the interest rate and referred to as q. If an additional payment A_i is added to the capital in a specific year (n), the interest rate change and A_i is calculated from Eq. (7.9) [244];

$$A_i = A_i \cdot q^{-i} \tag{7.9}$$

Taking into consideration the annuity factor, which can be calculated as seen from Eq. (7.10) [244].

$$a = \frac{q-1}{1-q^{-n}} \tag{7.10}$$

Then, with return on capital, Eq. (7.7) becomes Eq. (7.11) [244]

$$c_0 = A_0 + A_i \times \frac{q^n - 1}{(q-1) \cdot q^n} \tag{7.11}$$

The cost of the system in kWh (c_E) can be estimated by dividing the annual cost (C_a), which is the product of the annuity factor and the discounted capital (c_0), from the generated energy (E_a) per year as seen from Eq. (7.12) [244].

$$c_E = \frac{c_0 \times a}{E_\mathrm{a}} \tag{7.12}$$

7.6.1 Cost of 3- kW and 6-kW PV Systems in Ireland

According to the SEAI's Frequently Asked Question document [247], the average cost of PV grid-connected system installation in Ireland is € 1750 per kW, which is close to the survey done by Monaca and Ryan [248]. The breakdown of the PV system cost can be taken from [244] and it depends on the size of the

system. For instance, for 1 kW system; PV modules accounts for 48%, inverter for 13%, material for 17%, labour for 15% and 7% for documentation. For systems larger than 1 kW, the PV module's portion increases to 55%, while material, labour, and documentations decrease to 16%, 11%, and 5%, respectively.

Table 7-3 Calculated costs for 3 kW PV string and 6 kW PV array.

Type of system	**10-module string (3 kW)**	**6×10 array (6 kW)**
Installation cost (€)	6155.7	11405
Annuity factor $\boldsymbol{a}$	0.0710	0.0710
annual energy $\boldsymbol{E_a}$ **(kWh)**	2465	4929.6
Cost $\boldsymbol{c_E}$ **(€ /kWh)**	0.177	0.164

For a residential 3 kW PV system in Ireland, the installation cost (A_0) will be *c.* € 5250 [247]. The inverter needs to be changed after ten years, its estimated cost is *c.* € 1475.33 [248]. E_a annual energy production from a 3- and 6-kW PV system can be taken from Table 7-1 and 7-2. The interest rate was assumed to be 5% based on a cost study in Ireland by Ayompe *et al.* [249]. After having the necessary values estimated, the cost with return on capital can be calculated from Eq. (7.7-7.10) [244]. Table 7-3 shows the estimated cost for two PV systems; 3 kW and 6 kW.

7.6.2 Cost Comparisons for Replacement of Degraded PV Module

To compare the cost of a system operated with a degraded module and the cost of that system when this module is replaced, the following points need to be noted:

A) The cost of module replacement is added to Eq. (7.8). The cost of replacing a degraded PV module depends on the manufacturer's and maintenance companies' prices, but it can be calculated from the installation cost breakdown. PV modules account for 55%, understanding that the system consists of 30 modules, at 100 W each, the cost of one module will be roughly € 97. The labour cost for replacing a module is approximately € 222 on average. Therefore, the replacement cost of a degraded module will be *c.* € 319 [250].

B) E_a , the annual generated energy needed to be evaluated for the two systems: one operated with a degraded module, the other with a replaced PV module.

C) It must be noted that the cost is highly affected by time; therefore, the cost for four different times was calculated; a PV system with module degraded in year 5, year 10, year 15, and year 20 of operation. That means, if the system is operating at maximal power production in the first four years, and then one module degraded in the fifth year, the cost of the first four years should be calculated separately from the next twenty-one years and the lifetime cost for the 25 years is estimated.

Taking these points into consideration results are presented in Figures 7.4 and 7.5. In Figure 7.4, replacing a degraded module, with either EVA discolouration or low shunt resistance, in a 3-kW rated PV-string is more cost-effective, except if the replacement of the degraded module with low shunt resistance proceeded in year 20**.**

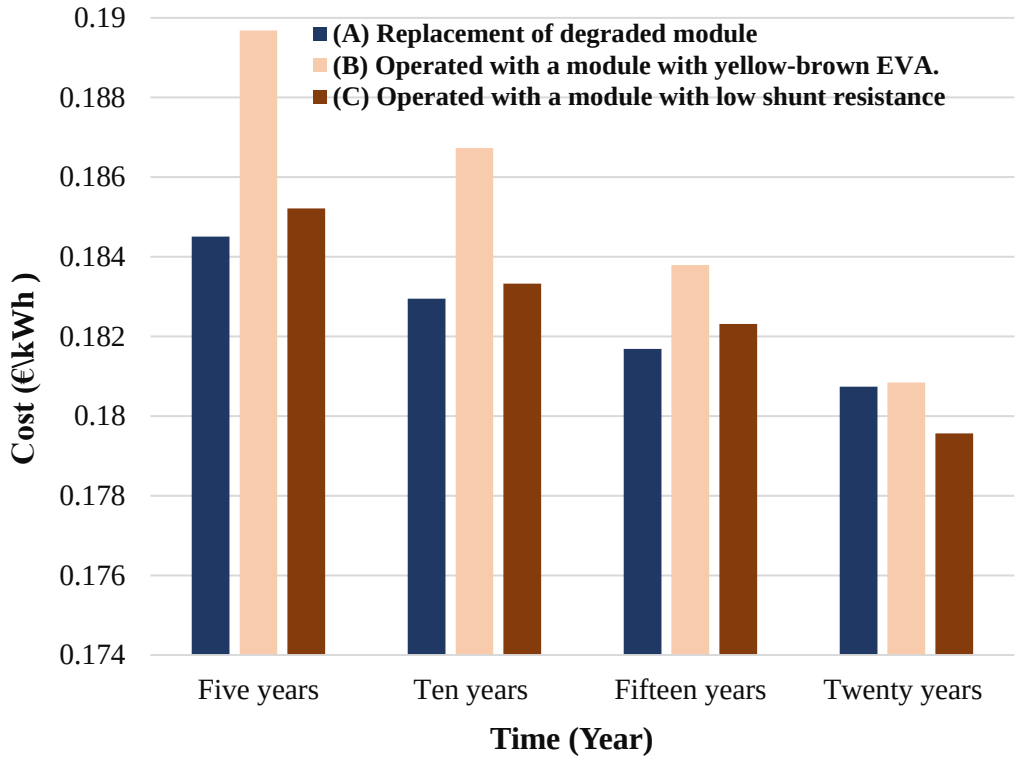


Figure 7.4 Estimated cost for a PV string consisting of 10 modules at four different times of degradation. Where: (A) Estimated cost when replacing an irreversibly degraded module in the system, (B) Estimated cost of the PV system when one module is degraded by yellow-brown EVA, (C) Estimated cost of the PV system when one module is degraded by low R_{sh} at 113.1 Ω cm^2.

However, replacing the degraded module with EVA at twenty years was almost similar to keeping it running in the system. Also, it is more costly to replace a

degraded module with low shunt resistance in the same year. However, risk management associated with keeping a faulty module in the system is required to make the right decision. For example, disconnecting solar bonding may lead to safety concerns in the worst-case scenario.

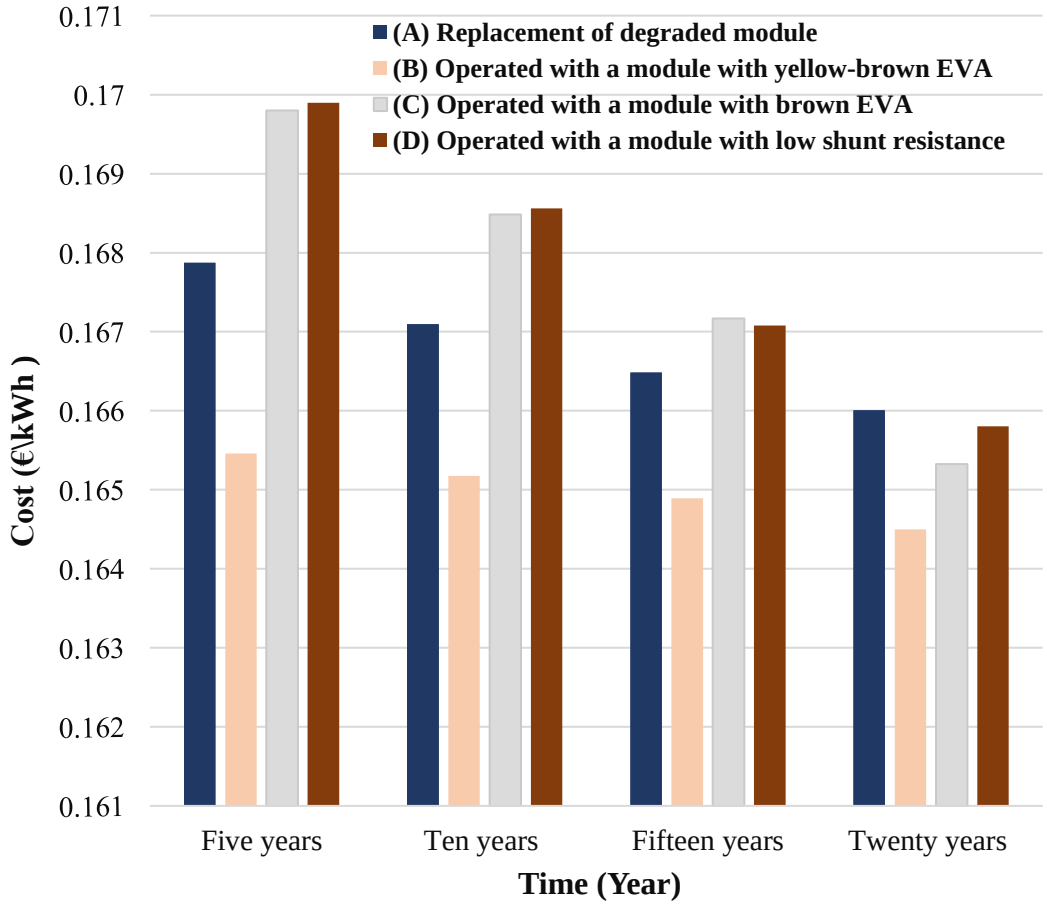


Figure 7.5 Estimated cost for a PV 6×10 array system at four different times of degradations. Where: (A) Estimated cost when replacing an irreversibly degraded module in the system, (B) Estimated cost of the PV system when one module degraded by yellow-brown EVA, (C) Estimated cost of the PV system when one module degraded by brown EVA, (D) Estimated cost of the PV system when one module degraded by low R_{sh} at 113.1 Ω cm^2.

Figure 7.5 shows the cost of replacing a degraded module in the 6×10 array system. It can be noticed that replacement cost in PV array system is higher when compared to a string system. This is because the effect of a degraded module in the array system becomes less severe, which makes the optimal time for replacing a degraded EVA module when the EVA turned to brown.

The cost for swapping a yellow-brown EVA in this scenario is higher. Once more, risk management is needed to ensure the failure is mild, exploring if the only cause for yellowing was UV light exposure, rather than other hazardous failure mechanisms that may lead to catastrophic progressive failure in the system. On the other hand, swapping a module with low shunt resistance at 113.1 Ω cm^2 is more cost-effective at all times except at or after 20 years of the system age.

7.7 Conclusion

The cost of replacing a degraded module with 113.1 Ω cm^2 shunt resistance was analyzed. Results have shown that it is more cost-effective to replace a degraded PV module in PV array and string systems unless the replacement will be at the end of the PV module lifecycle, specifically, in year 20 or more of the system lifetime. Replacing a PV module with mild discolouration of EVA, particularly yellow-brown, seems to be costly in the array system.

However, when it comes to cost analysis, several factors should be taken into consideration:

a) The setting of PV string and array, meaning the number of modules in a string or array. The cost analysis in this chapter considers one setting for each.

b) The normal degradation rate is 0.8% per annum, this was not counted when performing the analysis, i.e., the analysis was based on a single module that experienced a higher degradation rate than others or failure.

c) It might be argued that replacing a module that started to show critical degradation symptoms will lead to mismatch failure. In fact, it is otherwise, i.e., retaining such a module in the system will lead to a mismatch [62].

The replacement cost of a PV module before becoming critical in a PV string or an array system was not commonly analyzed in the literature. There is, nevertheless, a study by Orkizis [251] that showed the replacement of one PV module affected by a short-circuit failure in a (37×25 array system, 180 W each), is cost the same as keeping it in place. Table 7-4 compares key findings from Orkizis [251] and the results realized in this chapter.

Table 7-4 Comparison between the cost analysis used in Orkizis [251] and the one followed in this chapter.

Scientific Articles versus Existing Work	Approach Used
Orkizis [251]	Evaluated the effect of a PV module with an open circuit or short circuit failure in an array system, where the failed PV module produces no power. The results agreed with the findings in this chapter in which the setting of the array significantly characterises the power output, hence, affecting the cost. The cost analysis was based in Italy.
Existing Work	Evaluated the effect of a PV module suffering from either EVA discolouration or low shunt resistance in different settings of PV string and arrays, where the failed PV module still produce power. The replacement cost in one PV string and one array setting was compared based in Ireland.

8 Chapter 8| Conclusions, Summary and Outlook

The thesis conclusion is divided into three parts: contributions, summary, and proposal of future works.

8.1 Contributions

The dissertation revolves around finding comprehensive techniques to predict and detect the early degradation of PV modules. As methodological contributions in the thesis deal with testing the linkages between different constructs, the thesis contributes to the PV field by identifying gaps that need to be fulfilled through a comprehensive literature review. Reviewing the scientific literature provides a better understanding and summary of the obstacles that must be overcome, particularly detection techniques of degradation mechanisms of PV modules (Refer to Chapters 1 and 2). Exploring the scientific literature solidifies the thesis approach, and allows rigid investigational studies to be constructed on a methodical basis (Refer to Chapters 3, 4, 5, 6 and 7). This allows trustworthy data to be generated to perform accurate analyses that develop viable and valuable solutions to the degradation problem.

A combination of experimentation and simulation approaches delivered methodological contributions to the detection and prediction techniques of PV failures. Data collected from experiments to observe a progressive degradation of solar cells (Refer to Chapter 4) was analysed to develop and optimise novel and simple detection models of PV failures.

Further, the importance of simulation (Refer to Chapters 3 and 5) in the detection of PV failures was emphasised. Referring to Chapter 3, EVA degradation

had already been investigated through experiments (Refer to Chapters 1,2, and 3), however, when accurate simulations kicked off, the results flow in a broadened range, defining more degradation points that have assisted in originating a mathematical model. The same case has been noticed by referring to Chapter 5, results from shunt resistance degradations have been experimentally obtained (Refer to Chapter 4). Simulations create more degradation scenarios, thereby enabling detection of failed cells in PV modules and ensuring it is still feasible to detect these types of failures. Referring to Chapter 7, evaluation of the cost cannot be conveniently realised without simulation scenarios.

The beginning of the thesis identified two major mechanisms of PV degradation (Refer to Chapters 1 and 2). The simulation and experimental approaches followed by the thesis have led to the subsequent contributions:

- A novel model to predict and detect the early onset of EVA encapsulant failure (Refer to Chapter 3).
- Determining the critical point for shunt resistance degradation (Refer to Chapter 4).
- Novel models to predict and detect shunt resistance degradation before reaching the critical point (Refer to Chapter 4).
- A novel model to predict failed cells in PV modules, and a start for future simulation studies to generate enough data that can be trained by machine learning models (Refer to Chapters 5 and 6)
- Determining the optimal time to replace a PV module affected by EVA and shunt resistance degradations (Refer to Chapter 7).

The criteria given by Pillai and Rajasekar [47] were considered when developing the predictive models, the models are;

A) Simple: can detect failures and degradation by applying unsophisticated steps and basic mathematical calculation (Refer to Chapters 2,3, and 5).

B) Applicable in most PV modules: these models were tested and found to be practical to the polycrystalline modules, one of the most commercial types of PV. Although they were not tested on other common types of PV like monocrystalline and thin films modules, these types of PV are of the same nature as polycrystalline, and they are supposed to be of no significant difference. Organic and perovskite solar cells seem promising technologies in the future, it is recommended to test the predictive models presented by the thesis on those types.

C) Not interfering with power output or causing a blackout: some detection techniques such as EL or IR imaging requires the PV module to be dismantled from the PV field to carry on test in the workshop which causes a temporal blackout. In some developed technologies of IR or EL imaging, causes a shading that will interfere with the power. The literature contains many studies that discuss this problem and suggest a solution to tackle it. Unlike these detection techniques, the developed models can detect PV failure without interfering with power or causing a blackout.

D) Pinpointing and classifying between failures: the developed models were tested to detect the two main degradation mechanisms of PV modules, in which most PV failures progress after these mechanisms initiate. By detecting degradation at its early onset, the developed models will prevent these failures from emerging by allowing an earlier corrective action to be taken. The distinction between the two degradation mechanisms was demonstrated (Refer to Chapters 4 and 6). This criterion, therefore, was partially met .It is proposed in the 'future works' section to conduct more experiments that were reported in the literature to

identify the reduction range of shunt resistance. Hence, optimising the developed models to meet this criterion.

E) Cost-effectiveness: the developed models were cost-effective and did not require expensive instrumentations to be applied (Refer to Chapters 3 and 4). Furthermore, the developed model of shunt resistance (Refer to Chapter 4) degradation is even less costly by eliminating the instrumentation for solar irradiance measurements.

By meeting four of these criteria as well as meeting most of the expected contributions (Refer to Chapter 1), the original work presented in this thesis has contributed to the body of knowledge by demonstrating how progressive failures are indicated by key PV cell parameters and by advancing the detection techniques for PV failures. The thesis's summary linked to the stated contributions is explained further below.

8.2 Thesis Summary

This dissertation has entailed a body of knowledge and information by highlighting the global growth rate in PV modules deployment and stressing the need for an accurate monitoring system to ensure a reliable operation of the PV system. It showed that higher degradation rates and failures when they occur cause a significant reduction in power output and, in the worst-case scenario, may become catastrophic. This motivated the author to search for a novel approach to detect PV failures or critical degradation at the early stages via the PV's *I-V* curve measurements to prevent disastrous consequences.

A state-of-the-art literature review was conducted to scan PV failures, types, and their root cause (Refer to Chapter 2). PV module is constructed with different

components, and each is made from different materials. The literature showed that each element is vulnerable to specific types of failures. Some are considered mild; others may start mildly and then deteriorate faster, especially in harsh environments. It also revealed that the degradation mechanism usually starts with EVA degradation, appears as discolouration, classified under optical failures. In comparison, losses related to solar cells, cell bus bars, bypass diodes and junction box components are classified under electrical failures. The electrical failure and degradation mechanisms, when they occurred, were found to decrease the shunt resistance of the cell, impacting the generated *I-V* characteristics.

In terms of failure detection techniques, it was pointed out that they should be simple, applicable in most PV systems, cost-effective, accurate, and detect failures at low solar irradiance. Typically, detection starts with visual inspection and then employs more instrumental devices like infrared imaging. However, these devices are costly and uncomprehensive, i.e., designed only to detect limited types of failures. However, electrical characterization, which includes monitoring the PV's *I-V* curve, infers most PV failures from the shifts in the output parameters. That seems to explain why it is the most common detection technique.

Since the literature revealed that detection and predicting failures at the early stages protect the system from potential risks, simulations and experiments of early degradation scenarios were conducted: EVA discolouration and low shunt resistance (Refer to Chapters 3,4,5,6 and 7). This allowed us to monitor the alteration of *I-V* characteristics when degradation mechanisms initiate.

A simulation analysis based on experimental data from Pern *et al.* [83] assisted in proposing a novel approach to detect the onset of degradation mechanism caused

by EVA discolouration has been used (Refer to Chapter 3). The simulation was attained by simulation of the solar spectrum received by EVA at several degradation stages. This enabled the extraction of the short-circuit current density and hence the *I-V* major parameters in healthy and faulty EVA scenarios. The simulation outcomes showed that short-circuit current was highly linear when correlated with different levels of expected solar irradiance subjected to EVA degradation. However, I_{SC} was reduced at EVA discolouration, noticeably increasing with a linear fit slope. Therefore, it was used and employed as a simple linear model to detect the early onset of EVA degradation.

An experiment was set to monitor the degradation and failure mechanisms by reducing the PV's cell shunt resistance (Refer to Chapter 4). Fourteen levels of shunt resistance were investigated. Results showed that reduced shunt resistance directly influenced P_{max}, V_{OC}, and fill factor. The threshold point was determined to be *c.* 100 Ω cm^2, indicating the degradation is heading to catastrophic failure. After that, two novel linear models were employed to detect PV degradations and losses associated with low shunt resistance. These models correlate short-circuit current with open-circuit voltage and maximum-power output at different illumination levels. The slopes in these linear models were increased and can be used to detect degradation before the threshold point, allowing for corrective actions to be taken.

Then, the *I-V* curves generated at low shunt resistance levels were accurately simulated via SPICE to detect failed cells when they existed in a PV module, e.g., cell cracks, snail tracks, mismatch, and potential induced degradation (Refer to Chapter 5). In the simulation, the series resistance and saturation current densities

were increased with the shunt resistance reduction to model similar *I-V* curves. This may indicate that these hidden parameters are altered in case of failure.

The same approach has been used to detect these failures. However, the increase in slope when a few cells fail is considered insignificant, which requires precise monitoring to capture it. Furthermore, a mathematical equation was proposed to estimate the number of defective cells in a PV module, allowing a planned and appropriate time for corrective action to be considered.

These models developed from simulation and experimentation relating to degradation scenarios and *I-V* major parameters are applicable, straightforward, and easily implemented for online monitoring systems. Moreover, the level, type of degradation, and reversibility can also be classified by training a machine learning model (Refer to Chapter 6). A direct example of ML showed that machine learning models are practically effective and could be trained to classify between these degradation mechanisms.

Environmental stress influences are one of the dominant causes of PV failure and degradation. Dhahran city in Saudi Arabia has harsh weather; high temperature, relatively high humidity, and dusty make it a suitable location for severe weather experiments (Refer to Chapter 6). Findings showed that dust accumulation leads to a reduction in short-circuit current in a short time, particularly days. Moreover, measurements of a module diagnosed with a hotspot were also taken. As a result, the hotspot module loses power with a reduced fill factor. This helps to understand the required corrective action in failure incidents, where shading caused by dust needs regular cleaning, and to replace a module identified with a hotspot is recommended to restore maximal power output.

On this basis, replacement costs for a degraded PV module, specifically for EVA degradation and shunt resistance degradation, in a PV string or array systems were estimated and compared using the approach given by Quaschning [244] (Refer to Chapter 7). Results showed that replacing a module identified with yellow-brown EVA or shunt resistance degradation was more cost-effective, rather than operating in a string system, even if the replacement is made at a time close to the system's end-life cycle, precisely in year 20.

The same results were found for replacing a degraded shunt resistance module in a PV array system except for replacement before the end-of-life cycle, in year 20. However, replacing the module at the early stage of EVA degradation, yellow-brown discolouration, was costly. Therefore, the optimal time for replacement was after the EVA experienced brown discolouration. Optimal time also depends on the cause of discolouration and whether it is considered mild with no potential risks.

8.3 Future Works

Good research that answers specific questions opens the doors to new questions. In brief, the thesis described and analysed in-depth PV failures and degradations, demonstrating the risk they provide to the system. Detecting them early assures the PV system's safe and dependable operation. In this regard, the research reported in this thesis has resulted in comprehensive, simple, and cost-effective models that can detect these malfunctions and be easily used in PV monitoring. Further suggestions about questions that arose from the thesis can be proposed as follows:

- In Chapter 3, a novel model was proposed to detect uniform degradation of EVA. Experimental and simulation can be carried out to investigate the non-uniform degradation of EVA. That is, EVA discolouration becomes more severe in some cells rather than others. Consequently, the transmittance of some cells becomes less than others and generates a less photo-generating current.

- In Chapters 4 and 5, shunt resistance was linked with PV failures and degradation. Further experiments for each failure's mechanism, listed in the literature review, chapter 2, can be conducted to quantify the reduction range of shunt resistance and its reflection to I-V parameters. Then, machine learning models can be built and implemented to classify PV failures and degradation mechanisms. Furthermore, it has been shown by Wohlgemuth and Kurtz [40] that increment of series resistance in PV module may lead to disastrous consequences resulting from fire. Even though Chapter 5 showed through simulations that series resistance increment is coupled with shunt resistance reduction, further experimentation on series resistance is proposed. Finally, many PV failures start with one cell and then distribute to the other cells of the PV module in a matter of time; the author has found from the literature that PID and microcrack are among these failures. Comprehensive literature reviews and experiments are proposed to list and determine all these failures, quantifying the time they take to cause a critical degradation in a PV module.

- In Chapter 6, harsh weather, scorching with high relative humidity and dusty conditions, such as in Dharan, Saudi Arabia, is problematic for

PV modules. However, as long as the weather has high relative humidity, experiments to investigate if condensing the water vapour is applicable to clean the PV module from dust and decrease the operating temperature are proposed.

REFERENCE LIST

[1] L. Li, J. Lin, N. Wu, S. Xie, C. Meng, Y. Zheng, X. Wang, and Y. Zhao, "Review and outlook on the international renewable energy development," *Energy and Built Environment,* 2020.

[2] M. A. Green, "How did solar cells get so cheap?," *Joule,* vol. 3, no. 3, pp. 631-633, 2019.

[3] A. PSE, "Fraunhofer Institute For Solar Energy Systems ISE," *Photovoltaics Report.(2022)*.

[4] IEA, *Net renewable capacity additions by technology, 2020-2022*, IEA., Paris May/2021.

[5] L. Castaner, and S. Silvestre, *Modelling photovoltaic systems using PSpice*: John Wiley and Sons, 2002.

[6] A. Wang, and Y. Xuan, "A detailed study on loss processes in solar cells," *Energy,* vol. 144, pp. 490-500, 2018.

[7] M. N. I. Sarkar, "Effect of various model parameters on solar photovoltaic cell simulation: a SPICE analysis," *Renewables: Wind, Water, and Solar,* vol. 3, no. 1, pp. 1-9, 2016.

[8] D. M. Chapin, C. Fuller, and G. Pearson, "A new silicon p-n junction photocell for converting solar radiation into electrical power," *Journal of Applied Physics,* vol. 25, no. 5, pp. 676-677, 1954.

[9] L. M. Fraas, "History of solar cell development," *Low-Cost Solar Electric Power*, pp. 1-12: Springer, 2014.

[10] A. Goetzberger, C. Hebling, and H.-W. Schock, "Photovoltaic materials, history, status and outlook," *Materials Science and Engineering: R: Reports,* vol. 40, no. 1, pp. 1-46, 2003.

[11] M. A. Green, E. D. Dunlop, J. Hohl-Ebinger, M. Yoshita, N. Kopidakis, and A. W. Ho-Baillie, "Solar cell efficiency tables (version 55)," *Progress in Photovoltaics: Research and Applications,* vol. 28, no. NREL/JA-5900-75827, 2019.

[12] D. Feldman, and R. Margolis, "H2 2020: Solar Industry Update," 2021.

[13] K. Izumi, J.-W. Arnulf, and D. Jose, *Snapshot of Global PV Markets*, April 2021.

[14] C. Peike, I. Hädrich, K.-A. Weiß, and I. Dürr, "Overview of PV module encapsulation materials," *Photovoltaics International,* vol. 19, pp. 85-92, 2013.

[15] S. Ma, G. Yuan, Y. Zhang, N. Yang, Y. Li, and Q. Chen, “Development of encapsulation strategies towards the commercialization of perovskite solar cells,” *Energy & Environmental Science,* vol. 15, no. 1, pp. 13-55, 2022.

[16] O. Hasan, and A. Arif, “Performance and life prediction model for photovoltaic modules: Effect of encapsulant constitutive behavior,” *Solar energy materials and solar cells,* vol. 122, pp. 75-87, 2014.

[17] D. C. Miller, J. G. Bokria, D. M. Burns, S. Fowler, X. Gu, P. L. Hacke, C. C. Honeker, M. D. Kempe, M. Köhl, and N. H. Phillips, “Degradation in photovoltaic encapsulant transmittance: Results of the first PVQAT TG5 artificial weathering study,” *Progress in Photovoltaics: Research and Applications,* vol. 27, no. 5, pp. 391-409, 2019.

[18] M. López-Escalante, L. J. Caballero, F. Martín, M. Gabás, A. Cuevas, and J. Ramos-Barrado, “Polyolefin as PID-resistant encapsulant material in PV modules,” *Solar Energy Materials and Solar Cells,* vol. 144, pp. 691-699, 2016.

[19] M. Kempe, "Overview of scientific issues involved in selection of polymers for PV applications." In *2011 37th IEEE Photovoltaic Specialists Conference*, pp. 000085-000090. IEEE, 2011.

[20] B. M. Habersberger, P. Hacke, and L. S. Madenjian, "Evaluation of the PID-s susceptibility of modules encapsulated in materials of varying resistivity." In *2018 IEEE 7th World Conference on Photovoltaic Energy Conversion (WCPEC)(A Joint Conference of 45th IEEE PVSC, 28th PVSEC & 34th EU PVSEC)*, pp. 3807-3809. IEEE, 2018.

[21] J. Kapur, K. M. Stika, C. S. Westphal, J. L. Norwood, and B. Hamzavytehrany, “Prevention of potential-induced degradation with thin ionomer film,” *IEEE Journal of Photovoltaics,* vol. 5, no. 1, pp. 219-223, 2014.

[22] C. Peike, L. Purschke, K.-A. Weiss, M. Köhl, and M. Kempe, "Towards the origin of photochemical EVA discoloration." In *2013 IEEE 39th Photovoltaic Specialists Conference (PVSC)*, pp. 1579-1584. IEEE, 2013.

[23] N. Kyranaki, A. Smith, K. Yendall, D. A. Hutt, D. C. Whalley, R. Gottschalg, and T. R. Betts, “Damp-heat induced degradation in photovoltaic modules manufactured with passivated emitter and rear contact solar cells,” *Progress in Photovoltaics: Research and Applications*.

[24] A. Badiee, I. Ashcroft, and R. D. Wildman, “The thermo-mechanical degradation of ethylene vinyl acetate used as a solar panel adhesive and encapsulant,” *International Journal of Adhesion and Adhesives,* vol. 68, pp. 212-218, 2016.

[25] U. Desai, B. K. Sharma, A. Singh, and A. Singh, "A comparison of evolution of adhesion mechanisms and strength post damp-heat aging for a range of VA content in EVA encapsulant with photovoltaic backsheet," *Solar Energy*, vol. 231, pp. 908-920, 2022.

[26] H. Wang, X. Cheng, H. Yang, W. He, Z. Chen, L. Xu, and D. Song, "Potential-induced degradation: Recombination behavior, temperature coefficients and mismatch losses in crystalline silicon photovoltaic power plant," *Solar Energy*, vol. 188, pp. 258-264, 2019.

[27] M. Vázquez, and I. Rey-Stolle, "Photovoltaic module reliability model based on field degradation studies," *Progress in photovoltaics: Research and Applications*, vol. 16, no. 5, pp. 419-433, 2008.

[28] D. H. Daher, L. Gaillard, and C. Ménézo, "Experimental assessment of long-term performance degradation for a PV power plant operating in a desert maritime climate," *Renewable Energy*, 2022.

[29] J. Wohlgemuth, *IEC 61215: What it is and isn't (Presentation)*, National Renewable Energy Lab.(NREL), Golden, CO (United States), 2012.

[30] D. C. Jordan, B. Sekulic, B. Marion, and S. R. Kurtz, "Performance and aging of a 20-year-old silicon PV system," *IEEE Journal of Photovoltaics*, vol. 5, no. 3, pp. 744-751, 2015.

[31] H. Han, X. Dong, B. Li, H. Yan, P. J. Verlinden, J. Liu, J. Huang, Z. Liang, and H. Shen, "Degradation analysis of crystalline silicon photovoltaic modules exposed over 30 years in hot-humid climate in China," *Solar Energy*, vol. 170, pp. 510-519, 2018.

[32] A. Ndiaye, A. Charki, A. Kobi, C. M. F. Kébé, P. A. Ndiaye, and V. Sambou, "Degradations of silicon photovoltaic modules: A literature review," *Solar Energy*, vol. 96, pp. 140-151, 2013.

[33] A. Triki-Lahiani, A. B.-B. Abdelghani, and I. Slama-Belkhodja, "Fault detection and monitoring systems for photovoltaic installations: A review," *Renewable and Sustainable Energy Reviews*, vol. 82, pp. 2680-2692, 2018.

[34] A. Bai, J. Popp, P. Balogh, Z. Gabnai, B. Pályi, I. Farkas, G. Pintér, and H. Zsiborács, "Technical and economic effects of cooling of monocrystalline photovoltaic modules under Hungarian conditions," *Renewable and Sustainable Energy Reviews*, vol. 60, pp. 1086-1099, 2016.

[35] D. C. Jordan, S. R. Kurtz, K. VanSant, and J. Newmiller, "Compendium of photovoltaic degradation rates," *Progress in Photovoltaics: Research and Applications*, vol. 24, no. 7, pp. 978-989, 2016.

[36] M. Köntges, S. Kurtz, C. Packard, U. Jahn, K. A. Berger, K. Kato, T. Friesen, H. Liu, and M. Van Iseghem, "Review of failures of photovoltaic

modules IEA PVPS Task 13 external final report March 2014," *IEA-PVPS T13-01,* vol. 2014, 2014.

[37] Y. R. Golive, S. Zachariah, R. Dubey, S. Chattopadhyay, S. Bhaduri, H. K. Singh, B. Bora, S. Kumar, A. K. Tripathi, and A. Kottantharayil, "Analysis of field degradation rates observed in all-India survey of photovoltaic module reliability 2018," *IEEE Journal of Photovoltaics,* vol. 10, no. 2, pp. 560-567, 2019.

[38] D. A. Quansah, and M. S. Adaramola, "Ageing and degradation in solar photovoltaic modules installed in northern Ghana," *Solar Energy,* vol. 173, pp. 834-847, 2018.

[39] F. A. Olivencia Polo, J. Ferrero Bermejo, J. F. Gómez Fernández, and A. Crespo Márquez, "Failure mode prediction and energy forecasting of PV plants to assist dynamic maintenance tasks by ANN based models," *Renewable Energy,* vol. 81, pp. 227-238, 2015.

[40] A. Sepanski, F. Reil, W. Vaaßen, E. Janknecht, U. Hupach, N. Bogdanski, and B. van Heeckeren, "Assessing Fire Risks in Photovoltaic Systems and Developing Safety Concepts for Risk Minimization," *Report by US Department of Energy, Solar Energy Technologies Office (June, 2018)* (2018).

[41] P. Cancelliere, "PV electrical plants fire risk assessment and mitigation according to the Italian national fire services guidelines," *Fire and Materials,* vol. 40, no. 3, pp. 355-367, 2016.

[42] N. A. F. Mohd Nizam Ong, M. Z. Mohd Tohir, M. M. Mutlak, M. A. Sadiq, R. Omar, and M. S. Md Said, "BowTie analysis of rooftop grid-connected photovoltaic systems," *Process Safety Progress,* vol. 41, pp. S106-S117, 2022.

[43] J. H. Wohlgemuth, and S. R. Kurtz, "How can we make PV modules safer?," *2012 38th IEEE Photovoltaic Specialists Conference,* pp. 003162-003165, 2012.

[44] M. Aram, X. Zhang, D. Qi, and Y. Ko, "A State-of-the-Art Review of Fire Safety of Photovoltaic Systems in Buildings," *Journal of Cleaner Production,* pp. 127239, 2021.

[45] S. Blazey, "Fire and Solar PV Systems–Investigations and Evidence," 2017.

[46] Z. Wu, Y. Hu, J. X. Wen, F. Zhou, and X. Ye, "A review for solar panel fire accident prevention in large-scale PV applications," *IEEE Access,* vol. 8, pp. 132466-132480, 2020.

[47] D. S. Pillai, and N. Rajasekar, “A comprehensive review on protection challenges and fault diagnosis in PV systems,” *Renewable and Sustainable Energy Reviews,* vol. 91, pp. 18-40, 2018.

[48] K. Schulze, M. Groh, M. Nieß, C. Vodermayer, G. Wotruba, and G. Becker, "Untersuchung von Alterungseffekten bei monokristallinen PV-Modulen mit mehr als 15 Betriebsjahren durch Elektrolumineszenz-und Leistungsmessung."

[49] D. C. Jordan, and S. R. Kurtz, “Photovoltaic degradation rates—an analytical review,” *Progress in photovoltaics: Research and Applications,* vol. 21, no. 1, pp. 12-29, 2013.

[50] S. Durand, and D. Bowling, “Field experience with photovoltaic systems: Ten-year assessment. *Final report*. No. EPRI-TR-102138. Electric Power Research Inst., Palo Alto, CA (United States); Southwest Technology Development Inst., Las Cruces, NM (United States), 1993.

[51] I. IEC, “60050-191: International electrotechnical vocabulary: Chapter 191: Dependability and quality of service,” *International Electrotechnical Commission, Geneva*, 1990.

[52] D. C. Jordan, T. J. Silverman, J. H. Wohlgemuth, S. R. Kurtz, and K. T. VanSant, “Photovoltaic failure and degradation modes,” *Progress in Photovoltaics: Research and Applications,* vol. 25, no. 4, pp. 318-326, 2017.

[53] D. Jordan, N. Haegel, and T. Barnes, “Photovoltaics module reliability for the terawatt age,” *Progress in Energy*, 2022.

[54] I. Romero-Fiances, A. Livera, M. Theristis, G. Makrides, J. S. Stein, G. Nofuentes, J. de la Casa, and G. E. Georghiou, “Impact of duration and missing data on the long-term photovoltaic degradation rate estimation,” *Renewable Energy,* vol. 181, pp. 738-748, 2022.

[55] W. Heywang, and K. H. Zaininger, "Silicon: the semiconductor material," *Silicon*, pp. 25-42: Springer, 2004.

[56] A. Kılıç, and A. Öztürk, *Güneş enerjisi*: Kipaş Dağıtımcılık, 1983.

[57] M. Gürtürk, H. Benli, and N. K. Ertürk, “Determination of the effects of temperature changes on solar glass used in photovoltaic modules,” *Renewable Energy,* vol. 145, pp. 711-724, 2020.

[58] J. A. Tsanakas, L. Ha, and C. Buerhop, “Faults and infrared thermographic diagnosis in operating c-Si photovoltaic modules: A review of research and future challenges,” *Renewable and Sustainable Energy Reviews,* vol. 62, pp. 695-709, 2016.

[59] P. K. Enaganti, A. Bhattacharjee, A. Ghosh, Y. N. Chanchangi, C. Chakraborty, T. K. Mallick, and S. Goel, "Experimental investigations for dust build-up on low-iron glass exterior and its effects on the performance of solar PV systems," *Energy*, vol. 239, pp. 122213, 2022.

[60] D. King, M. Quintana, J. Kratochvil, D. Ellibee, and B. Hansen, "Photovoltaic module performance and durability following long-term field exposure," *Progress in Photovoltaics: research and applications*, vol. 8, no. 2, pp. 241-256, 2000.

[61] D. King, F. Pern, J. Pitts, C. Bingham, and A. Czanderna, "Optical changes in cerium-containing glass as a result of accelerated exposure testing [of PV modules]." In *Conference Record of the Twenty Sixth IEEE Photovoltaic Specialists Conference-1997*, pp. 1117-1120. IEEE, 1997.

[62] M. D. Kempe, T. Moricone, and M. Kilkenny, "Effects of cerium removal from glass on photovoltaic module performance and stability." In *Reliability of photovoltaic cells, modules, components, and systems II*, vol. 7412, pp. 203-214. SPIE, 2009.

[63] M. A. Hossion, "Visual and electrical degradation data of five years aged rooftop photovoltaic modules," *Data in Brief*, vol. 31, pp. 105762, 2020.

[64] D. A. Quansah, and M. S. Adaramola, "Comparative study of performance degradation in poly- and mono-crystalline-Si solar PV modules deployed in different applications," *International Journal of Hydrogen Energy*, vol. 43, no. 6, pp. 3092-3109, 2018.

[65] S. Dietrich, M. Pander, M. Ebert, and J. Bagdahn, "Mechanical assessment of large photovoltaic modules by test and finite element analysis." In *23rd European Photovoltaic Solar Energy Conference. Valencia, Spain*. 2008.

[66] R. Cavieres, R. Barraza, D. Estay, J. Bilbao, and P. Valdivia-Lefort, "Automatic soiling and partial shading assessment on PV modules through RGB images analysis," *Applied Energy*, vol. 306, pp. 117964, 2022.

[67] S. S. Chandel, M. Nagaraju Naik, V. Sharma, and R. Chandel, "Degradation analysis of 28 year field exposed mono-c-Si photovoltaic modules of a direct coupled solar water pumping system in western Himalayan region of India," *Renewable Energy*, vol. 78, pp. 193-202, 2015.

[68] S. Deng, Z. Zhang, C. Ju, J. Dong, Z. Xia, X. Yan, T. Xu, and G. Xing, "Research on hot spot risk for high-efficiency solar module," *Energy Procedia*, vol. 130, pp. 77-86, 2017.

[69] T. Ghanbari, "Permanent partial shading detection for protection of photovoltaic panels against hot spotting," *IET Renewable Power Generation*, vol. 11, no. 1, pp. 123-131, 2016.

[70] M. S. b. Jadin, S. F. A. Safian, K. H. Ghazali, T. L. Ven, and A. S. M. Shah, "Hotspot Detection in Photovoltaic Array Using Thermal Imaging Method," *Proceedings of the 6th International Conference on Electrical, Control and Computer Engineering*, pp. 101-107, 2022.

[71] J. W. Lathrop, R. A. Hartman, and C. R. Saylor, "Investigation of reliability attributes and accelerated stress factors on terrestrial solar cells," *Third annual report*. No. DOE/JPL/954929-81/8. Clemson Univ., SC (USA), 1981.

[72] N. Bansal, S. P. Jaiswal, and G. Singh, "Comparative investigation of performance evaluation, degradation causes, impact and corrective measures for ground mount and rooftop solar PV plants–A review," *Sustainable Energy Technologies and Assessments,* vol. 47, pp. 101526, 2021.

[73] P. Manganiello, M. Balato, and M. Vitelli, "A survey on mismatching and aging of PV modules: The closed loop," *IEEE Transactions on Industrial Electronics,* vol. 62, no. 11, pp. 7276-7286, 2015.

[74] W. Stark, and M. Jaunich, "Investigation of Ethylene/Vinyl Acetate Copolymer (EVA) by thermal analysis DSC and DMA," *Polymer Testing,* vol. 30, no. 2, pp. 236-242, 2011.

[75] A. Gok, D. A. Gordon, M. Wang, R. H. French, and L. S. Bruckman, "Degradation Science and Pathways in PV Systems," *Durability and Reliability of Polymers and Other Materials in Photovoltaic Modules*, pp. 47-93: Elsevier, 2019.

[76] L. E. Perret-Aebi, H. Y. Li, R. Théron, G. Roeder, Y. Luo, T. Turlings, R. F. M. Lange, and C. Ballif, "Insights on EVA lamination process: Where do the Bubbles Come From," *25th European Photovoltaic Solar Energy Conference and Exhibition, Valencia, Spain*, 2010.

[77] S. Karthikeyan, G. B. Ajay, N. R. Ahamed, and A. Sharun, "Edge AI–Based Aerial Monitoring," *Applied Edge AI: Concepts, Platforms, and Industry Use Cases*, pp. 237, 2022.

[78] S. M. Shrestha, J. K. Mallineni, K. R. Yedidi, B. Knisely, S. Tatapudi, J. Kuitche, and G. TamizhMani, "Determination of dominant failure modes using FMECA on the field deployed c-Si modules under hot-dry desert climate," *IEEE journal of photovoltaics*, vol. 5, no. 1, pp. 174-182, 2014.

[79] P. Rajput, G. N. Tiwari, O. S. Sastry, B. Bora, and V. Sharma, "Degradation of mono-crystalline photovoltaic modules after 22 years of outdoor exposure in the composite climate of India," *Solar Energy,* vol. 135, pp. 786-795, 2016.

[80] M. C. C. de Oliveira, A. S. A. D. Cardoso, M. M. Viana, and V. d. F. C. Lins, “The causes and effects of degradation of encapsulant ethylene vinyl acetate copolymer (EVA) in crystalline silicon photovoltaic modules: A review,” *Renewable and Sustainable Energy Reviews,* vol. 81, pp. 2299-2317, 2018.

[81] J. Frederick, H. Snell, and E. Haywood, “Solar ultraviolet radiation at the earth's surface,” *Photochemistry and Photobiology,* vol. 50, no. 4, pp. 443-450, 1989.

[82] E. Klampaftis, M. Congiu, N. Robertson, and B. S. Richards, “Luminescent ethylene vinyl acetate encapsulation layers for enhancing the short wavelength spectral response and efficiency of silicon photovoltaic modules,” *IEEE Journal of Photovoltaics,* vol. 1, no. 1, pp. 29-36, 2011.

[83] M. S. A. Kamel, M. Oelgemöller, and M. V. Jacob, “Sustainable plasma polymer encapsulation materials for organic solar cells,” *Journal of Materials Chemistry A,* vol. 10, no. 9, pp. 4683-4694, 2022.

[84] K. Cristofoli, “Preparação e caracterização de filmes de PEBD aditivados com fotoestabilizantes para a proteção de espumantes rose,” 2014.

[85] W. H. Holley, S. C. Agro, J. P. Galica, L. A. Thoma, R. S. Yorgensen, M. Ezrin, P. Klemchuk, and G. Lavigne, "Investigation into the causes of browning in EVA encapsulated flat plate PV modules." In *Proceedings of 1994 IEEE 1st World Conference on Photovoltaic Energy Conversion-WCPEC (A Joint Conference of PVSC, PVSEC and PSEC)*, vol. 1, pp. 893-896. IEEE, 1994.

[86] S. Jiang, K. Wang, H. Zhang, Y. Ding, and Q. Yu, “Encapsulation of PV modules using ethylene vinyl acetate copolymer as the encapsulant,” *Macromolecular Reaction Engineering,* vol. 9, no. 5, pp. 522-529, 2015.

[87] M. Noman, S. Tu, S. Ahmad, F. U. Zafar, H. A. Khan, S. U. Rehman, M. Waqas, A. D. Khan, and O. u. Rehman, “Assessing the reliability and degradation of 10–35 years field-aged PV modules,” *Plos one,* vol. 17, no. 1, pp. e0261066, 2022.

[88] P. Arularasu, “Combined UV-temperature-humidity Accelerated Testing of PV Modules: Reliability of UV-cut and UV-pass EVA Encapsulants,” *Reliability of UV-cut and UV-pass EVA encapsulants*. Arizona State University, 2019.

[89] “ISO, Standard 17223 “Plastics - Determination of yellowness index and change in yellowness index” (2014). .”

[90] M. C. C. de Oliveira, D. A. Cassini, A. S. A. C. Diniz, L. G. Soares, M. M. Viana, L. L. Kazmerski, and V. d. F. C. Lins, “Comparison and analysis of

performance and degradation differences of crystalline-Si photovoltaic modules after 15-years of field operation," *Solar Energy,* vol. 191, pp. 235-250, 2019.

[91] H. Yong, T. Minemoto, and T. Takahashi, "Dependence of Photovoltage on Incident Photon Energies Investigated by Photo-assisted Kelvin Probe Force Microscopy on Cu (In, Ga) Se 2 Solar Cells." in *2018 IEEE 7th World Conference on Photovoltaic Energy Conversion (WCPEC)(A Joint Conference of 45th IEEE PVSC, 28th PVSEC & 34th EU PVSEC)*, 2018: IEEE, pp. 1966-1969.

[92] B. Adothu, S. Chattopadhyay, P. Bhatt, P. Hui, F. R. Costa, and S. Mallick, "Early-stage identification of encapsulants photobleaching and discoloration in crystalline silicon photovoltaic module laminates," *Progress in Photovoltaics: Research and Applications*.

[93] E. Kaplani, "Detection of degradation effects in field-aged c-Si solar cells through IR thermography and digital image processing," *International Journal of Photoenergy,* vol. 2012, 2012.

[94] S. Kurtz, "Photovoltaic Module Reliability Workshop 2014: February 25-26, 2014," 2014.

[95] C. Ferrara, and D. Philipp, "Why Do PV Modules Fail?," *Energy Procedia,* vol. 15, pp. 379-387, 2012.

[96] F. Rosillo, and M. Alonso-Garcia, "Evaluation of color changes in PV modules using reflectance measurements," *Solar Energy,* vol. 177, pp. 531-537, 2019.

[97] F. Pern, A. Czanderna, K. Emery, and R. Dhere, "Weathering degradation of EVA encapsulant and the effect of its yellowing on solar cell efficiency." in *The Conference Record of the Twenty-Second IEEE Photovoltaic Specialists Conference-1991*, 1991, vol. 1: IEEE, pp. 557-561.

[98] C. Dechthummarong, B. Wiengmoon, D. Chenvidhya, C. Jivacate, and K. Kirtikara, "Physical deterioration of encapsulation and electrical insulation properties of PV modules after long-term operation in Thailand," *Solar energy materials and solar cells,* vol. 94, no. 9, pp. 1437-1440, 2010.

[99] C. S. T. Photovoltaic, "Modules—Design Qualification and Type Approval," *IEC,* vol. 1215, pp. 2005-05, 2005.

[100] A. S. A. Diniz, D. A. Cassini, M. C. de Oliveira, V. F. de Lins, M. M. Viana, D. S. Braga, and L. L. Kazmerski, "Evaluation of Performance Losses and Degradation of Aged Crystalline Si Photovoltaic Modules Installed in Minas Gerais (Brazil)," *Renewable Energy and Sustainable Buildings,* pp. 29-46: Springer, 2020.

[101] M. Dhimish, "Micro cracks distribution and power degradation of polycrystalline solar cells wafer: Observations constructed from the analysis of 4000 samples," *Renewable Energy,* vol. 145, pp. 466-477, 2020.
[102] A. Eslami Majd, and N. N. Ekere, "Crack initiation and growth in PV module interconnection," *Solar Energy,* vol. 206, pp. 499-507, 2020.
[103] P. Grunow, P. Clemens, V. Hoffmann, B. Litzenburger, and L. Podlowski, "Influence of micro cracks in multi-crystalline silicon solar cells on the reliability of PV modules," *Proceedings of the 20th EUPVSEC,* pp. 2042-2047, 2005.
[104] L. L. C. BrightSpot Automation, and M. A. Westford, "Solar panel design factors to reduce the impact of cracked cells and the tendency for crack propagation," *NREL PV Module Reliability Workshop, Denver, CO USA*, 2015.
[105] M. Sander, S. Dietrich, M. Pander, S. Schweizer, M. Ebert, and J. Bagdahn, "Investigations on crack development and crack growth in embedded solar cells," *Reliability of Photovoltaic Cells, Modules, Components, and Systems IV,* vol. 8112, pp. 811209, 2011.
[106] C. Buerhop, D. Schlegel, C. Vodermayer, and M. Nieß, "Quality control of PV-modules in the field using infrared-thermography." In *26th European Photovoltaic Solar Energy Conference*, pp. 3894-3897. 2011.
[107] A. Dolara, S. Leva, G. Manzolini, and E. Ogliari, "Investigation on performance decay on photovoltaic modules: Snail trails and cell microcracks," *IEEE journal of photovoltaics,* vol. 4, no. 5, pp. 1204-1211, 2014.
[108] I. Duerr, J. Bierbaum, J. Metzger, J. Richter, and D. Philipp, "Silver Grid Finger Corrosion on Snail Track affected PV Modules – Investigation on Degradation Products and Mechanisms," *Energy Procedia,* vol. 98, pp. 74-85, 2016.
[109] R. Swanson, M. Cudzinovic, D. DeCeuster, V. Desai, J. Jürgens, N. Kaminar, W. Mulligan, L. Rodrigues-Barbarosa, D. Rose, and D. Smith, "The surface polarization effect in high-efficiency silicon solar cells," *15th PVSEC,* 2005.
[110] M. Köntges, S. Kurtz, C. Packard, U. Jahn, K. A. Berger, K. Kato, T. Friesen, H. Liu, M. Van Iseghem, and J. Wohlgemuth, "Review of failures of photovoltaic modules," 2014.
[111] M. Dhimish, and A. M. Tyrrell, "Power loss and hotspot analysis for photovoltaic modules affected by potential induced degradation," *npj Materials Degradation,* vol. 6, no. 1, pp. 1-8, 2022.

[112] M. Köntges, G. Oreski, U. Jahn, M. Herz, P. Hacke, and K.-A. Weiß, *Assessment of Photovoltaic Module Failures in the Field: International Energy Agency Photovoltaic Power Systems Programme: IEA PVPS Task 13, Subtask 3: Report IEA-PVPS T13-09: 2017*: International Energy Agency, 2017.

[113] S. Pingel, S. Janke, and O. Frank, "Recovery methods for modules affected by potential induced degradation (PID)," *27th European Photovoltaic Solar Energy Conference and Exhibition (Frankfurt)*, pp. 3379-3383, 2012.

[114] M. Köntges, S. Kajari-Schröder, and I. Kunze, "Cell cracks measured by UV fluorescence in the field," *Proceedings of the 27th EU PVSEC, Frankfurt, Germany*, pp. 3033-3040, 2012.

[115] M. Köntges, S. Altmann, T. Heimberg, U. Jahn, and K. A. Berger, "Mean degradation rates in PV systems for various kinds of PV module failures," *Proceedings of the 32nd European Photovoltaic Solar Energy Conference and Exhibition, Munich, Germany*, pp. 21-24, 2016.

[116] S. Kurtz, "2017 NREL Photovoltaic Reliability Workshop," 2017.

[117] G. Illya, V. Handara, M. Siahandan, A. Nathania, and A. S. Budiman, "Mechanical Studies of Solar Photovoltaics (PV) Backsheets Under Salt Damp Heat Environments," *Procedia Engineering*, vol. 215, pp. 238-245, 2017.

[118] Z. Wu, S. Lyu, Q. Peng, H. Han, and D. Zhu, "Thermomechanical Stress Distribution Analysis of Junction Box on Silicon Photovoltaic Modules Based on Finite Element Analysis," *IEEE Journal of Photovoltaics*, vol. 9, no. 6, pp. 1716-1720, 2019.

[119] E. Diaz-Dorado, A. Suárez-García, C. Carrillo, and J. Cidras, "Influence of the shadows in photovoltaic systems with different configurations of bypass diodes." in *SPEEDAM 2010*, 2010: IEEE, pp. 134-139.

[120] M. Karimi, H. Samet, T. Ghanbari, and E. Moshksar, "A current based approach for hotspot detection in photovoltaic strings," *International Transactions on Electrical Energy Systems*, vol. 30, no. 9, pp. e12517, 2020.

[121] K. A. Kim, and P. T. Krein, "Hot spotting and second breakdown effects on reverse IV characteristics for mono-crystalline Si photovoltaics." in *2013 IEEE Energy Conversion Congress and Exposition*, 2013: IEEE, pp. 1007-1014.

[122] AE-Solar, "SMART MODULES WITH HOT-SPOT FREE TECHNOLOGY," 2018.

[123] R. G. Ross, “PV reliability development lessons from JPL's flat plate solar array project,” *IEEE Journal of Photovoltaics,* vol. 4, no. 1, pp. 291-298, 2013.

[124] H. Oufettoul, S. Motahhir, G. Aniba, M. Masud, and M. A. AlZain, “Improved TCT topology for shaded photovoltaic arrays,” *Energy Reports,* vol. 8, pp. 5943-5956, 2022.

[125] S. A. Spanoche, J. D. Stewart, S. L. Hawley, and I. E. Opris, “Model-based method for partially shaded PV modules hot spot suppression,” *2012 IEEE 38th photovoltaic specialists conference (PVSC) PART 2*, pp. 1-7, 2012.

[126] W. Herrmann, W. Wiesner, and W. Vaassen, "Hot spot investigations on PV modules-new concepts for a test standard and consequences for module design with respect to bypass diodes." In *Conference Record of the Twenty Sixth IEEE Photovoltaic Specialists Conference-1997*, pp. 1129-1132. IEEE, 1997.

[127] J. M. Kuitche, R. Pan, and G. TamizhMani, “Investigation of Dominant Failure Mode(s) for Field-Aged Crystalline Silicon PV Modules Under Desert Climatic Conditions,” *IEEE Journal of Photovoltaics,* vol. 4, no. 3, pp. 814-826, 2014.

[128] A. K. Tripathi, M. Aruna, and C. S. N. Murthy, “Output power loss of photovoltaic panel due to dust and temperature,” *International Journal of Renewable Energy Research,* vol. 7, no. 1, pp. 439-442, 2017.

[129] K. Hasan, S. B. Yousuf, M. S. H. K. Tushar, B. K. Das, P. Das, and M. S. Islam, “Effects of different environmental and operational factors on the PV performance: A comprehensive review,” *Energy Science & Engineering,* vol. 10, no. 2, pp. 656-675, 2022.

[130] A. A. Abdallah, K. Ali, M. M. Kivambe, and B. Darussalam, “Common failure modes observed in PV system installed in desert climate.”

[131] N. Bansal, S. P. Jaiswal, and G. Singh, “Prolonged degradation and reliability assessment of installed modules operational for 10 years in 5 MW PV plant in hot semi-arid climate,” *Energy for Sustainable Development,* vol. 68, pp. 373-389, 2022.

[132] M. Santhakumari, and N. Sagar, “A review of the environmental factors degrading the performance of silicon wafer-based photovoltaic modules: Failure detection methods and essential mitigation techniques,” *Renewable and Sustainable Energy Reviews,* vol. 110, pp. 83-100, 2019.

[133] H. Nagel, A. Metz, and K. Wangemann, "Crystalline Si solar cells and modules featuring excellent stability against potential-induced

degradation." In *26th European Photovoltaic Solar Energy Conference and Exhibition*, pp. 3107-3112. 2011.

[134] F. M. Zaihidee, S. Mekhilef, M. Seyedmahmoudian, and B. Horan, "Dust as an unalterable deteriorative factor affecting PV panel's efficiency: Why and how," *Renewable and Sustainable Energy Reviews,* vol. 65, pp. 1267-1278, 2016.

[135] M. Saidan, A. G. Albaali, E. Alasis, and J. K. Kaldellis, "Experimental study on the effect of dust deposition on solar photovoltaic panels in desert environment," *Renewable Energy,* vol. 92, pp. 499-505, 2016.

[136] U. Mehmood, F. A. Al-Sulaiman, and B. Yilbas, "Characterization of dust collected from PV modules in the area of Dhahran, Kingdom of Saudi Arabia, and its impact on protective transparent covers for photovoltaic applications," *Solar Energy,* vol. 141, pp. 203-209, 2017.

[137] S. Fan, Y. Wang, S. Cao, T. Sun, and P. Liu, "A novel method for analyzing the effect of dust accumulation on energy efficiency loss in photovoltaic (PV) system," *Energy,* pp. 121112, 2021.

[138] S. A. M. Said, and H. M. Walwil, "Fundamental studies on dust fouling effects on PV module performance," *Solar Energy,* vol. 107, pp. 328-337, 2014.

[139] A. Sayigh, S. Al-Jandal, and H. Ahmed, "Dust effect on solar flat surfaces devices in Kuwait." In *Proceedings of the workshop on the physics of non-conventional energy sources and materials science for energy*, pp. 353-367. ICTP Triest, Italy, 1985.

[140] H. K. Elminir, A. E. Ghitas, R. Hamid, F. El-Hussainy, M. Beheary, and K. M. Abdel-Moneim, "Effect of dust on the transparent cover of solar collectors," *Energy conversion and management,* vol. 47, no. 18-19, pp. 3192-3203, 2006.

[141] S. R. Madeti, and S. Singh, "A comprehensive study on different types of faults and detection techniques for solar photovoltaic system," *Solar Energy,* vol. 158, pp. 161-185, 2017.

[142] M. K. Alam, F. Khan, J. Johnson, and J. Flicker, "A comprehensive review of catastrophic faults in PV arrays: types, detection, and mitigation techniques," *IEEE Journal of Photovoltaics,* vol. 5, no. 3, pp. 982-997, 2015.

[143] A. Mellit, G. M. Tina, and S. A. Kalogirou, "Fault detection and diagnosis methods for photovoltaic systems: A review," *Renewable and Sustainable Energy Reviews,* vol. 91, pp. 1-17, 2018.

[144] D. S. Pillai, and N. Rajasekar, "Metaheuristic algorithms for PV parameter identification: A comprehensive review with an application to threshold setting for fault detection in PV systems," *Renewable and Sustainable Energy Reviews,* vol. 82, pp. 3503-3525, 2018.

[145] M. M. Rahman, J. Selvaraj, N. Rahim, and M. Hasanuzzaman, "Global modern monitoring systems for PV based power generation: A review," *Renewable and Sustainable Energy Reviews,* vol. 82, pp. 4142-4158, 2018.

[146] I. E. C. Standard, "61215 Crystalline Silicon Terrestrial Photovoltaic (PV) ModulesDesign Qualification and Type Approval," *International Electrotechnical Commission,* 1995.

[147] N. M. Kumar, K. Sudhakar, M. Samykano, and V. Jayaseelan, "On the technologies empowering drones for intelligent monitoring of solar photovoltaic power plants," *Procedia computer science,* vol. 133, pp. 585-593, 2018.

[148] K. Drabczyk, G. Kulesza-Matlak, A. Drygała, M. Szindler, and M. Lipiński, "Electroluminescence imaging for determining the influence of metallization parameters for solar cell metal contacts," *Solar Energy,* vol. 126, pp. 14-21, 2016.

[149] W. Hobbs, O. Lavrova, and B. Lockridge, *Comparison of Electroluminescence Image Capture Methods*, Sandia National Lab.(SNL-NM), Albuquerque, NM (United States), 2016.

[150] I. Høiaas, K. Grujic, A. G. Imenes, I. Burud, E. Olsen, and N. Belbachir, "Inspection and condition monitoring of large-scale photovoltaic power plants: A review of imaging technologies," *Renewable and Sustainable Energy Reviews,* vol. 161, pp. 112353, 2022.

[151] S. Kajari-Schröder, I. Kunze, U. Eitner, and M. Köntges, "Spatial and orientational distribution of cracks in crystalline photovoltaic modules generated by mechanical load tests," *Solar Energy Materials and Solar Cells,* vol. 95, no. 11, pp. 3054-3059, 2011.

[152] W. Dallas, O. Polupan, and S. Ostapenko, "Resonance ultrasonic vibrations for crack detection in photovoltaic silicon wafers," *Measurement Science and Technology,* vol. 18, no. 3, pp. 852, 2007.

[153] A. Belyaev, O. Polupan, W. Dallas, S. Ostapenko, D. Hess, and J. Wohlgemuth, "Crack detection and analyses using resonance ultrasonic vibrations in full-size crystalline silicon wafers," *Applied Physics Letters,* vol. 88, no. 11, pp. 111907, 2006.

[154] S. A. Hamid, and M. N. Zulkifli, “Microstructure Evaluation of Photovoltaic Solar Panel’s Interconnection: A Review,” *Materials Science Forum,* vol. 1055, pp. 27-35, 2022.
[155] A. Rifat, P. P. Pandao, and B. S. Babu, “Solar Powered Fault Detection System for Railway Tracks,” *European Journal of Electrical Engineering and Computer Science,* vol. 6, no. 1, pp. 39-43, 2022.
[156] F. Harrou, Y. Sun, B. Taghezouit, A. Saidi, and M.-E. Hamlati, “Reliable fault detection and diagnosis of photovoltaic systems based on statistical monitoring approaches,” *Renewable energy,* vol. 116, pp. 22-37, 2018.
[157] E. Garoudja, F. Harrou, Y. Sun, K. Kara, A. Chouder, and S. Silvestre, “Statistical fault detection in photovoltaic systems,” *Solar Energy,* vol. 150, pp. 485-499, 2017.
[158] M. H. Ali, A. Rabhi, A. El Hajjaji, and G. M. Tina, “Real time fault detection in photovoltaic systems,” *Energy Procedia,* vol. 111, pp. 914-923, 2017.
[159] E. Garoudja, A. Chouder, K. Kara, and S. Silvestre, “An enhanced machine learning based approach for failures detection and diagnosis of PV systems,” *Energy conversion and management,* vol. 151, pp. 496-513, 2017.
[160] L. Chen, S. Li, and X. Wang, “Quickest fault detection in photovoltaic systems,” *IEEE Transactions on Smart Grid,* vol. 9, no. 3, pp. 1835-1847, 2016.
[161] W. Chine, A. Mellit, V. Lughi, A. Malek, G. Sulligoi, and A. M. Pavan, “A novel fault diagnosis technique for photovoltaic systems based on artificial neural networks,” *Renewable Energy,* vol. 90, pp. 501-512, 2016.
[162] D. T. Cotfas, P. A. Cotfas, and S. Kaplanis, “Methods to determine the dc parameters of solar cells: A critical review,” *Renewable and Sustainable Energy Reviews,* vol. 28, pp. 588-596, 2013.
[163] J.-S. Pan, A.-Q. Tian, T.-S. Pan, and S.-C. Chu, "Parameters Extraction of Solar Cell Using an Improved QUasi-Affine TRansformation Evolution (QUATRE) Algorithm," *Advances in Intelligent Systems and Computing*, pp. 253-263: Springer, 2022.
[164] J. Qin, L. Wang, S. Yang, and R. Huang, “The effect of solar cell shunt resistance change on the bus voltage ripple in spacecraft power system,” *Microelectronics Reliability,* vol. 88, pp. 1047-1050, 2018.
[165] V. d’Alessandro, P. Guerriero, S. Daliento, and M. Gargiulo, “A straightforward method to extract the shunt resistance of photovoltaic cells

from current–voltage characteristics of mounted arrays," *Solid-State Electronics,* vol. 63, no. 1, pp. 130-136, 2011.

[166] Y. S. Kim, S.-M. Kang, B. Johnston, and R. Winston, "A novel method to extract the series resistances of individual cells in a photovoltaic module," *Solar energy materials and solar cells,* vol. 115, pp. 21-28, 2013.

[167] Z. Lucheng, and S. Hui, "Novel approach for characterizing the specific shunt resistance caused by the penetration of the front contact through the p–n junction in solar cell," *Journal of Semiconductors,* vol. 30, no. 7, pp. 074007, 2009.

[168] A. Mohapatra, B. Nayak, and K. Mohanty, "Parameter Extraction of PV Module using NLS Algorithm with Experimental Validation," *International Journal of Electrical and Computer Engineering,* vol. 7, no. 5, pp. 2392, 2017.

[169] M. Elyaqouti, D. Saadaoui, S. Lidaighbi, J. Chaoufi, A. Ibrahim, R. Aqel, and S. Obukhov, "A novel hybrid numerical with analytical approach for parameter extraction of photovoltaic modules," *Energy Conversion and Management: X,* vol. 14, pp. 100219, 2022.

[170] K. Ramalingam, C. Indulkar, G. B. Gharehpetian, and S. M. Mousavi Agah, "Chapter 3 - Solar Energy and Photovoltaic Technology," *Distributed Generation Systems,* pp. 69-147: Butterworth-Heinemann, 2017.

[171] S. K. Vankadara, S. Chatterjee, and P. K. Balachandran, "An accurate analytical modeling of solar photovoltaic system considering Rs and Rsh under partial shaded condition," *International Journal of System Assurance Engineering and Management,* pp. 1-10, 2022.

[172] S. Roy, and R. Gupta, "Quantitative Estimation of Shunt Resistance in Crystalline Silicon Photovoltaic Modules by Electroluminescence Imaging," *IEEE Journal of Photovoltaics,* vol. 9, no. 6, pp. 1741-1747, 2019.

[173] S. Kaplanis, and E. Kaplani, "Energy performance and degradation over 20 years performance of BP c-Si PV modules," *Simulation Modelling Practice and Theory,* vol. 19, no. 4, pp. 1201-1211, 2011.

[174] A. D. Dhass, N. Beemkumar, S. Harikrishnan, and H. M. Ali, "A Review on Factors Influencing the Mismatch Losses in Solar Photovoltaic System," *International Journal of Photoenergy,* vol. 2022, 2022.

[175] A. Sinha, O. Sastry, and R. Gupta, "Nondestructive characterization of encapsulant discoloration effects in crystalline-silicon PV modules," *Solar Energy Materials and Solar Cells,* vol. 155, pp. 234-242, 2016.

[176] A. R. Gxasheka, E. E. Van Dyk, and E. L. Meyer, "Evaluation of performance parameters of PV modules deployed outdoors," *Renewable Energy,* vol. 30, no. 4, pp. 611-620, 2005.

[177] P. Rajput, M. Malvoni, N. M. Kumar, O. S. Sastry, and G. N. Tiwari, "Risk priority number for understanding the severity of photovoltaic failure modes and their impacts on performance degradation," *Case Studies in Thermal Engineering,* vol. 16, 2019.

[178] H. A. Al Mahdi, P. G. Leahy, and A. P. Morrison, "Predicting Early EVA Degradation in Photovoltaic Modules From Short Circuit Current Measurements," *IEEE Journal of Photovoltaics,* 2021.

[179] C. S. Ruschel, F. P. Gasparin, E. R. Costa, and A. Krenzinger, "Assessment of PV modules shunt resistance dependence on solar irradiance," *Solar Energy,* vol. 133, pp. 35-43, 2016.

[180] A. Sinha, O. S. Sastry, and R. Gupta, "Nondestructive characterization of encapsulant discoloration effects in crystalline-silicon PV modules," *Solar Energy Materials and Solar Cells,* vol. 155, pp. 234-242, 2016.

[181] J. Zhang, Y. Liu, K. Ding, L. Feng, F. U. Hamelmann, and X. Chen, "Model Parameter Analysis of Cracked Photovoltaic Module under Outdoor Conditions," *2020 47th IEEE Photovoltaic Specialists Conference (PVSC),* pp. 2509-2512, 2020.

[182] S. Gallardo-Saavedra, L. Hernández-Callejo, M. del Carmen Alonso-García, J. D. Santos, J. I. Morales-Aragonés, V. Alonso-Gómez, Á. Moretón-Fernández, M. Á. González-Rebollo, and O. Martínez-Sacristán, "Nondestructive characterization of solar PV cells defects by means of electroluminescence, infrared thermography, I–V curves and visual tests: Experimental study and comparison," *Energy,* vol. 205, pp. 117930, 2020.

[183] J. Oh, S. Bowden, and G. TamizhMani, "Potential-induced degradation (PID): Incomplete recovery of shunt resistance and quantum efficiency losses," *IEEE Journal of Photovoltaics,* vol. 5, no. 6, pp. 1540-1548, 2015.

[184] W. Luo, Y. S. Khoo, P. Hacke, V. Naumann, D. Lausch, S. P. Harvey, J. P. Singh, J. Chai, Y. Wang, and A. G. Aberle, "Potential-induced degradation in photovoltaic modules: a critical review," *Energy & environmental science,* vol. 10, no. 1, pp. 43-68, 2017.

[185] E. L. Meyer, and E. E. Van Dyk, "The effect of reduced shunt resistance and shading on photovoltaic module performance." in *Conference Record of the Thirty-first IEEE Photovoltaic Specialists Conference, 2005.,* 2005: IEEE, pp. 1331-1334.

[186] A. D. Dhass, E. Natarajan, and L. Ponnusamy, "Influence of shunt resistance on the performance of solar photovoltaic cell," *2012 International Conference on Emerging Trends in Electrical Engineering and Energy Management (ICETEEEM)*, pp. 382-386, 2012.

[187] E. E. van Dyk, and E. L. Meyer, "Analysis of the effect of parasitic resistances on the performance of photovoltaic modules," *Renewable Energy*, vol. 29, no. 3, pp. 333-344, 2004.

[188] K. L. Kennerud, "Analysis of performance degradation in CdS solar cells," *IEEE Transactions on aerospace and electronic systems*, no. 6, pp. 912-917, 1969.

[189] S. R. Rummel, and T. J. McMahon, "Effect of cell shunt resistance on PV module performance at reduced light levels," *AIP conference proceedings*, vol. 353, no. 1, pp. 581-586, 1996.

[190] S. Chattopadhyay, R. Dubey, V. Kuthanazhi, J. J. John, C. S. Solanki, A. Kottantharayil, B. M. Arora, K. Narasimhan, V. Kuber, and J. Vasi, "Visual degradation in field-aged crystalline silicon PV modules in India and correlation with electrical degradation," *IEEE Journal of photovoltaics*, vol. 4, no. 6, pp. 1470-1476, 2014.

[191] H. M. Walwil, A. Mukhaimer, F. Al-Sulaiman, and S. A. Said, "Comparative studies of encapsulation and glass surface modification impacts on PV performance in a desert climate," *Solar Energy*, vol. 142, pp. 288-298, 2017.

[192] M. Aghaei, A. Fairbrother, A. Gok, S. Ahmad, S. Kazim, K. Lobato, G. Oreski, A. Reinders, J. Schmitz, and M. Theelen, "Review of degradation and failure phenomena in photovoltaic modules," *Renewable and Sustainable Energy Reviews*, vol. 159, pp. 112160, 2022.

[193] L. W. Nagel, and D. O. Pederson, *SPICE (Simulation Program with Integrated Circuit Emphasis)*, EECS Department, University of California, Berkeley, 1973.

[194] R. Bhide, and S. R. Bhat, "Modular power conditioning unit for photovoltaic applications," *PESC'92 Record. 23rd Annual IEEE Power Electronics Specialists Conference*, pp. 708-713, 1992.

[195] L. Castañer, R. Aloy, and D. Carles, "Photovoltaic system simulation using a standard electronic circuit simulator," *Progress in Photovoltaics: Research and applications*, vol. 3, no. 4, pp. 239-252, 1995.

[196] A. D. Simmons, and D. G. Infield, "Current waveform quality from grid-connected photovoltaic inverters and its dependence on operating

conditions," *Progress in Photovoltaics: Research and Applications,* vol. 8, no. 4, pp. 411-420, 2000.

[197] A. Moreno, J. Julve, S. Silvestre, and L. Castañer, "SPICE macromodeling of photovoltaic systems," *Progress in Photovoltaics: Research and Applications,* vol. 8, no. 3, pp. 293-306, 2000.

[198] A. Standard, "E892," Terrestrial Solar Spectral Irradiance Tables at Air Mass 1.5 for a 37 deg," *Tilted Surface", American Society for Testing and Materials, Philadelphia, PA,* 1985.

[199] I. Standard, "60904-3, Measurement principles for terrestrial pv solar devices with reference spectral irradiance data," *International Electrotechnical Commission, Geneva, Switzerland,* 2008.

[200] M. Dhimish, A. Ahmad, and A. M. Tyrrell, "Inequalities in photovoltaics modules reliability: From packaging to PV installation site," *Renewable Energy,* 2022.

[201] C. Riordan, and R. Hulstron, "What is an air mass 1.5 spectrum?(Solar cell performance calculations)." in *IEEE Conference on Photovoltaic Specialists,* 1990: IEEE, pp. 1085-1088.

[202] R. Hulstrom, R. Bird, and C. Riordan, "Spectral solar irradiance data sets for selected terrestrial conditions," *solar cells,* vol. 15, no. 4, pp. 365-391, 1985.

[203] J. Cotter, J. Guo, P. Cousins, M. Abbott, F. Chen, and K. Fisher, "P-type versus n-type silicon wafers: prospects for high-efficiency commercial silicon solar cells," *IEEE Transactions on Electron Devices,* vol. 53, no. 8, pp. 1893-1901, 2006.

[204] H. Mølnås, B. Russ, S. L. Farrell, M. P. Gordon, J. J. Urban, and A. Sahu, "n-Type doping of a solution processed p-type semiconductor using isoelectronic surface dopants for homojunction fabrication," *Applied Surface Science,* vol. 590, pp. 153089, 2022.

[205] "PClD Photovoltaics Special Research Centre at the University of New South Wales, Sydney, Australia.."

[206] A. M. Krishna, K. P. Rao, M. B. Prakash, and N. Ramchander, "Data acquisition system for performance monitoring of solar photovoltaic (PV) power generation," *Int J Eng Res Tech,* vol. 1, no. 7, pp. 1-6, 2012.

[207] H. Rezk, I. Tyukhov, M. Al-Dhaifallah, and A. Tikhonov, "Performance of data acquisition system for monitoring PV system parameters," *Measurement,* vol. 104, pp. 204-211, 2017.

[208] N. S. Reddy, C. Gowthami, E. Mounika, S. Harshad, and R. V. P. Kumar, "Real-Time Data Acquisition to Excel and Monitoring Characteristics of

Solar Panel Using Arduino," *International Journal of Recent Advances in Multidisciplinary Topics,* vol. 3, no. 5, pp. 15-20, 2022.

[209] A. Khanna, T. Mueller, R. A. Stangl, B. Hoex, P. K. Basu, and A. G. Aberle, "A fill factor loss analysis method for silicon wafer solar cells," *IEEE Journal of Photovoltaics,* vol. 3, no. 4, pp. 1170-1177, 2013.

[210] F. J. Pern, "Ethylene-vinyl acetate (EVA) encapsulants for photovoltaic modules: Degradation and discoloration mechanisms and formulation modifications for improved photostability," *Die Angewandte Makromolekulare Chemie: Applied Macromolecular Chemistry and Physics,* vol. 252, no. 1, pp. 195-216, 1997.

[211] F. J. Pern, "Factors that affect the EVA encapsulant discoloration rate upon accelerated exposure," *Solar energy materials and solar cells,* vol. 41, pp. 587-615, 1996.

[212] G. Verma, *Autodesk fusion 360 black book*: BPB Publications, 2018.

[213] D. Chan, J. Phillips, and J. Phang, "A comparative study of extraction methods for solar cell model parameters," *Solid-State Electronics,* vol. 29, no. 3, pp. 329-337, 1986.

[214] J. Janesch, "Two-wire vs. four-wire resistance measurements: Which configuration makes sense for your application," *no. May,* pp. 2-4, 2013.

[215] H. Abdelhamid, A. Edris, A. Helmy, and Y. Ismail, "Fast and accurate PV model for SPICE simulation," *Journal of Computational Electronics,* vol. 18, no. 1, pp. 260-270, 2019.

[216] M. De Blas, J. Torres, E. Prieto, and A. Garcıa, "Selecting a suitable model for characterizing photovoltaic devices," *Renewable energy,* vol. 25, no. 3, pp. 371-380, 2002.

[217] R. Asadpour, X. Sun, and M. A. Alam, "Electrical signatures of corrosion and solder bond failure in c-Si solar cells and modules," *IEEE Journal of Photovoltaics,* vol. 9, no. 3, pp. 759-767, 2019.

[218] P. Dash, and N. Gupta, "Effect of temperature on power output from different commercially available photovoltaic modules," *International Journal of Engineering Research and Applications,* vol. 5, no. 1, pp. 148-151, 2015.

[219] C. F. Abe, J. B. Dias, G. Notton, and P. Poggi, "Computing solar irradiance and average temperature of photovoltaic modules from the maximum power point coordinates," *IEEE Journal of Photovoltaics,* vol. 10, no. 2, pp. 655-663, 2020.

[220] T. J. McMahon, T. S. Basso, and S. R. Rummel, "Cell shunt resistance and photovoltaic module performance," *Conference Record of the Twenty Fifth IEEE Photovoltaic Specialists Conference-1996*, pp. 1291-1294, 1996.
[221] H. Yan, Z. Zhou, and H. Lu, "Photovoltaic industry and market investigation," *2009 International Conference on Sustainable Power Generation and Supply*, pp. 1-4, 2009.
[222] P. J. Verlinden, "Future challenges for photovoltaic manufacturing at the terawatt level," *Journal of Renewable and Sustainable Energy,* vol. 12, no. 5, pp. 053505, 2020.
[223] A. Chouder, S. Silvestre, B. Taghezouit, and E. Karatepe, "Monitoring, modelling and simulation of PV systems using LabVIEW," *Solar Energy,* vol. 91, pp. 337-349, 2013.
[224] A. Chouder, S. Silvestre, N. Sadaoui, and L. Rahmani, "Modeling and simulation of a grid connected PV system based on the evaluation of main PV module parameters," *Simulation Modelling Practice and Theory,* vol. 20, no. 1, pp. 46-58, 2012.
[225] Y. Jiang, J. A. A. Qahouq, and I. Batarseh, "Improved solar PV cell Matlab simulation model and comparison," *2010 IEEE International Symposium on Circuits and Systems (ISCAS)*, pp. 2770-2773, 2010.
[226] K. Ishaque, Z. Salam, and H. Taheri, "Modeling and simulation of photovoltaic (PV) system during partial shading based on a two-diode model," *Simulation Modelling Practice and Theory,* vol. 19, no. 7, pp. 1613-1626, 2011.
[227] V. Khanna, B. K. Das, and D. Bisht, "Matlab/simelectronics models based study of solar cells," *International Journal of Renewable Energy Research (IJRER),* vol. 3, no. 1, pp. 30-34, 2013.
[228] M. A. Munoz, M. C. Alonso-García, N. Vela, and F. Chenlo, "Early degradation of silicon PV modules and guaranty conditions," *Solar Energy,* vol. 85, no. 9, pp. 2264-2274, 2011.
[229] M. Fuentes, M. Vivar, H. Hosein, J. Aguilera, and E. Muñoz-Cerón, "Lessons learned from the field analysis of PV installations in the Saharawi refugee camps after 10 years of operation," *Renewable and Sustainable Energy Reviews,* vol. 93, pp. 100-109, 2018.
[230] V. Sharma, and S. S. Chandel, "Performance and degradation analysis for long term reliability of solar photovoltaic systems: A review," *Renewable and Sustainable Energy Reviews,* vol. 27, pp. 753-767, 2013.
[231] A. Luque, and S. Hegedus, *Handbook of photovoltaic science and engineering*: John Wiley & Sons, 2011.

[232] C.-T. Sah, R. N. Noyce, and W. Shockley, "Carrier generation and recombination in pn junctions and pn junction characteristics," *Proceedings of the IRE,* vol. 45, no. 9, pp. 1228-1243, 1957.

[233] K. Nishioka, N. Sakitani, Y. Uraoka, and T. Fuyuki, "Analysis of multicrystalline silicon solar cells by modified 3-diode equivalent circuit model taking leakage current through periphery into consideration," *Solar energy materials and solar cells,* vol. 91, no. 13, pp. 1222-1227, 2007.

[234] M. K. Singla, and P. Nijhawan, "Triple diode parameter estimation of solar PV cell using hybrid algorithm," *International Journal of Environmental Science and Technology,* vol. 19, no. 5, pp. 4265-4288, 2022.

[235] D. S. H. Chan, and J. C. H. Phang, "Analytical methods for the extraction of solar-cell single-and double-diode model parameters from IV characteristics," *IEEE Transactions on Electron devices,* vol. 34, no. 2, pp. 286-293, 1987.

[236] C. J. Willmott, K. Matsuura, and S. M. Robeson, "Ambiguities inherent in sums-of-squares-based error statistics," *Atmospheric Environment,* vol. 43, no. 3, pp. 749-752, 2009.

[237] T. Chai, and R. R. Draxler, "Root mean square error (RMSE) or mean absolute error (MAE)?–Arguments against avoiding RMSE in the literature," *Geoscientific model development,* vol. 7, no. 3, pp. 1247-1250, 2014.

[238] K. Loague, and R. E. Green, "Statistical and graphical methods for evaluating solute transport models: overview and application," *Journal of contaminant hydrology,* vol. 7, no. 1-2, pp. 51-73, 1991.

[239] R. N. Lee, "Two-dimensional critical point configuration graphs," *IEEE Transactions on Pattern Analysis and Machine Intelligence,* no. 4, pp. 442-450, 1984.

[240] A. H. Almasoud, and H. M. Gandayh, "Future of solar energy in Saudi Arabia," *Journal of King Saud University-Engineering Sciences,* vol. 27, no. 2, pp. 153-157, 2015.

[241] "Electromechanical Devices , Laboratory Manual ", Electrical Engineering Department, King Fahd University of Petroleum & Minerals, N.D.

[242] T. Berghout, M. Benbouzid, T. Bentrcia, X. Ma, S. Djurović, and L.-H. Mouss, "Machine Learning-Based Condition Monitoring for PV Systems: State of the Art and Future Prospects," *Energies,* vol. 14, no. 19, pp. 6316, 2021.

[243] Y. Zhao, L. Yang, B. Lehman, J.-F. de Palma, J. Mosesian, and R. Lyons, "Decision tree-based fault detection and classification in solar photovoltaic arrays," *2012 Twenty-Seventh Annual IEEE Applied Power Electronics Conference and Exposition (APEC)*, pp. 93-99, 2012.

[244] V. Quaschning, *Understanding renewable energy systems*: Routledge, 2016.

[245] I. A. Board, "Joule Pulsa Solar PV Systems."

[246] S. K. Sahoo, M. Shah, N. A. Dawlatzai, and R. A. J. Amalorpavaraj, "Assessment of mismatching in series and parallel connection of the PV modules of different technologies and electrical parameters," *2020 International Conference on Computer Communication and Informatics (ICCCI)*, pp. 1-5, 2020.

[247] Sustainable Energy Authority of Ireland, "Frequently Asked Questions on Solar Photovoltaics," SEAI, Ireland, N.D.

[248] S. La Monaca, and L. Ryan, "Solar PV where the sun doesn't shine: Estimating the economic impacts of support schemes for residential PV with detailed net demand profiling," *Energy Policy*, vol. 108, pp. 731-741, 2017.

[249] L. M. Ayompe, A. Duffy, S. J. McCormack, and M. Conlon, "Projected costs of a grid-connected domestic PV system under different scenarios in Ireland, using measured data from a trial installation," *Energy Policy*, vol. 38, no. 7, pp. 3731-3743, 2010.

[250] "How Much Does It Cost To Repair Or Remove Solar Panels?," 02-12 - 2021, 2021, [Online] ; https://www.homeadvisor.com/cost/heating-and-cooling/repair-solar-panels/.

[251] M. Orkisz, "Estimating effects of individual PV panel failures on PV array output," *IEEE Transactions on Industry Applications*, vol. 54, no. 5, pp. 4825-4832, 2018.